Measuring the Higgs self-coupling at an electron-positron collider

Michele Faucci Giannelli

Physics Department
Royal Holloway University of London

A thesis submitted to the University of London

for the degree of Doctor of Philosophy

November 2008

this page must be removed

Declaration

I declare that the work presented in this thesis is my own.

Michele Faucci Giannelli

Abstract

The Standard Model of particle physics predicts the value of the self-coupling of the Higgs boson but it cannot be measured at the Large Hadron Collider even if the boson is discovered there. This measurement requires a machine such as the proposed International Linear Collider (ILC) with a centre of mass energy of 500 GeV or more. In this thesis, the sensitivity to the Higgs self-coupling is evaluated using the ZHH to six jets channel for a Higgs mass of $120\,\mathrm{GeV/c^2}$. Full simulation has been carried out for $500\,\mathrm{fb^{-1}}$ of both signal events and the most significant backgrounds in a possible ILC detector known as the Large Detector Concept at a centre of mass energy of 500 GeV. Realistic algorithms have been used for tracking, clustering and vertex reconstruction of these events. A cut based analysis, a kinematic fit analysis and a neural network analysis are presented; the resolution evaluated with these analyses is 180%. A critical comparison with two previous analysis is presented.

The particle flow concept, which is the idea driving the detector design, is described as a possible solution for achieving high jet energy resolution. The motivation for the central role of calorimetry is discussed in the context of the composition of jets. Providing the required calorimeters is the goal of the CALICE R&D project. The CALICE collaboration has performed several beam tests with prototype calorimeters at DESY, CERN and FNAL. Some studies of the tracking systems used in the beam lines are presented together with an analysis of the position and angular resolution of the electromagnetic calorimeter prototype. The result from this analysis indicates that the calorimeter has a position resolution of about 1 mm and an angular resolution better than 30 mrad for electron energies above 20 GeV.

To Giovanna,

my love who endured and helped me while writing this thesis.

Thank you.

Acknowledgement

First of all I would like to thank my supervisor Prof. Mike Green. Thank you for providing me with a Thomas Holloway studentship that made this PhD possible. Thank also for the constant supervision that allowed me to focus on my work and to finish in only three years. Most important of all, thanks for all discussions during the last three years; they have been fundamental for my academic growth.

I would like to express my gratitude to Dr Fabrizio Salvatore for his constant support and the enlightening discussions which were essential for my work. I would like to thank him also for introducing me to research in particle physics during my summer studentship at Royal Holloway in 2003. A special thanks to both Fabrizio and his wife Dr Antonella De Santo for their guidance but most of all for the really good time spent together.

I could not have completed my work without the support of all the staff of the Royal Holloway Particle Physics Group; in particular I would like to thank Dr Glen Cowan for his help with statistics and Dr Veronique Boisvert for her help with the kinematic fit procedure. I would also like to thank Tina, Sudan, Lawrence and all the other new and old PhD students for their help and useful discussions.

During the last three years many more people have contributed to this work with ideas, suggestions and direct help. In particular I would like to thank Dr Erika Garutti for her help during the commissioning of the tracking systems and Prof. Paul Dauncey for the useful discussion during the analysis of the tracking system and the track reconstruction. I would also thank the UK CALICE and LDC communities for the support during the last three years. A special thanks to Prof. Francois Richard

who appointed me co-convener for the Higgs session at the EGFA meeting and offered me a post-doc at LAL.

Per ultimi, ma non meno importanti, voglio ringraziare la mia famiglia e in particolare i miei genitori per la loro fiducia nei miei confronti e per il loro continuo sostegno.

Contents

List of Figures

List of Tables

Chapter 1

Introduction

Particle physics is entering a period of likely discoveries with the start of the Large Hadron Collider. This machine and its detectors will study particle interactions at the Terascale, aiming to answer many open questions such as: does the Higgs boson exist, is Super Symmetry (SUSY) the correct extension to the Standard Model or does the Universe have extra dimensions? Many theories are likely to be discarded but LHC cannot give a definitive answer to many questions since the hadronic collider lacks the precision a lepton machine can achieve.

For this reason the international particle physics community is already working on the next generation electron-positron collider. In order to reach a centre of mass energy up to 1 TeV this machine must be a linear machine. In fact the maximum energy in a circular machine is limited by the energy lost by synchrotron radiation and LEP reached the region of the maximum with collisions up to 209 GeV. The International Linear Collider (ILC) is the global effort to develop the technology and study the performance required by the accelerator and the detectors in order to achieve several physics goals.

Besides the obvious centre of mass energy and luminosity requirements, the accelerator has other technical requirements such as a small number of pairs produced by the beam-beam interactions which could blind the vertex detector. The technology for the accelerator has been decided [1], superconducting cavities, but there is still a

lot of work to do in order to reach the gradient required by the ILC. For this reason there is a R&D programme to further develop the technology. Several other beam systems, such as the delivery and the polarisation systems, are in an advanced phase of development and the UK is leading the research in many of these areas.

The detector requirements [2] cover all sub-detectors, from vertex detector that should be able to reconstruct c-jets to the calorimeters that must provide a jet energy resolution of about $30\%/\sqrt{E}$; these requirements will be discussed in Chapter 3. In addition to these sub-detector based requirements, a list of benchmark physics channels has been proposed to assess the full detector performance [3]. The latest concept for the interaction region reduced the interaction points from two to one. Nevertheless the ILC community is planning to have two detectors to be alternated on the beam line using a push-pull system. At the time this work began there were four concepts (so called SiD, LDC, GLD and 4th concept). In the last year, the European (LDC) and the Japanese (GLD) concepts decided to join to form the International Large Detector (ILD) collaboration. This thesis is based on the LDC concept since the ILD detector baseline was decided only in September 2008. In addition to the three concepts that are studying the general properties of the detector, such as the magnetic field and the radius, there are several collaborations that are developing prototypes for the sub-detectors. One of these collaborations is the CAlorimetry for a LInear Collider Experiment (CALICE) collaboration which has built and tested several calorimeters prototypes on beam lines at DESY, CERN and FNAL.

I have been involved in both detector activities, the prototype R&D and the detector study, having worked within the CALICE collaboration and in the Large Detector Concept (LDC) detector optimisation group. My contribution to the CALICE experiment is described in Chapter 2 of this thesis: I was responsible for the commissioning of the tracking system of the test beam performed at DESY and at CERN and then I used the reconstructed tracks to evaluate the position and angular resolution of the electromagnetic calorimeter. The analysis on the sensitivity to the Higgs self-coupling is my main contribution to the LDC detector optimisation. This analysis requires high

performances from all sub-detectors, hence it is an excellent channel to benchmark the performance requirements of a detector. The theoretical framework that describes the Higgs sector of the Standard Model and in particular the Higgs self-coupling is summarised in Chapter 3 together with an overview of previous analyses performed using fast simulation. The particle flow concept was used to improve the reconstruction; this concept and the comparison of three currently available algorithms that implement it are described in Chapter 4. The analysis of the Higgs self-coupling sensitivity, performed using the best available particle flow algorithm, is presented in Chapter 5.

Chapter 2

The CALICE calorimeter prototype

2.1 Introduction

The CALICE collaboration [4] is developing and comparing several designs for the calorimetry system of a Linear Collider detector. The goal of the collaboration is to prove the technology and assess the performance of the proposed designs in time for the Engineering Design Report due in 2010. Several prototypes, for both electromagnetic and hadronic calorimeters, have been built and tested on beam lines. Such tests have taken place at DESY during May 2006 with a low energy electron beam and at CERN in the summer of 2006 and 2007 with high energy electron and hadronic beams. They are continuing in 2008 at FNAL with high and low energy beams of all types. The test beam runs will continue during the next years for old and new prototypes.

The UK groups have been involved in several tasks including the development of the data acquisition (DAQ) and of the Monte Carlo simulation, a major contribution in running the test beam and the analysis of the electromagnetic calorimeter (ECAL) data. My responsibility in the test beams was mainly the commissioning of the tracking system for the beams at DESY and CERN. To fulfil this task I performed several studies on the tracking system. I also developed a track reconstruction procedure and participated in the development of the official tracking package. The

reconstructed tracks were used to determine the position and angular resolution of the electromagnetic calorimeter.

The chapter is structured as follows: in Section 2.2 the electromagnetic calorimeter and electromagnetic showers are described. This is followed by the description of the test beams and the simulation in Section 2.3. Then in Sections 2.4 and 2.5 the studies on the tracking system at DESY and CERN respectively are presented. The analysis on the position and angular resolution is presented in Section 2.6.4.

2.2 The electromagnetic calorimeter prototype

2.2.1 Description

The design of the electromagnetic calorimeter is driven by two requirements: compactness, in order to reduce the radius of the coil, and high segmentation, to allow particle flow reconstruction. Therefore the calorimeter must have a small Molière radius (a measure of the lateral spread of an electromagnetic shower) and small radiation length (X_0, the distance for which an electron travelling in the material reduces its energy by a factor e); the first requirement allows better separation between showers from different particles, while the second makes the calorimeter more compact. These two requirements are further discussed in Section 3.2 and Chapter 4. Tungsten was chosen, having a Molière radius of 9 mm and a X_0 of 3.5 mm; tungsten is also mechanically strong hence it does not require additional material for support. The sensitive material is in the form of silicon 1×1 cm^2 pixels built in wafers of 6×6 pixels with nine wafers (3×3) forming a layer.

The prototype calorimeter [5], as shown in Figure 2.1(a), was divided into three sections (green, blue and yellow in the figure), 10 layers per section, with an increasing thickness of tungsten; in the first section the thickness was 1.4 mm, in the second it was 2.8 mm and in the last it was 4.2 mm. Therefore the electromagnetic calorimeter was made of 30 layers for a total of $24\,X_0$ and 9720 channels. The separation of the three sections also allowed the rotation of the calorimeter to study the effect of

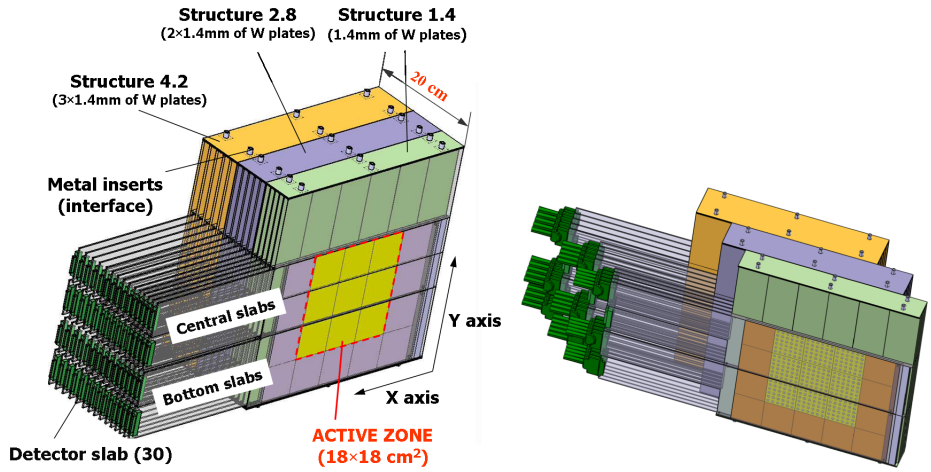

(a) (b)

Figure 2.1: Schematics of the electromagnetic calorimeter: (a) normal configuration and (b) rotated configuration (from [5]).

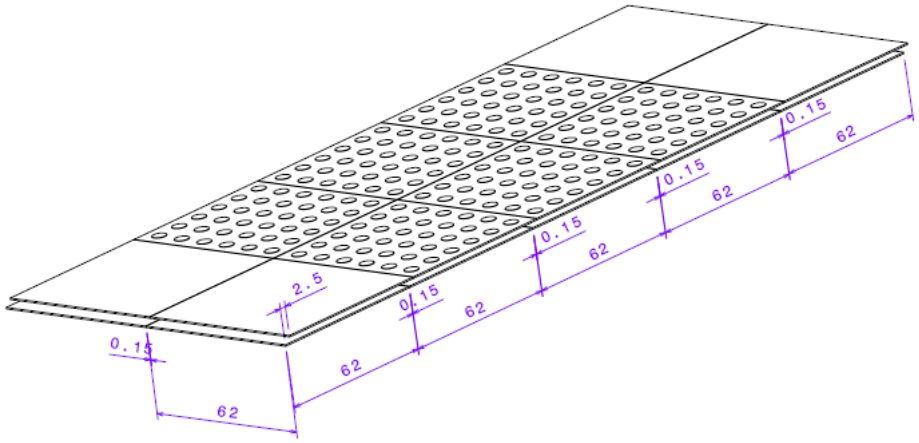

Figure 2.2: Schematics of a slab of the electromagnetic calorimeter; all distances are in mm (CALICE collaboration).

different impact angles as shown in Figure 2.1(b).

To increase the compactness of the calorimeter, each pair of layers was combined in a "slab"; one of the two tungsten layers was part of the calorimeter structure and the two sensitive layers were fixed to the second passive layer to form the movable part of the prototype. A schematic of the structure of a slab is shown in Figure 2.2 while the zoom of the border region between two wafers is shown in Figure 2.3. It is possible to see that the total gap between the active elements was about 2.6 mm. In order to cover these dead areas, the two sensitive planes in a slab were offset by 2.5 mm in the x direction. Furthermore the slabs were offset by 1.3 mm in the x direction (Figure

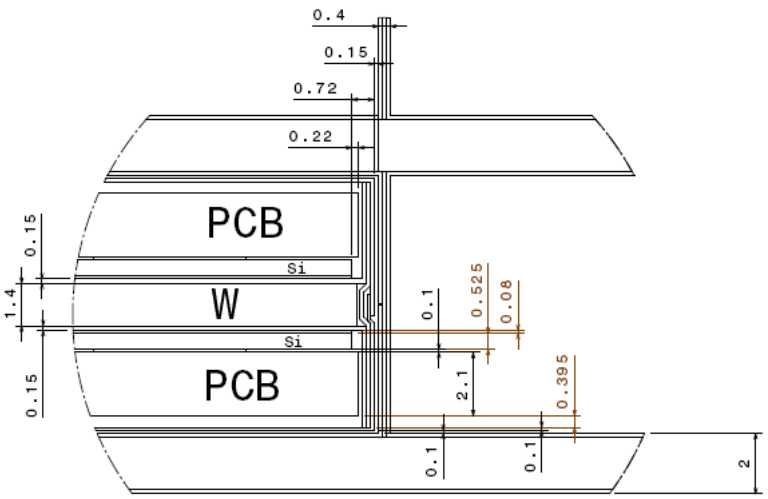

Figure 2.3: Schematics of the region between two wafers; all distances are in mm (CALICE collaboration).

2.4). The prototype was divided into two parts along the y direction for mechanical reasons; the upper part contained a 2×3 matrix of silicon wafers (central slab in Figure 2.1) while the bottom part had only one line of three silicon wafers (bottom slab in Figure 2.1); this separation caused a further gap of 1.8 mm between the wafers.

The signal in the silicon was read out by a multi-layer printed circuit board (PCB) which carried the signal to the very front end electronics. This was located outside the detector to reduce dead areas and simplify thermal dissipation. Each wafer was read out by two Application Specific Integrated Circuits (ASICs) that were used to shape the signal. The ASICs were read out by the DAQ which was based on customised VME cards, each hosting an FPGA and several ADCs. The TDC board used for the tracking system was integrated in the DAQ system.

2.2.2 Electromagnetic shower in the detector

The physics related to electron interactions in matter is well known: they lose energy interacting by ionisation or by emitting a bremsstrahlung photon. The energy at which the two energy losses are equal is called the *critical energy*. Figure 2.5 shows the energy loss of electrons in matter as function of the electron energy. For every radiation length, the energy of an electron is reduced by a factor e. A beam electron

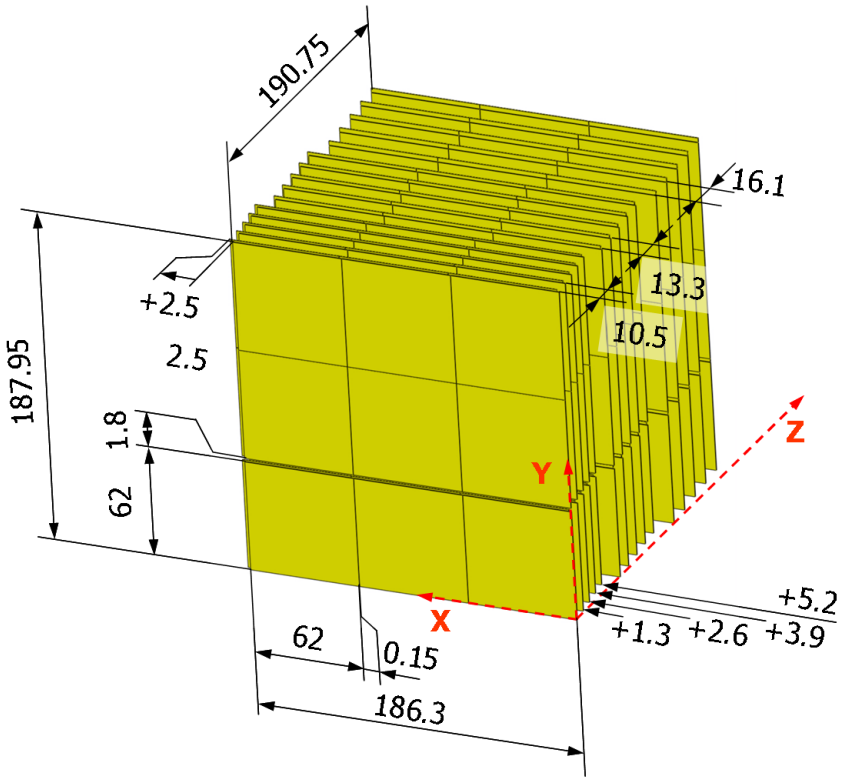

Figure 2.4: Schematics of the electromagnetic calorimeter (from [5]).

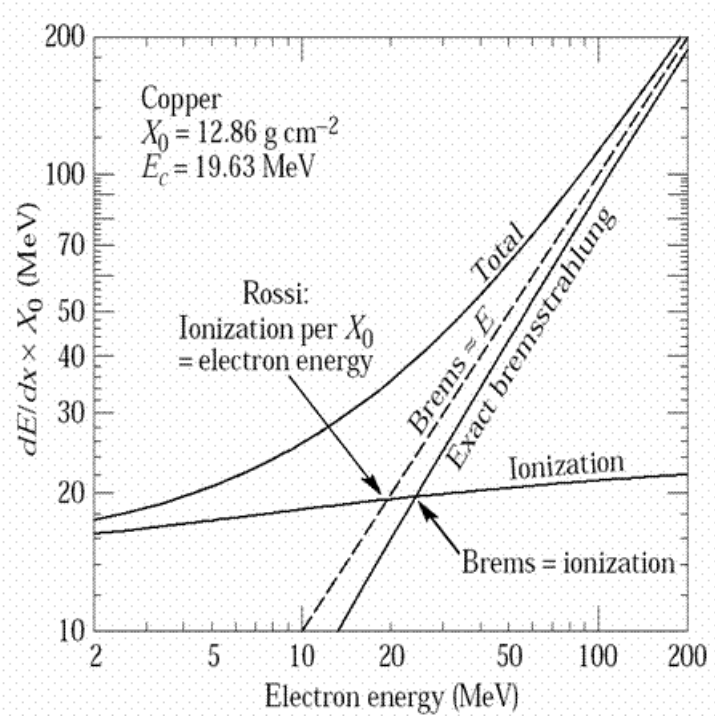

Figure 2.5: Energy loss of electron in copper (from [6]).

loses essentially all of its energy by emission of bremsstrahlung photons, which then convert to electron-positron pairs. The number of emitted photons is proportional to the energy of the emitting electron. The multiplication continues with electrons emitting more photons and photons converting into pairs until the energy of the electrons is below the critical energy and the energy of the photons is below threshold for pair production. This chain of reactions is called an electromagnetic shower. The typical shower of a 10 GeV electron is contained in about 20 X_0. The electromagnetic calorimeter had a total depth of 24 X_0, enough to contain most of the showers.

In the calorimeter the shower develops mainly in the tungsten, the passive material. When the shower reaches the end of a tungsten layer, the particles travel through the silicon and the support material. This less dense material causes an increase of the effective Molière radius and X_0; i.e. preliminary studies have shown that the effective Molière radius increases from 9 mm to 20 mm [7]. The electrons and positrons that pass through the silicon release 2 MeV/cm; this is the energy released by a particle at the minimum ionisation point (MIP). This energy, collected as charge, is what the calorimeter detects of the electromagnetic shower and it is the reason why the energy can be expressed in MIPs. The number of particles produced in a shower is proportional to the number of emitted photons which is, as already mentioned, proportional to the energy of the primary particle, hence counting the electrons and the positrons in the shower measures the energy. Since only a fraction of the total energy is measured, this type of calorimeter is called a sampling calorimeter.

2.3 Beam lines description

Beam tests were performed at DESY in May 2006 and at CERN during 2006 and 2007. At the DESY test beam only the electromagnetic calorimeter (ECAL) was tested. At CERN all CALICE calorimeters were tested: the ECAL, the hadronic calorimeter (HCAL [8]) and a third calorimeter used as a tail catcher and muon tracker (TCMT [9]). Each test beam had a different configuration depending on the goal of the data

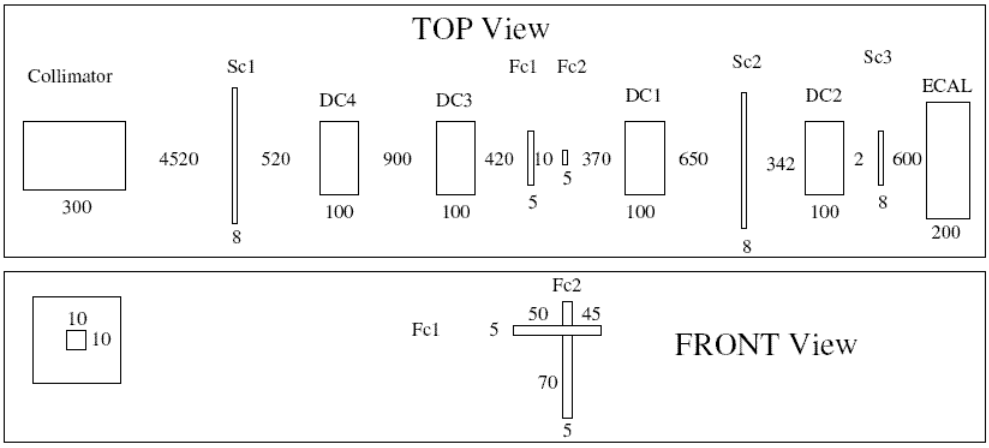

Figure 2.6: DESY test beam schematic.

taking. The ECAL dedicated runs in 2006 at CERN had the calorimeters separated because the ECAL needed to be rotated. In 2007 the two calorimeters were as close as possible to perform particle flow studies on the whole system.

2.3.1 The DESY test beam

The DESY beam line setup is shown in Figure 2.6. Four drift chambers (DC 1 to 4) were placed in front of the ECAL together with the triggering system formed by three scintillators planes and two crossed finger scintillators. A collimator was placed at the end of the vacuum tube, 5 m in front of the first drift chamber (DC4). The trigger was defined by the coincidence of the three scintillators (Sc1, Sc2 and Sc3). The beam was tunable in the energy range 1 to 6 GeV and either electrons or positrons could be selected.

2.3.2 The 2006 CERN test beam

The test beam at CERN took place in August and October at the H6 beam area of the SPS [10]. The H6 beam could be tuned to be composed mainly of negative pions, protons and positive pions, positrons or electrons with energy from 6 GeV up to 180 GeV for pions or 90 GeV for electrons. Muons were produced by closing the beam dumps at the beginning of the beam area. The configuration of the beam line is shown in Figure 2.7. The first element was a Ĉerenkov detector used to separate

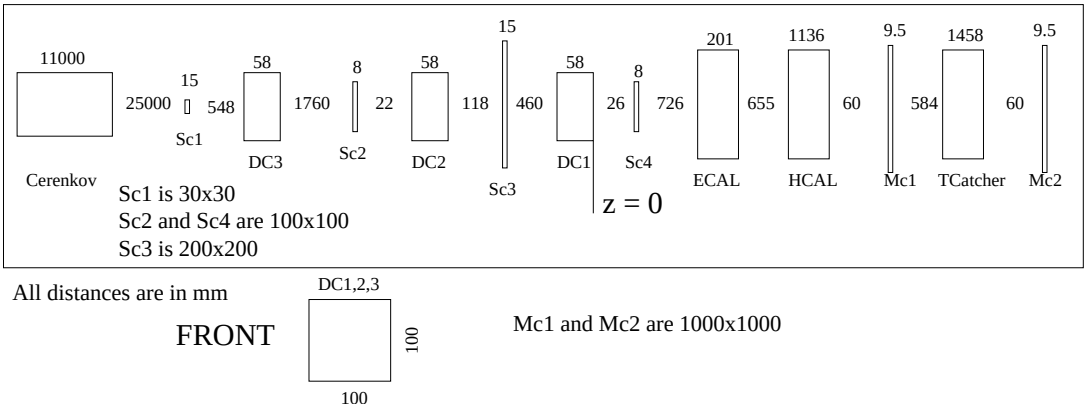

Figure 2.7: Configuration of the CERN test beam in summer 2006.

electrons and pions or pions and protons. The tracking system was composed of three multi wire proportional chambers (MWPC, labelled also DC) while the trigger was defined as the coincidence of three scintillators (Sc1, Sc2 and Sc4). Sc3 had a hole in the centre and was used to veto the beam halo. The ECAL was placed on a movable and turning stage. The HCAL prototype was installed 655 mm behind of the ECAL in order to allow the rotation of the latter. The TCMT prototype was installed on the back of the HCAL prototype. Two $1\,\mathrm{m}^2$ scintillators (Mc1 and Mc2) were installed between the TCMT layers and were used as a muon trigger.

The configuration of the October run was similar. The main difference was the relocation of the ECAL 57 mm in front of the HCAL.

2.3.3 The 2007 CERN test beam

The 2007 beam line is shown in Figure 2.8. The test beam took place in the same H6 area at CERN, hence the tracking system was the same as 2006. The only difference was the relocation of the Mc2 scintillator from the back of the TCMT to the front of the beam line. This $1\,\mathrm{m}^2$ scintillator was used only to trigger muons together with the last scintillator (Mc1) in muon runs. Three other scintillators (Sc1, Sc2, Sc3) were used for the trigger in all other runs. The ECAL and the HCAL were placed on a common movable stage that allowed x and y scans of the detectors; the platform could also rotate up to 30° in order to study the angle effect on linearity and resolution for both calorimeters. The TCMT was placed in a fixed position behind the HCAL.

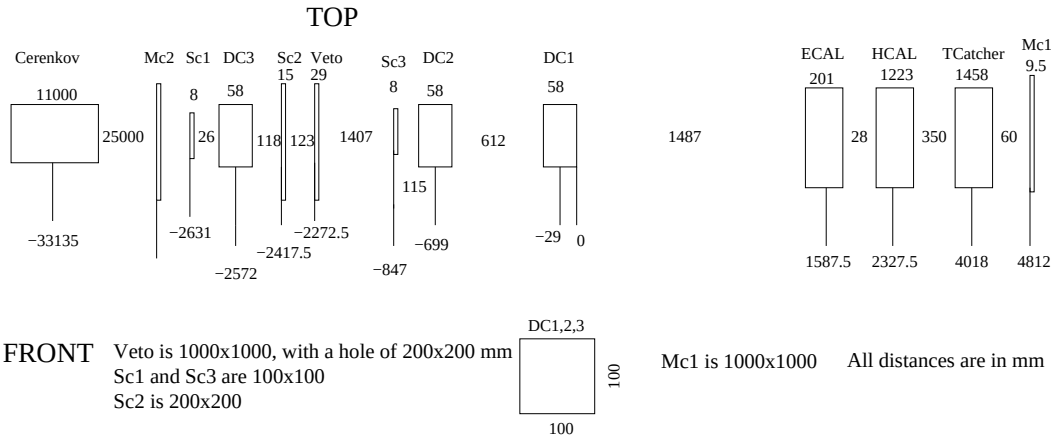

Figure 2.8: Configuration of the CERN test beam in summer 2007.

2.3.4 Monte Carlo simulation of the test beam

The various configurations described in Section 2.3 have been simulated in MOKKA [11], a Geant4 based application. The tracking chambers have been simulated as a single volume of gas. The average of the position of the hits produced in a chamber was digitised using Gaussian smearing. For the calorimeter a simple digitisation was applied. In order to study the tracking performance, the position and the momentum of the simulated particles at the front face of the calorimeter were recorded. All elements on the beam line have been simulated in order to include the correct amount of material in front of the calorimeter. The areas beyond the test beam area were not accessible, hence not all the material before the collimator at DESY or the Ĉerenkov detector at CERN has been simulated. For this reason the amount of multiple Coulomb scattering may be slightly underestimated in the simulation. In order to avoid this problem, only high energy runs in which the scattering is very low were used for the position resolution study of Section 2.6.4.

2.4 The DESY tracking system

A study of the position and angular resolution of the calorimeter requires the reconstruction of the beam particle in each event, and hence a prior requirement is an understanding of the performance of the beam chambers. In this Section the evalua-

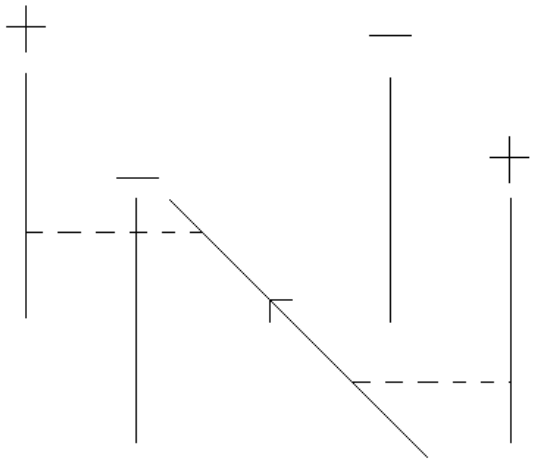

Figure 2.9: Schematics for the DESY tracking chambers. The continuous inclined line is the electron trajectory. The dotted lines are the distances measured by the chambers. Two consecutive chambers had the opposite electric field.

tion of the efficiency, the drift velocity in the gas and the intrinsic resolution of the DESY tracking chambers are described.

2.4.1 The DESY drift chambers

Four identical chambers were used during the DESY test beam. Each chamber was separated in two parts; one had a vertical electric field, the second had a horizontal electric field. This configuration allowed the measurement of the beam particle's position in both x and y directions. Each chamber was supplied with a positive and a negative voltage used for each direction. The values for the negative voltages were the nominal ones (-2500 V); those for the positive high voltage were chosen to maximise the chamber efficiency as described is Section 2.4.2. The uniform electric field was generated by a series of wires placed at the opposite sides of the chamber. Two consecutive chambers had the anode and the cathode switched, resulting in an opposite drift direction. It was possible to evaluate the impact point from the drift velocity of the electrons in the gas and the time required by the electrons to drift to the wire. The schematics of the chambers are shown in Figure 2.9.

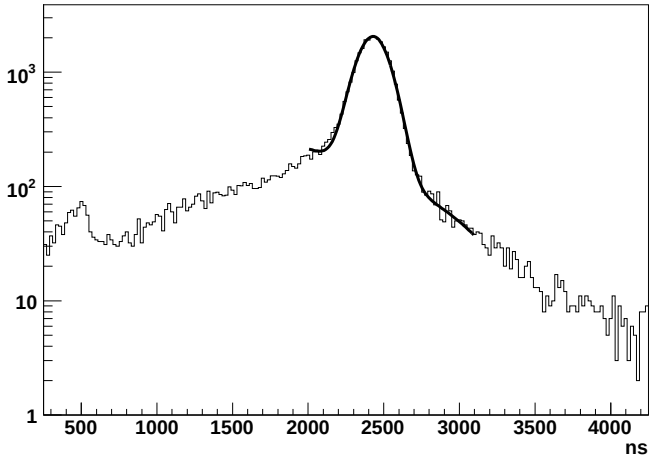

Figure 2.10: Typical distribution of the sum of times for two consecutive chambers, the drift velocity is the calculated as the dimension of the chamber (72 mm) divided by the mean of the distribution. In this fit a parabolic background is included.

2.4.2 Efficiency

A high efficiency was required for each chamber in order to have a large number of events with a well reconstructed track. In March 2006 the gas mixture was changed (for safety reasons) from 50:50 argon-ethane to 95:5. The efficiency of the new gas mixture was tested before the start of the test beam to validate the change. Two different methods were used to investigate the chamber efficiencies using a 3 GeV electron beam.

- In the first method the product of the efficiencies of two consecutive parallel wires is determined. The sum of the time of two consecutive parallel wires should be a constant in the hypothesis of identical drift velocity in the chambers and orthogonal tracks. Since the deviation from these assumptions was small, the beam had an angle of 10 mrad with respect to the chambers, this is a valid method for efficiency measurement. Figure 2.10 shows the distribution of the sum. The fit, performed between 2000 and 3200 ns, is a Gaussian distribution plus a parabolic function for the background. The area under the Gaussian distribution divided by all triggered events (the total number of entries in the plot) gives the product of the efficiency of the two wires. For example, DC12x

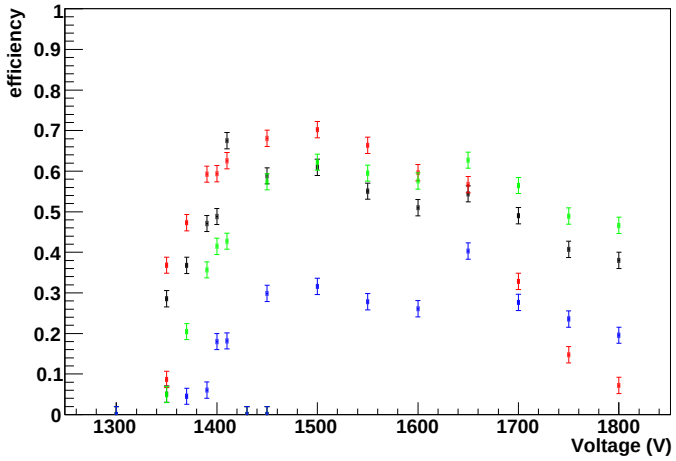

Figure 2.11: Efficiency as a function of the high voltage for several combinations of wires. Black is DC12 x, red is DC12 y, green is DC34 x and blue is DC34 y.

indicates the product of the efficiencies for the x wires in DC1 and DC2. The positive high voltage was changed to maximise the efficiency of all chambers. The result of the analysis is presented in Figure 2.11. The distribution has a discontinuity between 1600 and 1650 V. This effect is not understood other than that several hours had passed between the two sets of measurements. The result is not affected by this since the distribution clearly peaks at 1500 V. The same analysis performed on the chamber with the original gas mixture (50:50) gives an efficiency of 85%.

- In the second method the chamber efficiency is estimated using the product of x and y efficiencies. This method has the advantage of having to optimise only one high voltage at a time, since the x and y wires had the same power supply. The chamber measured the time distance between the point hit by the electron and the wire plane, as shown in Figure 2.12. If the electron was not detected, a spark or a second electron might be measured instead. The profile plot in Figure 2.13 shows the distribution of reconstructed events in a chamber. From the plot it is possible to distinguish several zones. The dark area in the bottom left corner is the contribution of the events correctly reconstructed by both wires. The points outside this region correspond to badly reconstructed events; in those parallel

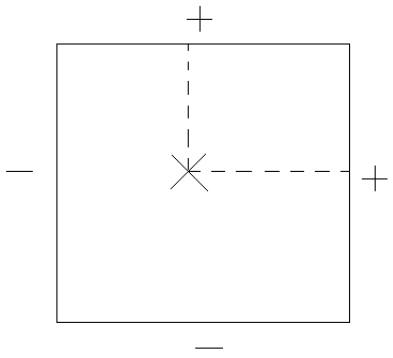

Figure 2.12: Single chamber schematics. The X is the impact position of the beam particle while the dotted lines are the distances measured by the two wire planes.

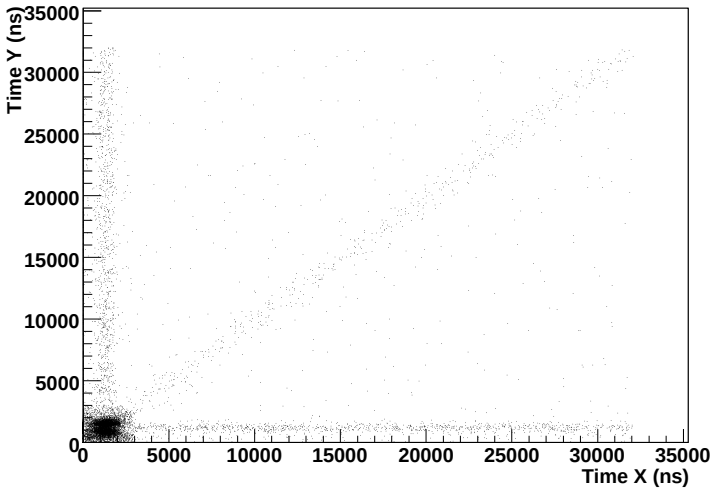

Figure 2.13: Profile plot of the hits in a chamber, the chamber itself is the dark area in the bottom left corner.

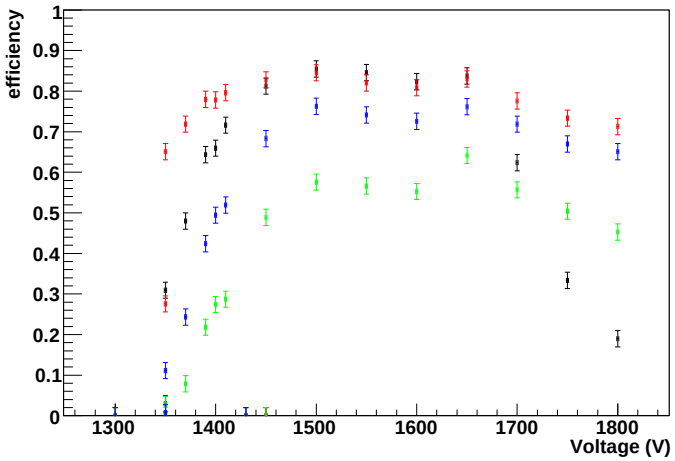

Figure 2.14: Efficiency as a function of the positive high voltage for all four chambers. Red is DC1, black is DC2, green is DC3 and blue is DC4.

to an axis one wire correctly reconstructed the original electron while the other wire missed the particle and later reconstructed a background hit. Actually, the hit caused by a spark or a second electron occurred at a random time. The events on the diagonal are those in which both wires missed the triggered electron but were both able to reconstruct the same background event. All the remaining points are events in which the two wires reconstructed different background events. Finally, the events with no hits in at least one direction are not shown in the figure but are considered for the total number of events. The ratio between all events in the chamber area divided by all events, gave the efficiency of the chamber. This method slightly overestimated the efficiency of the chamber by not subtracting the background events in the chamber area. This was not a problem since the goal of the test was to compare the result in 2006 with the one of the previous year. Results from this method are presented in Figure 2.14. The same discontinuity in the efficiency observed in Figure 2.11 is also seen here. The efficiency evaluated with this method for the original gas mixture was 91%.

It is clear from Figure 2.14 that DC3 had a significantly lower efficiency than the other chambers. This was reflected in the DC34y result in Figure 2.11. Combining the two

Energy (GeV)	DC1 (mm/ns)	DC2 (mm/ns)	DC3 (mm/ns)	DC4 (mm/ns)
1.5	0.0289	0.0301	0.0317	0.0327
2	0.0292	0.0305	0.0325	0.0333
3	0.0290	0.0301	0.0322	0.0331
4	0.0290	0.0303	0.0322	0.0332
5	0.0288	0.0304	0.0321	0.0336
6	0.0294	0.0303	0.0328	0.0334

Table 2.1: Drift velocity in the four chambers for six typical runs covering all the energy range of the DESY test beam.

results, the problem could be associated with the y reconstruction of DC3. The reason of the problem was not discovered. Concerning the goal of the study, determining if the new gas mixture was usable, both methods showed that there was a reduction in performance using the new mixture. However this was considered acceptable and the change in the gas mixture was approved. The second method was also used to choose the working point of the chambers; during the test beam all chambers were operated at 1500 V.

2.4.3 Drift velocity calculation

The measurement of the drift velocity is crucial for good chamber resolution and track reconstruction. Since the relative alignments of the chambers were not known and the only information obtained from each chamber was the time between the trigger and the hit on the wire for both directions, the system was under-constrained.

In order to estimate the drift velocity in each chamber, the time measured in the chamber was compared with the centre of gravity of the shower in the calorimeter. Assuming a beam orthogonal to the chamber and negligible misalignment, the ratio of the two quantities gives the drift velocity in the chamber. A typical distribution for one of the chambers is shown in Figure 2.15. This procedure requires good alignment between chambers and calorimeter; since the calorimeter and the chamber were offset by 50 mm along y, the measurement was performed only for the x direction which was aligned to better than a mm. The evaluated drift velocity was used for both directions; this was possible because of the design of the chamber. Table 2.1 summarises the

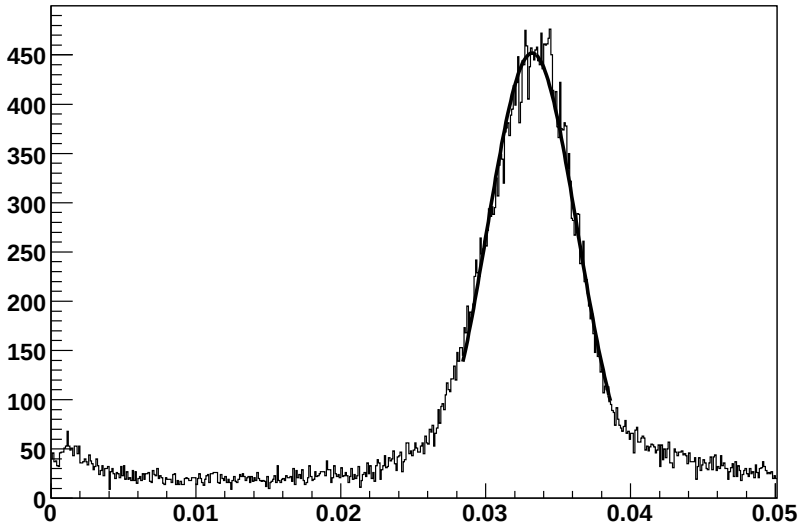

Figure 2.15: Plot of the ratio between the ECAL position and the drift chamber time for chamber four in the 6 GeV run.

result of this method for seven runs covering all energies used during the DESY test beam. The system was very stable from run to run with variation smaller than $\sim 3\%$. The small differences between chambers were likely due to different gas pressures and possibly chamber misalignment.

2.4.4 Intrinsic resolution evaluation

The intrinsic resolution of the chambers is needed in the digitisation of the tracking chambers in the Monte Carlo simulation described in Section 2.3.4. Without the correct smearing of the simulated hits, the contribution of the tracking resolution to any study of the performance of the calorimeter would be wrong.

2.4.4.1 Statistical technique

To evaluate the intrinsic resolution of the chamber, assumed identical in all drift chambers, the data of Table 2.1 were used. A linear function was used to fit the four reconstructed points along x, giving two degrees of freedom (four points minus two parameters of the linear fit). For each event the variable S, defined in equation 2.1, was calculated:

$$S = \sqrt{\sum_{i=1}^{n} \left(y_i - f\left(x_i;\theta\right)\right)^2}. \tag{2.1}$$

where $y_i$are the measured points and $f(x_i;\theta)$ is the linear function used to fit them evaluated at the points x_i. This variable is exactly the square root of the numerator of the usual χ^2 variable assuming identical errors for all the measurements, i.e:

$$\chi^2 = \frac{\sum_{i=1}^{n} \left(y_i - f\left(x_i;\theta\right)\right)^2}{\sigma^2} = \frac{S^2}{\sigma^2}. \tag{2.2}$$

Since the χ distribution for two degrees of freedom (n_{dof}) has mode equal to 1, it is possible to evaluate the error from the distribution of S:

$$\hat{\sigma} = \frac{mode[S]}{\sqrt{n_{dof} - 1}}. \tag{2.3}$$

The effect of the backgrounds, such as sparking in the chamber or double particle events, is a long tail at high values of S. The mode of the distribution is not as affected as the mean by these effects, hence is a better estimator.

Knowing the errors for several energies, it was possible to disentangle the contribution from multiple scattering and intrinsic chamber resolution. The Monte Carlo simulation of the test beam was used to evaluate the two contributions.

2.4.4.2 Analysis

To estimate the mode of the S distribution, the peak region was fitted with a bifurcated Gaussian distribution defined as

$$\begin{aligned} &\text{if } x < \mu \quad G(x) = Ae^{-\frac{1}{2}\frac{(x-\mu)^2}{\sigma_L}} \\ &\text{if } x > \mu \quad G(x) = Ae^{-\frac{1}{2}\frac{(x-\mu)^2}{\sigma_R}}. \end{aligned} \tag{2.4}$$

with A, μ, σ_L and σ_R free parameters. The fit range of the distribution was defined as all the bins with a content greater than a fraction of the maximum; this fraction was varied between 20% and 80% and this is equivalent to a scan in the fitting range.

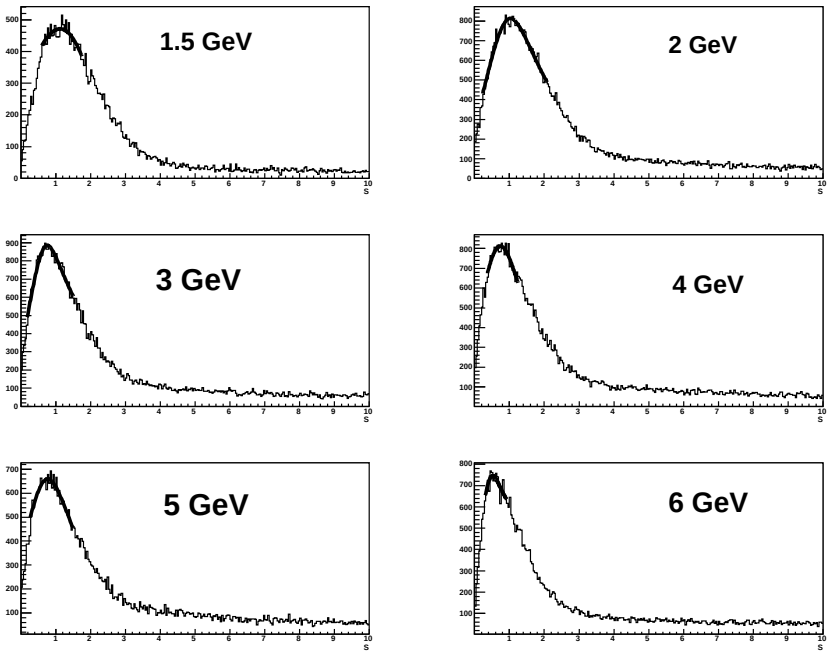

Figure 2.16: S distribution for all runs (from 1.5 GeV in top left to 6 GeV in bottom right). The fit was performed with a bifurcated Gaussian distribution.

Figure 2.16 shows the best fit to the S distributions for all energies. The best fit was chosen as the one giving the $\frac{\chi^2}{n_{dof}}$ closest to 1.

A variation of the fitting range could produce a fluctuation of the estimated mode larger than the statistical error. The study of this systematic effect was performed varying the fitting range; the systematic error was defined as the difference between the value of the maximum obtained having a χ^2-probability of 10% and 90%.

2.4.4.3 Monte Carlo simulation

Two different values for the smearing in the digitisation of the chambers were used: 0 mm and 0.5 mm. The former represents perfect reconstruction while the latter is close to the estimated intrinsic resolution of the chambers.

Since multiple scattering is an effect that decreases with the energy ($\propto 1/E$) while the intrinsic resolution should be constant, the following function was used to fit the data:

$$\hat{\sigma} = \frac{\mathrm{p0}}{E} \oplus \mathrm{p1}, \tag{2.5}$$

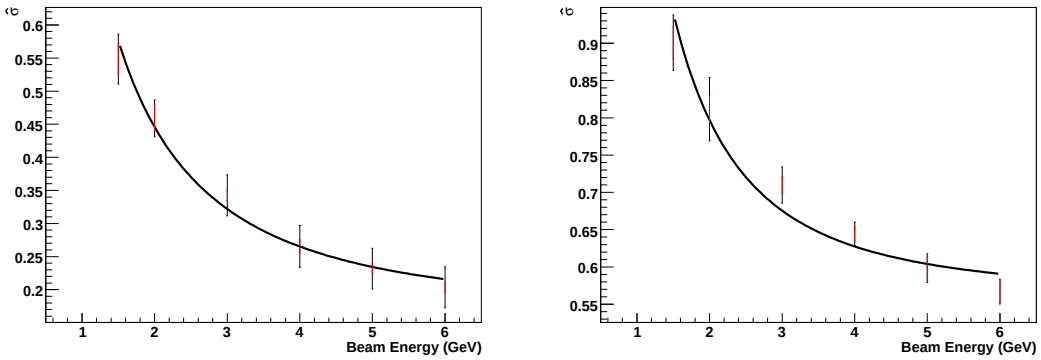

Figure 2.17: Fit of the resolution using Equation (2.5) for Monte Carlo assuming perfect reconstruction (left) and 0.5 mm resolution (right) in the drift chambers.

where the two terms are added in quadrature since they should be independent. The fits performed on the Monte Carlo simulations with perfect reconstruction and 0.5 mm resolution are presented in Figure 2.17. The red lines represent the statistical errors while the black ones are the sum of statistical and systematic errors; the two simulations had different contributions from the two types of errors. The χ^2 were 1.4 and 6.6 respectively for four degrees of freedom. The estimated resolutions, the constant terms from the fit, were not in perfect agreement with the input values of 0 mm and 0.5 mm: in the case of perfect reconstruction the estimated resolution was 0.17 ± 0.03 mm while the estimated reconstruction when the digitisation was performed using 0.5 mm was 0.56 ± 0.01 mm. The latter value was more relevant than the former since it was close to the real value of the chambers. Given the discrepancy in the Monte Carlo reconstruction, the method appears to have a systematic error of about 0.05 mm.

2.4.4.4 Best fit to the simulation

Another approach was used to analyse the same simulation. Instead of using the function which reflected the physics interpretation of the process, it was possible to use a function that better fitted the simulation and obtain a prediction closer to the input values. Such a function was

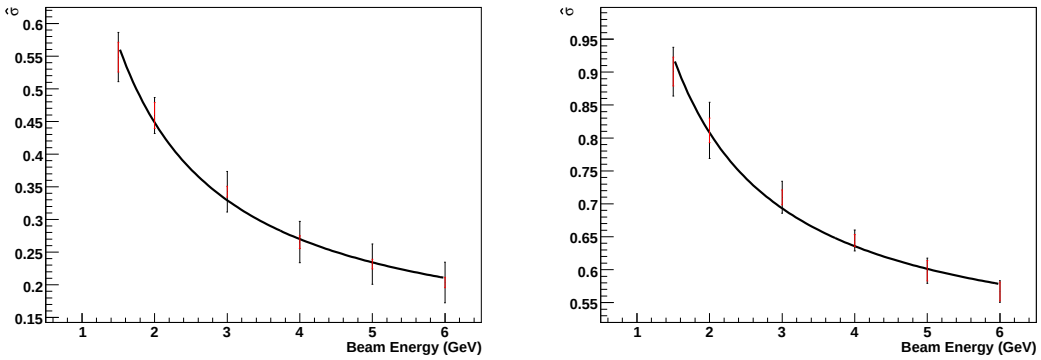

Figure 2.18: Fit of the resolution using Equation (2.6) for Monte Carlo assuming perfect reconstruction (left) and 0.5 mm resolution (right) in the drift chambers.

χ^2/dof	Perfect reconstruction	0.5 mm reconstruction
using Eq. (2.5)	1.373/4	6.595/4
using Eq. (2.6)	0.6573/4	1.627/4

Table 2.2: χ^2/ndf for the functions 2.5 and 2.6 fitting the two Monte Carlo simulations.

$$\hat{\sigma} = \frac{\mathrm{p0}}{E} + \mathrm{p1}. \tag{2.6}$$

In this case the two terms are simply summed rather than summed in quadrature. The fits to the same points presented in Figure 2.17 are shown in Figure 2.18. Table 2.2 shows the χ^2 and Table 2.3 shows the performance in reconstructing the input resolution obtained with the two functions for the two Monte Carlo samples. It is clear that the Equation (2.6) obtained better performances than Equation (2.5) when fitting the simulation; the reason is not understood.

2.4.4.5 Fit to the data

Equations (2.5), sum in quadrature, and (2.6), linear sum, were used to fit the data. The fits are presented in Figure 2.19 while the fitted parameters are summarised in

Fitted intrinsic resolution	Perfect reconstruction	0.5 mm reconstruction
using Eq. (2.5)	0.17 ± 0.03	0.56 ± 0.01
using Eq. (2.6)	0.09 ± 0.03	0.46 ± 0.02

Table 2.3: Fitted intrinsic resolution using the functions 2.5 and 2.6 fitting the two Monte Carlo simulations.

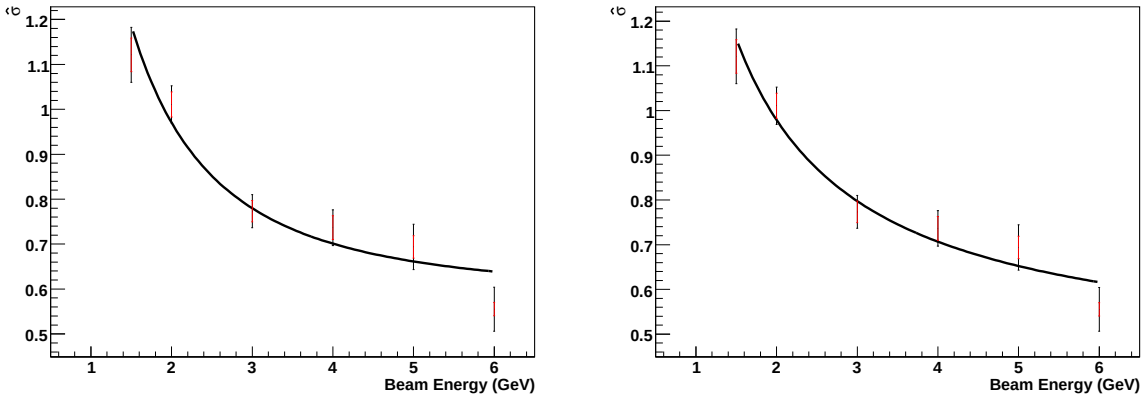

Figure 2.19: Fit of the resolution using Equations (2.5) (left) and (2.6) (right) for the DESY test beam data.

Using Eq. (2.5)	Multiple scattering term (mm)	Constant term (mm)
Data	1.55 ± 0.09	0.58 ± 0.03
MC perfect resolution	1.13 ± 0.07	0.17 ± 0.03
MC 0.5 mm resolution	0.83 ± 0.05	0.56 ± 0.01

Table 2.4: Results for the intrinsic resolution of the DESY drift chambers for data and Monte Carlo using the sum in quadrature of multiple scattering and intrinsic resolution terms.

Tables 2.4 and 2.5.

A common result from both fits was a higher value for the multiple scattering term in the data than in the Monte Carlo. This is an indication that the material in the simulation was not as much as the material in the real test beam.

The model described by Equation (2.5) (sum in quadrature) gave a chamber intrinsic resolution of $0.58 \pm 0.03 \pm 0.05$ mm. The systematic error was due to the result on the Monte Carlo simulation described in Section 2.4.4.3. Moreover, the multiple scattering term in the simulations with 0 and 0.5 mm resolution was not compatible. This is expected to be unchanged since the simulation model is the same and the multiple scattering should be independent from the digitisation. For these reasons I

Using Eq. (2.6)	Multiple scattering term (mm)	Constant term (mm)
Data	1.1 ± 0.1	0.43 ± 0.04
MC perfect resolution	0.69 ± 0.07	0.09 ± 0.03
MC 0.5 mm resolution	0.71 ± 0.08	0.46 ± 0.02

Table 2.5: Results for the intrinsic resolution of the DESY drift chambers for data and Monte Carlo using the sum of multiple scattering and intrinsic resolution terms.

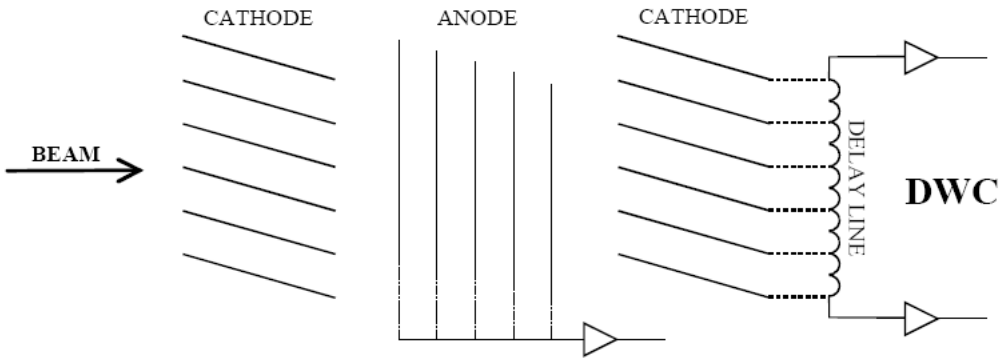

Figure 2.20: Structure of the tracking chamber used in the CERN test beams (from [12]).

consider Equation (2.6) to provide a better description of the problem: the reconstructed intrinsic resolutions from the Monte Carlo were in agreement with the input values and the multiple scattering term was similar in the two simulations. Using this model the intrinsic resolution of the DESY beam chambers was estimated to be $0.43 \pm 0.04\,\mathrm{mm}$.

2.5 The CERN tracking system

The commissioning of the CERN tracking system is described in this section. After the description of the chambers, their calibration and alignment are presented. Then the efficiency of the tracking system is evaluated. Both 2006 and 2007 beam line data are analysed; due to the different knowledge of the beam line, different approaches have been taken for the two periods. These studies are relevant for optimising the track reconstruction which is needed for the study of position and angular resolution presented in Section 2.6.

2.5.1 CERN Delay Wire Chambers (DWC) description

The three chambers used to perform the track reconstruction in the CERN test beam were provided by CERN. The chambers had a typical "sandwich" structure of two cathode planes with a central anode wire-plane (Figure 2.20). The signal of the

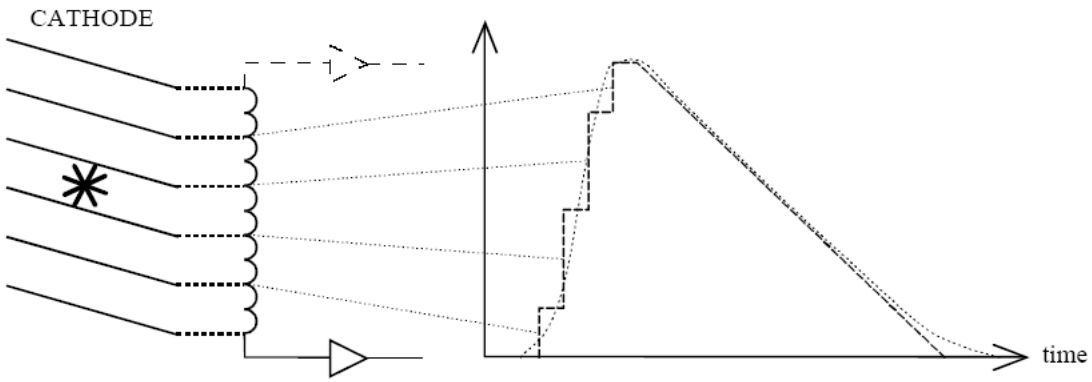

Figure 2.21: The travelling wave is built up by adding up the single inputs in the delay line (from [12]).

charged particle was read out by a delay line connected to the cathode wire-plane (Figure 2.21). The induced signal from the cathode wires built up two waves in the delay line, one in each direction. Subtracting the two times from the delay lines, it was possible to reach a resolution ten times better than the wire spacing. A second sandwich structure, orthogonal to the first, was used to measure the impact point in the other direction. All signals produced in the chamber were discriminated before being read by the TDC. The output of the TDC was recorded by the DAQ. The active area of the chamber was 64 cm^2 while the intrinsic resolution was better than 200 μm [12].

2.5.2 Calibration of DWC

During the commissioning of the beam line in 2007, a dedicated run was performed in order to calibrate the chambers as described in [12]. This procedure had not been performed in 2006. However, since the chambers were the same, the values found in 2007 could also be used for the chamber reconstruction of the 2006 data.

Each chamber could be injected with a signal at three different points in x and y. The three injection points were plotted as function of the reconstructed times and fitted to find the propagation velocity and the electronic offset. A typical fit is presented in Figure 2.22 and the results for all the chambers are summarised in Table 2.6. For the first two chambers the error on the propagation velocity was about 3%,

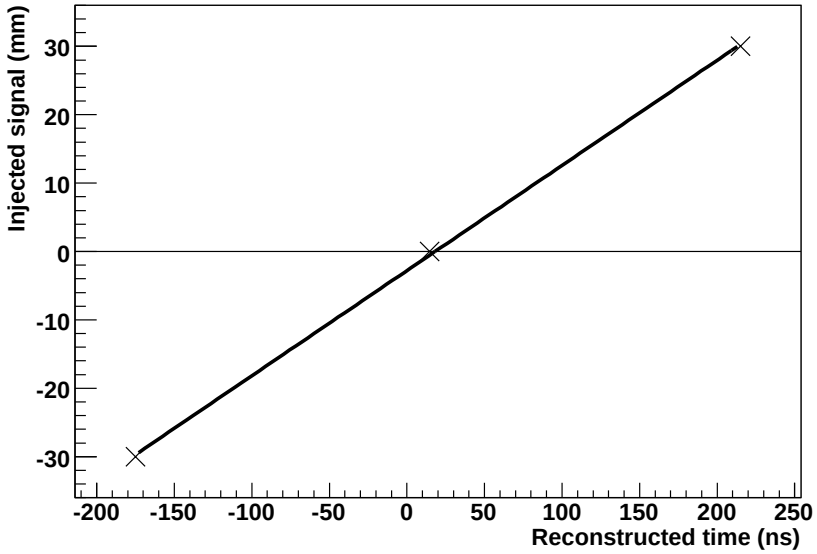

Figure 2.22: Calibration procedure of a tracking chamber at CERN. The injection points are plotted as a function of the reconstructed times. From the fit it is possible to evaluate the propagation velocity and the electronic offset of the chamber.

Wire	Slope (mm/ns)	Offset (mm)	Slope using two points (mm/ns)
dc1x	0.154 ± 0.004	-2.8 ± 0.6	0.158
dc1y	0.150 ± 0.004	-0.7 ± 0.6	0.150
dc2x	0.171 ± 0.004	-1.4 ± 0.6	0.176
dc2y	0.173 ± 0.004	-1.7 ± 0.6	0.150
dc3x	0.143	-0.7	-
dc3y	0.148	-0.6	-

Table 2.6: Summary of the calibration of the CERN tracking chambers. There are no measurement errors for DC3 because the wire used in the calibration was broken.

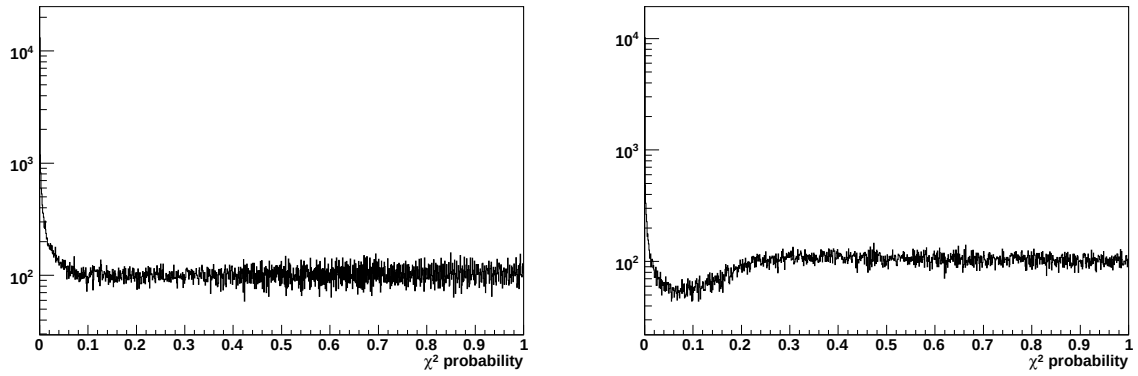

Figure 2.23: χ^2-probability distribution for the best propagation velocity in x (left) and y (right).

leading to an error smaller than 0.2 mm in the central part of the chamber as claimed by the constructor [12].

Unfortunately in one of the drift chambers an internal wire was broken giving only two points to perform the fit. The last column of Table 2.6 shows the "fit" for only two points for the first two chambers. The difference between the second and the last columns of the table was too large (from 0.173 ± 0.004 to 0.15 in dc2y) to allow the use of the value found for the third chamber. Thus a further analysis was performed to optimise the propagation velocity.

A sample of well reconstructed tracks must have a flat χ^2-probability distribution; the optimum value of the propagation velocity was chosen as the one giving the flattest slope. A linear fit was performed between 0.5 and 1 of the χ^2-probability to evaluate the slope. Figure 2.23 shows the χ^2-probability distribution for the best values of the propagation velocity for x (0.14 mm/ns) and y (0.18 mm/ns), while in Figure 2.24 the same distribution are presented for a "wrong" propagation velocity. The difference in slope is clearly visible. The slope of the χ^2-probability as a function of the propagation velocity is shown in Figure 2.25.

The error on the two velocities was evaluated using the results presented in Figure 2.25; for the x direction the slope changes rapidly around the zero of the probability, therefore the estimated error was small, of the order of 0.005 mm/ns, leading to a relative error of 3.6%. For the y direction the zero was never reached and the region

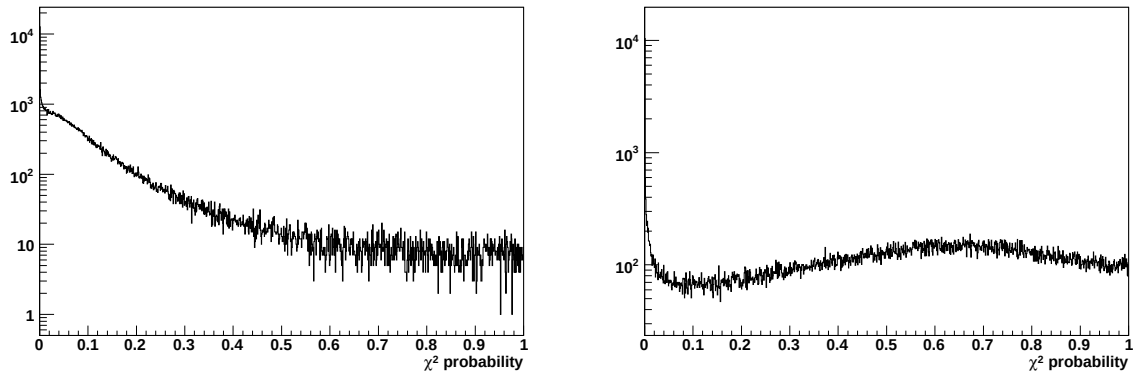

Figure 2.24: χ^2-probability distribution for a bad propagation velocity. For x direction (left) 0.18 mm/ns is used instead of 0.14 mm/ns, for y direction (right) 0.14 mm/ns is used instead of 0.18 mm/ns.

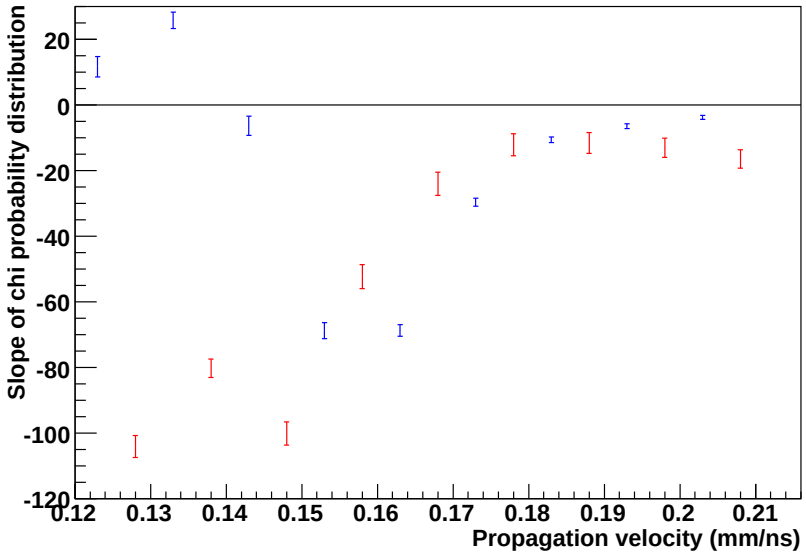

Figure 2.25: Slope of the χ^2-probability as a function of the propagation velocity in DC3. Red is y direction, blue is x direction.

close to zero had a large plateau around the chosen value. In this case the error was estimated to be 0.01 mm/ns, equivalent to a relative error of 5.6%.

In conclusion, the tracking chambers of the CERN test beam was calibrated using the standard procedure and a further study. The measured resolution for the DC1 and DC2 was the nominal (0.2 mm). The broken wire in DC3 meant that the calibration could not be determined directly. The alternative procedure provided a resolution of about 0.2 mm in x and 0.4 mm in y.

2.5.3 Alignment

In 2007 the drift chambers were aligned to the beam line during the survey with a precision of 200 μm.

In 2006 such a survey was not performed. To measure the alignment of the chambers a 50 GeV electron run was used. Having negligible multiple scattering deviation, the three hits should be aligned within the chamber intrinsic resolution (200 μm). The distance between the hits along the x and y axis in the chambers was used to align the chambers between themselves assuming that the chambers were orthogonal to the beam. Since the angle between beam and chambers for the 2007 data was about 0.5 mrad, this assumption was valid. This angle caused a shift between the hits in the first and last chamber of 0.2 mm, small enough for this study. The precision achieved with this procedure was about 1 mm. This value is the sigma of the distribution of the relative distances; a typical distribution is presented in Figure 2.26.

The tracking system then needs to be aligned to the calorimeter. The distance between the reconstructed impact point on the calorimeter and the barycentre of all hits in the calorimeter was used to evaluate this offset.

2.5.4 Tracking efficiency

A fully reconstructed track required 12 signals: two from each of the x and y wires in each of the three chambers. The efficiency of the tracking system, defined as the ratio between the events with at least the minimum 12 signals over the total number

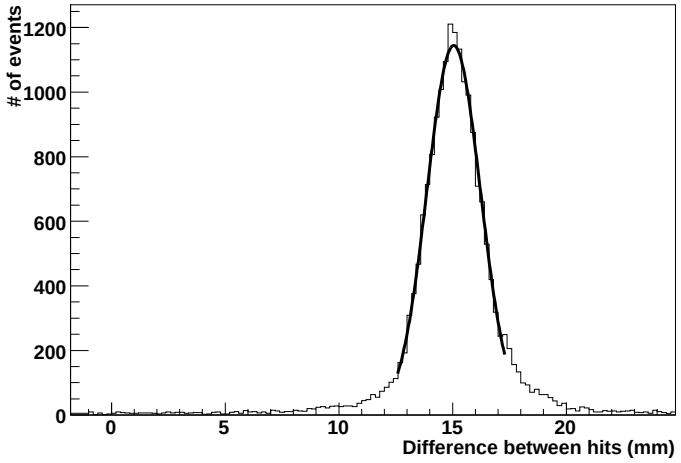

Figure 2.26: Distribution of the difference of two hits in different chambers. The sigma of the distribution gives the precision of the alignment procedure that is about 1 mm.

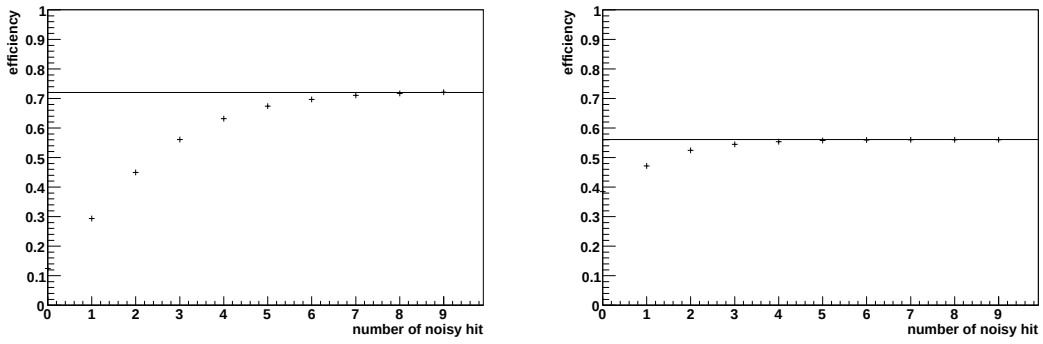

Figure 2.27: Efficiency of the tracking system for the 2006 (left) and 2007 (right).

of events, is shown as a horizontal line in Figure 2.27 for 2006 (left) and 2007 (right) data. The chambers had some noise (sparks, double particle events, electronic noise) that could increase the number of signals. The same figure shows the efficiency as a function of the maximum number of extra hits in the chambers. For the following studies, the maximum number of extra signals chosen for the 2006 data was 6, while for the 2007 data it was 3. The difference in performance between the two periods was due to a difference in the discriminator level.

Figure 2.28 shows the efficiency of the tracking system as a function of the beam energy. The beam spread was the main cause of the energy dependence. In a larger beam there is a higher chance for a particle to miss one chamber or passing through the external part of the chamber that is less efficient (see [12] for details in chamber

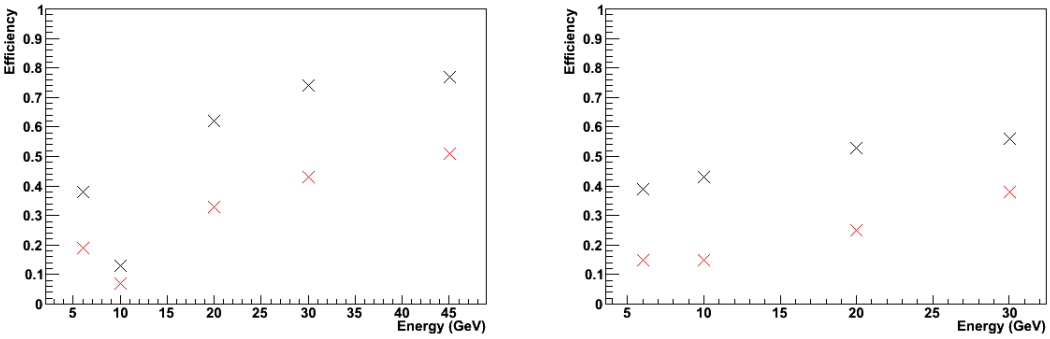

Figure 2.28: Efficiency of the tracking system as a function of the energy for the 2006 (left) and 2007 (right) data; for all reconstructed tracks (black) and for tracks with $\chi^2 < 5$ (red).

design and performance). Since the collimation of the beam increased with the energy, the efficiency increased as well. The low efficiency for the 10 GeV run in 2006 (left plot) was caused by a malfunction of the TDC that did not work for a large part of the run.

2.6 Position and angular resolution of the electromagnetic calorimeter

The energy resolution is often regarded as the most important parameter of a calorimeter. However, for a particle flow optimised calorimeter, the energy resolution is not the only relevant parameter. The segmentation plays a central role for minimising the "confusion term" of the jet energy resolution since high segmentation enables better cluster separation. Increased segmentation also improves the position resolution of each cluster therefore reducing the confusion due to a wrong association of clusters to tracks. In order to validate the simulations performed with the particle flow algorithms, it is important to study these effects in a real calorimeter and if possible determine the required segmentation for the final detector design.

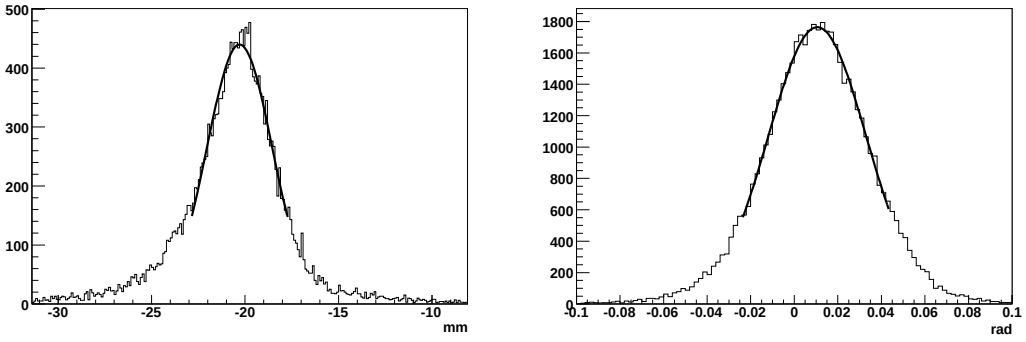

Figure 2.29: Examples for the evaluation of the position (left) and angular (right) resolution. The fit is performed between -1.5 and 1.5 sigma.

2.6.1 Definition of position and angular resolution

The calorimeter position was reconstructed using the centre of gravity (COG) in both directions from all reconstructed hits in the calorimeter as described by the formula:

$$\overline{X} = \frac{\sum_{i=0}^{i=N} x_i E_i}{E_{tot}},$$

where E_i and x_i are the energy and the position of the i-th hit, and N is the total number of hits above the standard 0.6 MIP threshold. E_{tot} is the total energy in the calorimeter. Similarly the angles with respect to the x and y axes were calculated using the formulas:

$$\Phi = \text{atan}\left(\frac{\hat{y}}{\hat{z}}\right), \theta = \text{atan}\left(\frac{\hat{x}}{\hat{z}}\right),$$

with $\hat{x}$ and $\hat{z}$ the eigenvectors of the cluster formed by all the hits. These definitions were used for the data and the Monte Carlo simulation.

The difference between the COG of the cluster and the extrapolation of the track to the centre (in z) of the cluster was used to evaluate the position resolution of the calorimeter; the same was done for the angles. Figure 2.29 shows two typical distributions used to evaluate the position and the angular resolution; the plots were obtained from a 20 GeV electron run. The 20 mm deviation was set in order to centre the beam on the central wafer of the calorimeter. The calorimeter was not perfectly orthogonal to the beam, having an angle of 0.01 rad with respect to the beam.

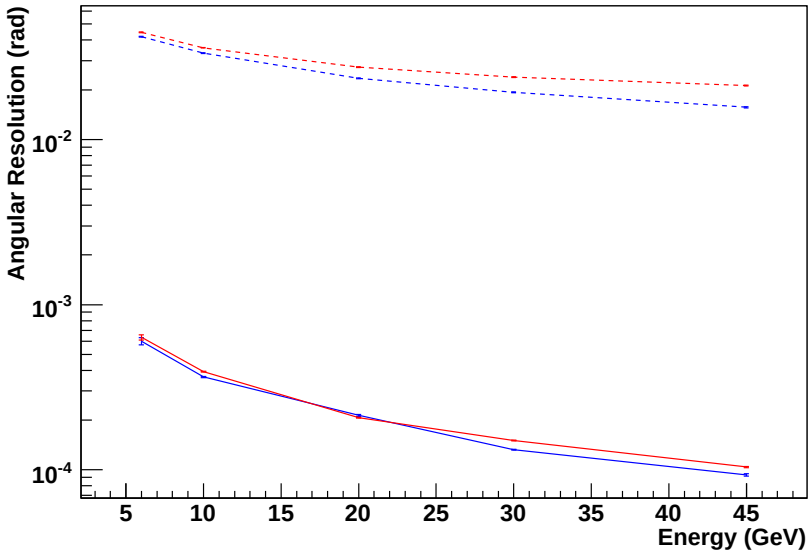

Figure 2.30: Angular resolution of the calorimeter (dotted line) as evaluated from the Monte Carlo. The continuous line are the angular resolution for the tracking system. Red lines are the resolution along the y direction, blue along the x direction.

2.6.2 Use of the tracking system

Given the definition of position and angular resolutions, the tracking resolution has to be as good as or better than the calorimeter resolution in order to determine the latter. In order to establish this, the tracking and the calorimeter resolutions were estimated using the Monte Carlo described in Section 2.3.4.

The difference between the x, y, Φ and θ reconstructed by the tracking system and the calorimeter and those obtained from the Monte Carlo information at the front face of the calorimeter gave distributions similar to those of Figure 2.29. The standard deviation of these distributions as a function of the beam energy are shown in Figures 2.30 and 2.31 for the angular and position resolution respectively.

Figure 2.30 shows that the angular resolution of the tracking system was smaller than 1 mrad, while the calorimeter angular resolution was always larger than 20 mrad. Therefore the requirement of having a small contribution from the tracking system was satisfied.

For the position resolution the situation was more complicated. In fact the tracking resolution was larger than the calorimeter resolution for energies below 20 GeV.

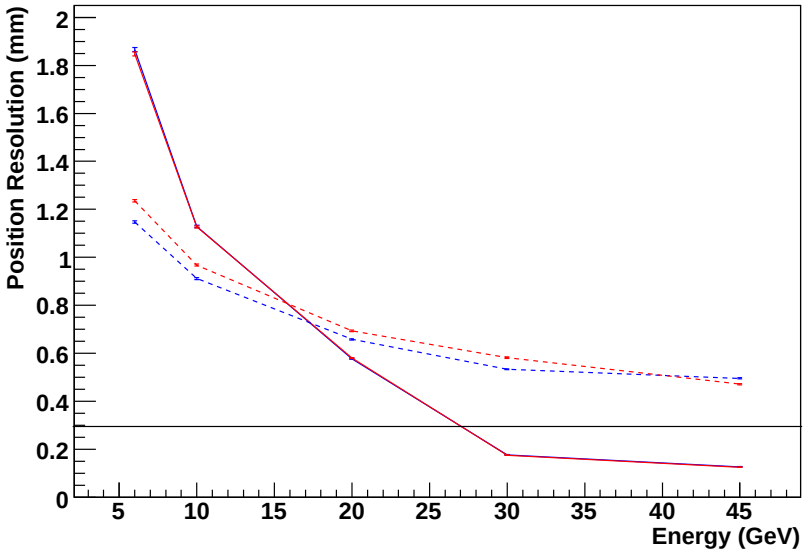

Figure 2.31: Resolution of the calorimeter (dotted line) as evaluated from the Monte Carlo; in red along the y direction, in blue for the x direction. The continuous line is the contribution to the tracking resolution from the multiple scattering (colour) and due to the intrinsic resolution of the tracking chambers (black).

The tracking resolution shown in Figure 2.31 was evaluated assuming perfect reconstruction in the tracking chambers. This is an estimation of the multiple Coulomb scattering since any contribution from the intrinsic chamber resolution was excluded. The effect of the intrinsic chamber resolution is shown by the horizontal black line and corresponds to 0.3 mm. This was obtained assuming a resolution of 0.2 mm in all chambers. For the calorimeter position, the corrections described in Section 2.6.5 were applied.

Above 30 GeV, the tracking resolution was dominated by the intrinsic resolution of the chambers and at such high momenta the multiple scattering should not affect the tracking resolution. In the analysis of real data, runs with energy from 10 GeV were used to study the position resolution of the calorimeter while all energies were used for evaluating of the angular resolution.

2.6.3 Event selection

The techniques presented in Section 2.5 were used to produce well reconstructed tracks. For the angular and position resolution study a linear tracking was used: the

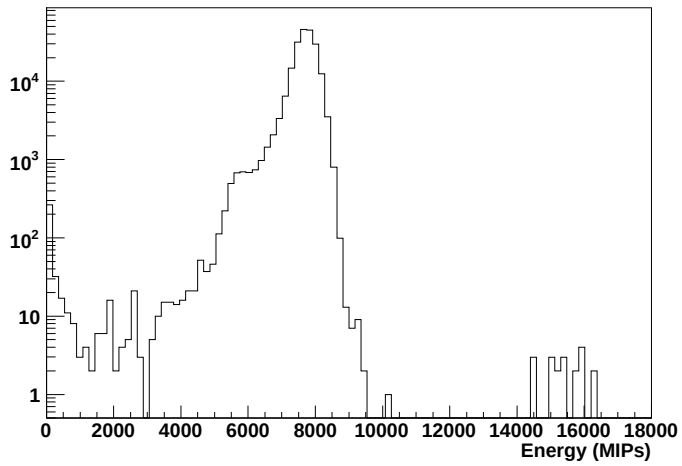

Figure 2.32: Energy distribution for a 30 GeV run. The energy is measured in MIPs.

two projections of the track on x and y were considered independently and for each projection a linear fit of the three reconstructed points was performed. In order to reconstruct a track, the same requirements of Section 2.5.4 were used and the cut $\chi^2 < 5$, which is equivalent to the cut χ^2-probability > 0.08, was placed to reject unlikely tracks. This cut was based on the distributions of Figure 2.23.

A simple filter was applied on the calorimeter data in order to select only those events with a single electron. A cut on the total energy in the calorimeter was used to discard double particle events and reduce possible pion contamination. Figure 2.32 shows a typical energy distribution for a 30 GeV electron run. The cuts were optimised to select only the peak region, in this case between 7200 and 8500 MIPs.

Since the tracking had a central role in the position resolution and the level of knowledge of the beam line in 2006 and 2007 was different (survey and calibration were performed only in 2007), the two data samples were studied separately.

2.6.4 Position and angular resolution

2.6.4.1 Resolution for 2006 data

The position and angular resolution were evaluated using runs with an electron beam "centred" on the middle wafer. This was done despite the fact that the beam was not well centred in the y direction, as visible from the plots in Figure 2.33. For this

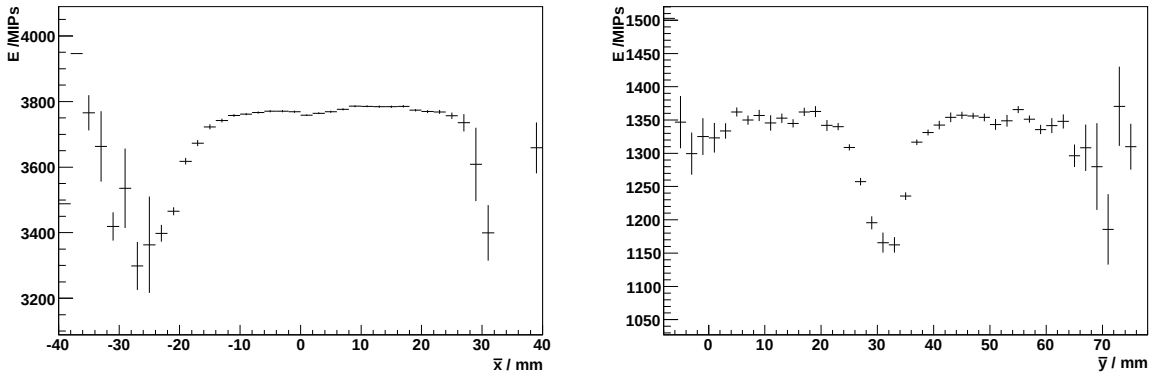

Figure 2.33: Measured energy in the calorimeter as a function of calorimeter impact point in the 2006 test beam; x projection on the left, y projection on right. The wafer gaps are visible at the edges of the left distribution and the middle of the right distribution.

setup, electron runs with an energy from 6 GeV to 45 GeV were available. For the studies on position resolution only energies above 10 GeV were used. Figures 2.34 and 2.35 show the position and angular resolutions as a function of the beam energy. The tracking resolution along x is worse than along y, affecting the position resolution which is worse along x than along y. Since the angular resolution is not affected by the tracking resolution, as described in Section 2.6.2, and the calorimeter is staggered along x but not along y, the angular resolution along θ is better than along Φ. With the limited knowledge of the beam line, and therefore of the real impact point, the calorimeter position resolution could be estimated to be less than 1.75 ± 0.01 mm for a 30 GeV electron.

2.6.4.2 Resolution for 2007 data

The position and angular resolution as a function of the beam energy are shown in Figures 2.36 and 2.37, respectively. The runs were chosen "centred" on the middle wafer as shown in Figure 2.38.

2.6.4.3 Comparison between 2006 and 2007 results

The results for the two periods are summarised in Tables 2.7 and 2.8. The angular resolution was similar for the two periods having most of the points overlapping within

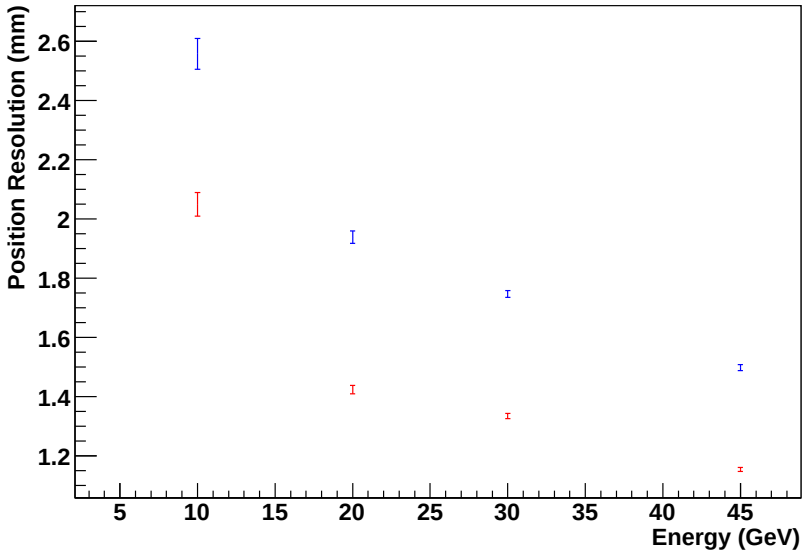

Figure 2.34: Position resolution for 2006 runs. In red the resolution along the y axis, in blue along x.

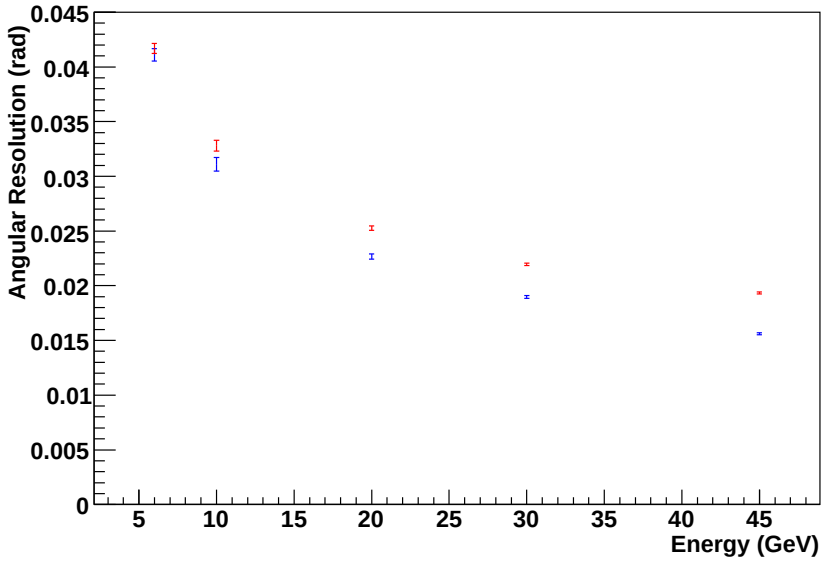

Figure 2.35: Angular resolution for 2006 runs. In red the resolution along the y axis, in blue along x.

Beam energy	Pos. 06 (mm)	Pos. 07 (mm)	Ang. 06 (mrad)	Ang. 07 (mrad)
6 GeV			41.1 ± 0.6	42 ± 1
10 GeV	2.56 ± 0.05	1.76 ± 0.02	31.1 ± 0.6	31.6 ± 0.4
20 GeV	1.94 ± 0.02	1.40 ± 0.02	22.7 ± 0.2	22.7 ± 0.2
30 GeV	1.75 ± 0.01	1.21 ± 0.01	19.0 ± 0.1	18.5 ± 0.1

Table 2.7: Summary of the position and angular resolution for the x axis for the two CERN test beam runs.

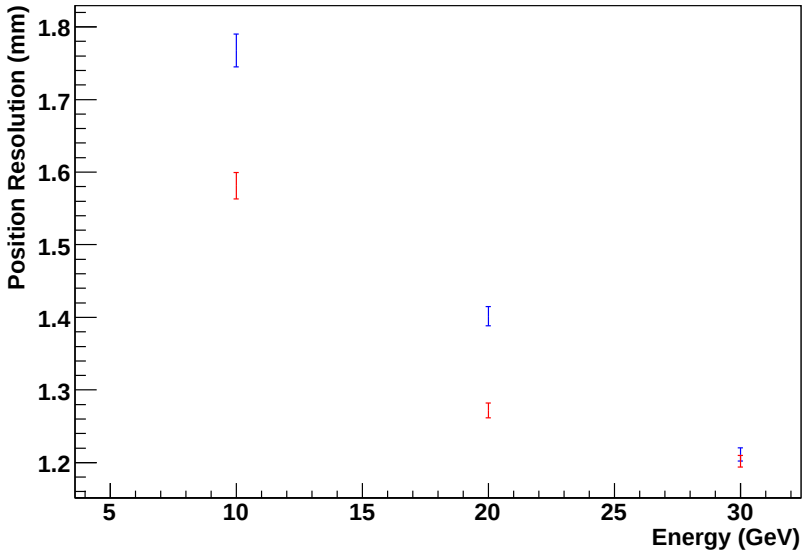

Figure 2.36: Position resolution for 2007 runs. In red the resolution along the y axis, in blue along the x one.

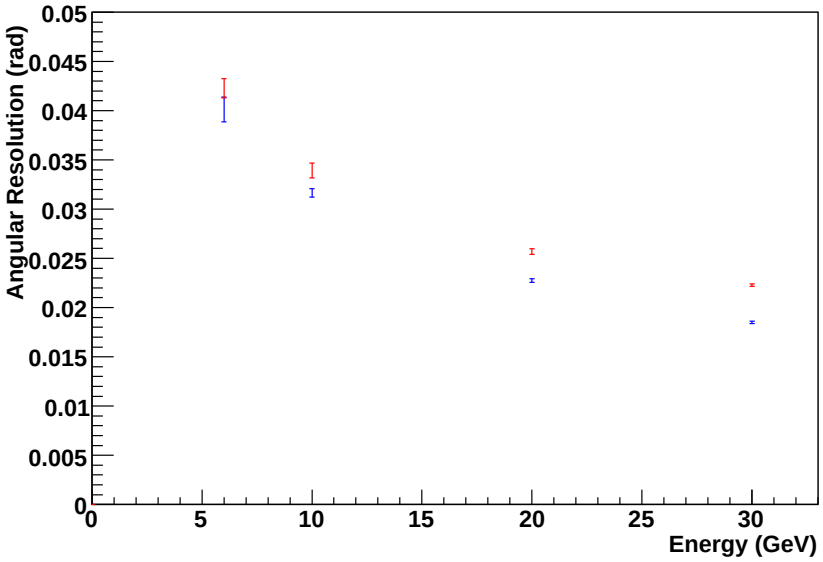

Figure 2.37: Angular resolution for 2007 runs. In red the resolution along the y axis, in blue along the x one.

Beam energy	Pos. 06 (mm)	Pos. 07 (mm)	Ang. 06 (mrad)	Ang. 07 (mrad)
6 GeV			41.7 ± 0.5	40 ± 1
10 GeV	2.05 ± 0.04	1.58 ± 0.02	32.8 ± 0.5	33.9 ± 0.7
20 GeV	1.42 ± 0.02	1.27 ± 0.02	25.3 ± 0.2	25.7 ± 0.3
30 GeV	1.33 ± 0.01	1.20 ± 0.01	22.0 ± 0.1	22.2 ± 0.1

Table 2.8: Summary of the position and angular resolution for the y axis for the two CERN test beam runs.

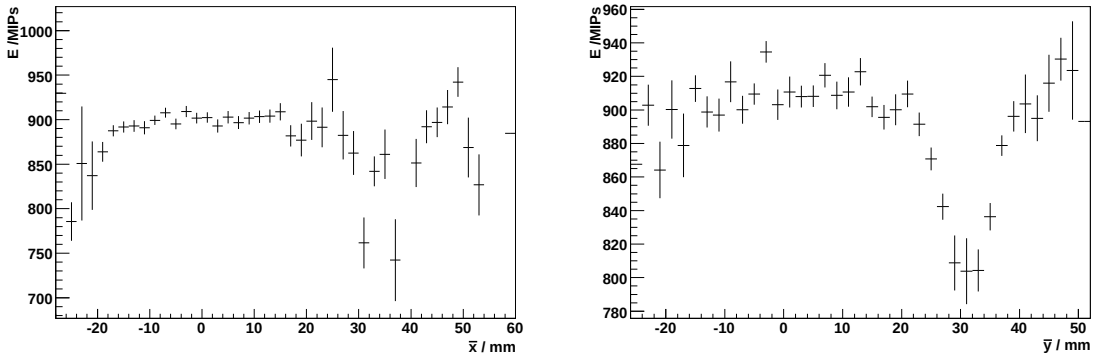

Figure 2.38: Energy deposited in calorimeter as function of calorimeter impact point in the 2007 test beam; x projection on the left, y projection on right. The wafer gaps are visible at the edges of the distributions.

one sigma; this confirms the low impact of the tracking on this measurement. The position resolutions along the x axis was worse in 2006 than in 2007. Since there was no difference in the calorimeter, the improvement presumably arose from a better knowledge of the tracking system. Along the y axis a smaller improvement was achieved for all energies. Since the result was still far from what could be achieved in the Monte Carlo as presented in Figure 2.31, an additional study was performed.

2.6.5 Corrections

In order to improve the results presented in Section 2.6.4, it is important to correct the distortions due to the 1×1 cm^2 cell structure of the calorimeter. The quantisation of the position measurement of each energy deposit results in a distortion of the centre of gravity measurement of a cluster. This distortion follows an S-shaped curve across each cell. A detailed description of this effect can be found in [13]. The effect can be corrected using a periodic function. However, the cell structure of the calorimeter was not homogeneous due to the gaps between the wafers as shown in Figure 2.33; this required a special treatment for the gap region.

Figure 2.39 shows the correlation plot of the impact position reconstructed with the calorimeter and the tracking for both directions for a 30 GeV data run. It is possible to see a difference between the two plots, due to the effect of the different staggering; in the x direction the planes were displaced as described in Section 2.2

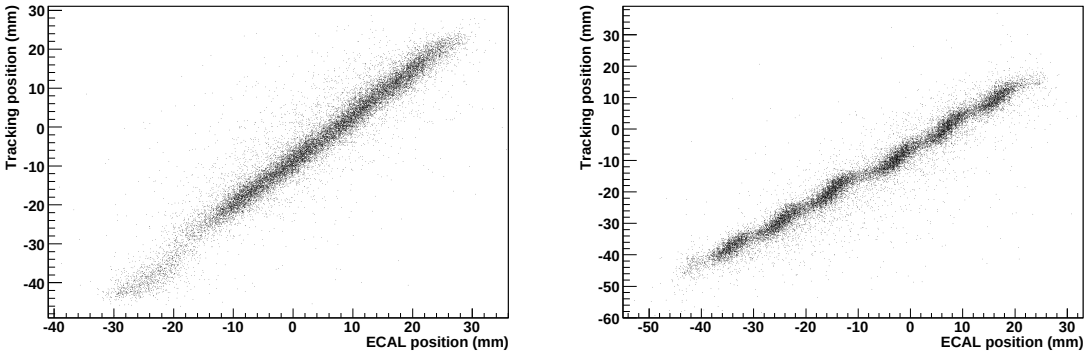

Figure 2.39: Correlation plot of the reconstructed impact position using the calorimeter and the tracking system. Projection along the x axis on the left and along the y axis on the right. The staggering on the x axis helps in reducing the *S-curve* effect.

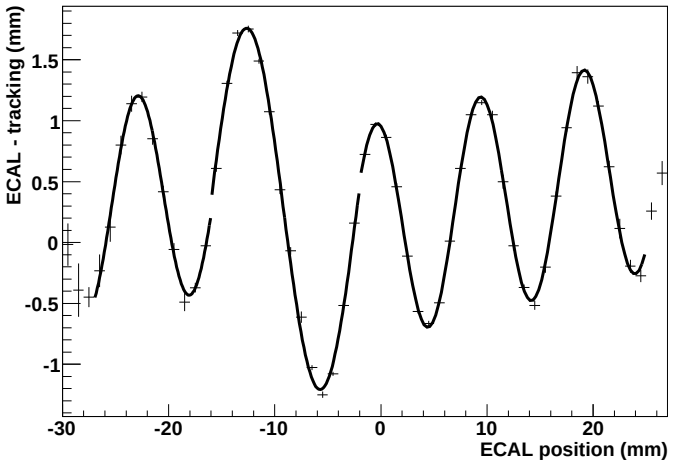

Figure 2.40: Typical fit used to estimate the corrections to the impact position due to the cell structure of the calorimeter. Three functions are used to fit the data in three different regions; two wafers, on the left and the right, and the inter-wafer gap in the middle. The functions reflect the structure visible in right plot of Figure 2.33.

while in the y direction there was no staggering. The ability to measure the effect depends also on the energy of the incoming particle since the tracking had a better resolution at high energy. This was a further reason to use high energy runs for this study.

The same effect is visible in the plot of the resolution as a function of the impact position; this plot was easier to fit with sinusoidal functions. An example of the fit is presented in Figure 2.40: three different functions were used to fit two different wafers (left and right fits) and the inter-wafer area (middle). Since the *S-curve* effect

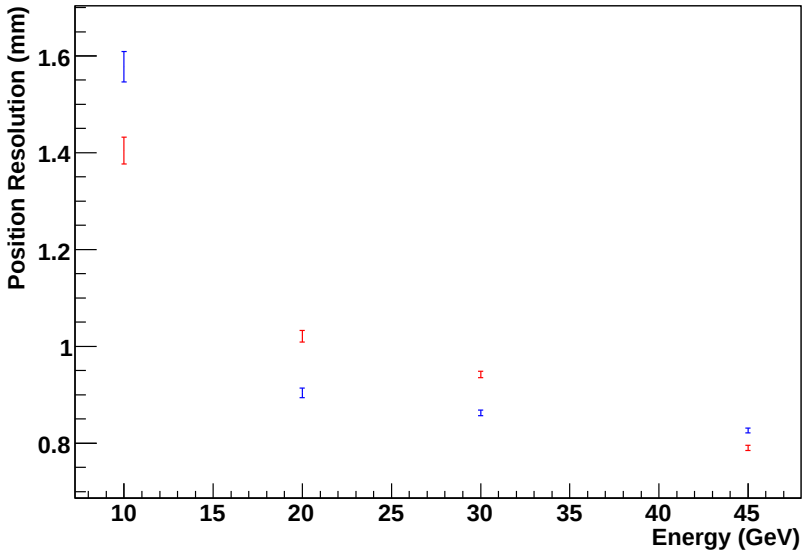

Figure 2.41: Position resolution for 2006 runs after applying the correction presented in Section 2.6.5. In red the resolution along the y axis, in blue along the x.

depended on the beam energy, each run was fitted independently.

Using the information from the fit it was possible to correct the calorimeter reconstructed point and improve the resolution. The position resolution of the calorimeter after this correction for the 2006 data is shown in Figure 2.41. The same plot for 2007 data is presented in Figure 2.42.

A clear improvement is visible when comparing the results of Figures 2.41 and 2.42 with Figures 2.34 and 2.36. However the position resolution was still not as good as the resolution obtained from the Monte Carlo presented in Figure 2.31. The difference was likely due to the contribution from the tracking; an under-estimation of the calorimeter resolution in the Monte Carlo could not be excluded.

2.6.6 Inter-wafer region

The analysis presented until now used runs with the beam centred close to the middle of the central wafer. This is not the most generic case and a study of resolutions when the beam is centred on the inter-wafer gap is also needed. To perform this analysis the runs of 2007 with the beam centred at the corner between four wafers in the same slab were used (point $[+3, +3]$ in Figure 2.43).

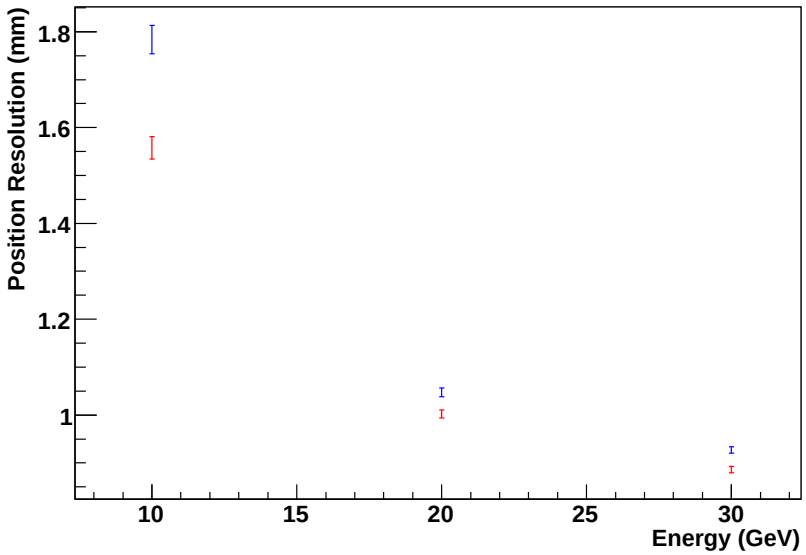

Figure 2.42: Position resolution for 2007 runs after applying the correction presented in Section 2.6.5. In red the resolution along the y axis, in blue along the x one.

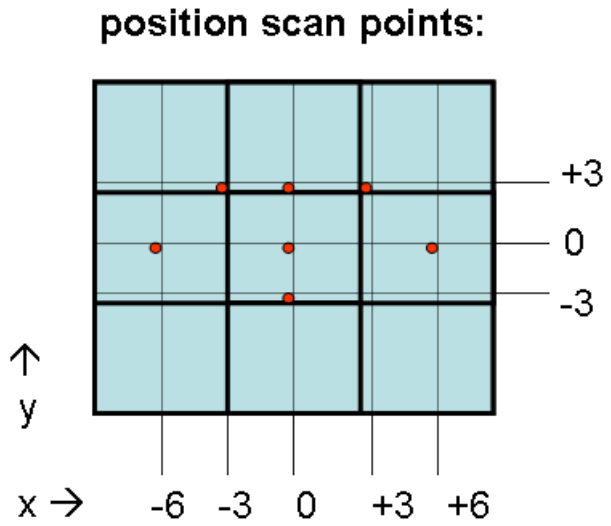

Figure 2.43: Front face of the electromagnetic calorimeter. The nine squares represent the nine silicon wafer while the red dots are the position at which the beam was aimed during the test beam. In this analysis the [0,0] and $[+3, +3]$ data are used.

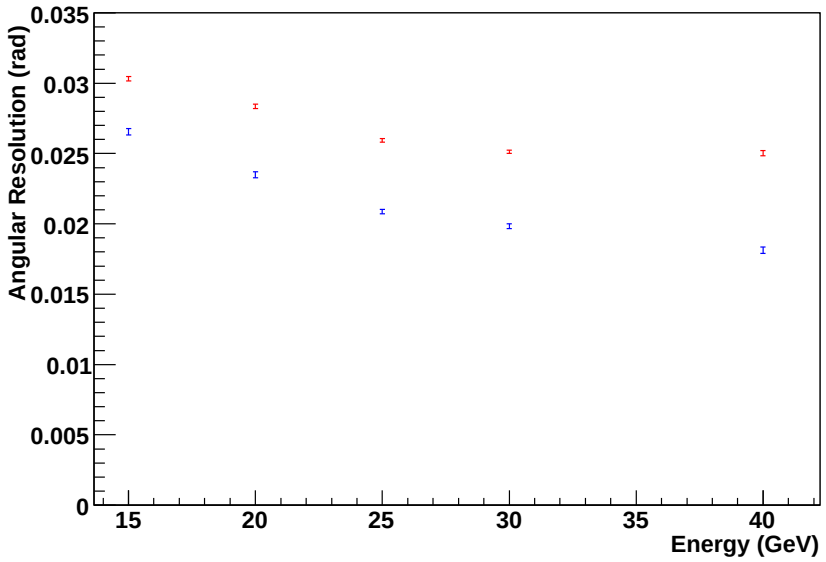

Figure 2.44: Angular resolution as function of beam energy for the inter-wafer region. In red the resolution along the y angle, in blue along the x.

The energy cuts were changed in order to include events in the gap region where a smaller amount of energy would be deposited in the calorimeter. The lower cut was set to 400 MIPs in order to eliminate only muon and pion events while the upper cut was not changed maintaining the function of cutting double particle events. After applying the correction described in Section 2.6.5, the angular and position resolutions obtained at different energies are shown in Figure 2.44 and 2.45 respectively.

The angular resolution was not different from the value obtained in the centre of the wafer; the reduced number of hits did not significantly affect the reconstruction of the cluster direction. The position resolution was affected by the gap. The corner region of the wafer had a lower resolution than the central region of the wafer. The position resolution for the x axis was worse than the y one because in this region the *S-curve* effect could not be corrected. Figure 2.46 shows that, along the x direction, the clear structure of Figure 2.40 disappears due to the combined effect of the staggering and the gap. Along y the structure was still visible as shown in Figure 2.47 and it was possible to apply the correction.

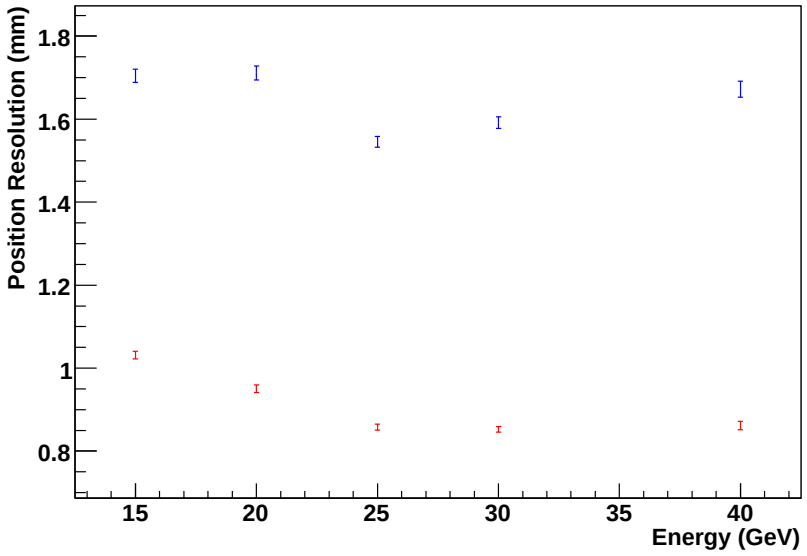

Figure 2.45: Position resolution as function of beam energy for the inter-wafer region. In red the resolution along the y axis, in blue along the x.

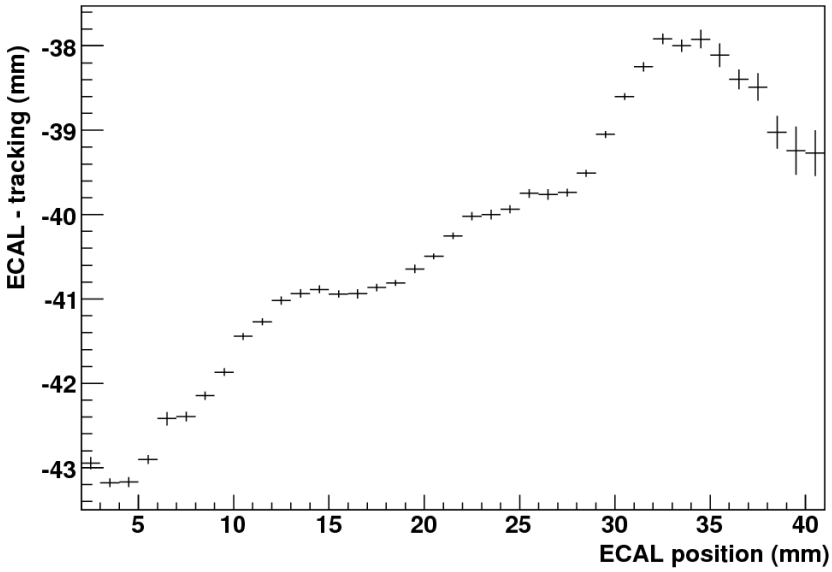

Figure 2.46: *S-curve* effect along the x axis in the gap region. The structure, clearly visible in Figure 2.40, is not visible in the corner region; for this reason it was not possible to apply the correction.

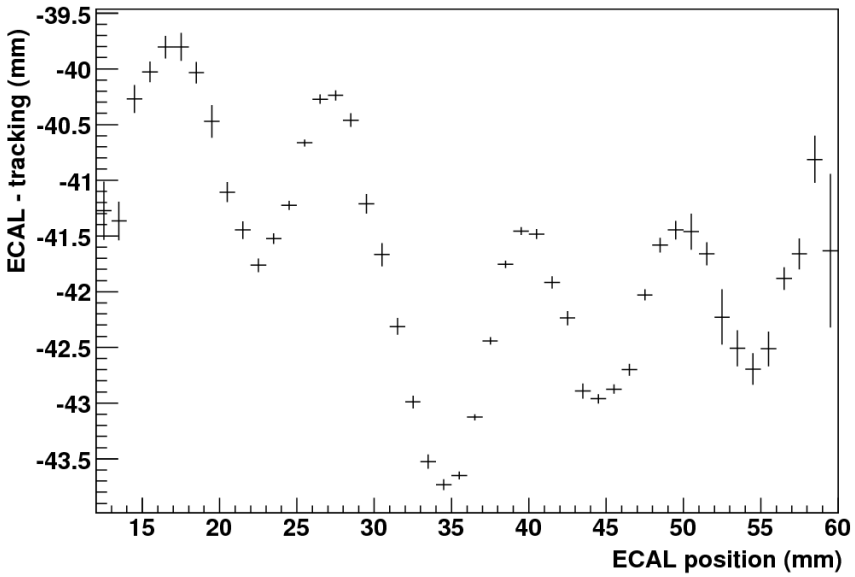

Figure 2.47: *S-curve* effect along the y axis in the gap region. In this case the structure is clearly visible and it was possible to apply the correction.

2.6.7 Conclusions and performance comparison

In this section the position and angular resolution, two crucial parameters of the electromagnetic calorimeter, have been evaluated. Using data from both years of test beam at CERN, the position resolution for electrons hitting the centre of a wafer is evaluated to be better than 0.9 mm for electrons above 30 GeV (see Figure 2.42). This value is an upper limit since it includes the tracking resolution contribution. The resolution worsens to 1.5 mm for the x axis when the electron hits the inter-wafer gap (see Figure 2.45); this effect is mainly due to the difficulties in correcting the *S-curve* effect in the gap region.

The angular resolution does not depend on the tracking and is estimated to be less than 30 mrad for electrons above 20 GeV in the centre of the wafer; a similar behaviour has been found for electrons passing through the inter-wafer gap. In both cases the resolution along the x direction is better than the y direction.

It is possible to compare this calorimeter to others for the performance in position resolution using the relation

$$\sigma_{x,y} \approx \frac{0.1 R_{\text{eff}}}{\sqrt{0.1E}}$$

with R_{eff} the effective Moliere radius and E the energy of the beam particle. This parametric relation has been found comparing different calorimeters as described in [13]. For a 20 GeV electron, assuming $R_{\text{eff}} = 20\,\text{mm}$ [7], the resolution should be $\sigma_{x,y} \approx 1.4\,\text{mm}$ while for a 30 GeV electron the prediction is $\sigma_{x,y} \approx 1.1\,\text{mm}$. The measured resolutions are $\sigma_{x,y} \approx 1\,\text{mm}$ and $\sigma_{x,y} \approx 0.9\,\text{mm}$ respectively. Considering that the tracking might contribute to these results, the ECAL perform better than the typical calorimeter. In order to subtract the tracking contribution a more detailed simulation is needed. In particular the Monte Carlo should include all material in the beam line in order to simulate the correct multiple Coulomb scattering. For the high energy run any improvement can be achieved only by reducing the intrinsic chamber contribution; placing a chamber directly in front of the calorimeter would give the impact position of the particle with an error smaller than 0.2 mm. This solution was suggested during the commissioning of the 2007 beam line, but could not be implemented for safety reasons (the movable platform on which the calorimeters were placed needed free space in order to rotate and the chambers could not be moved any closer).

The angular resolution is not described by a parametric formula but a comparison can be made with other calorimeters. The ALEPH electromagnetic calorimeter was build with lead, which has a radiation length almost double that of tungsten, making the calorimeter almost double in length. Since the angular resolution improves with the distance between first and last layers, i.e. a longer leverage allows higher angular precision, it is not surprising that the ALEPH calorimeter had a better angular resolution of about 1 mrad for a 10 GeV electron [14]. The ATLAS electromagnetic barrel calorimeter [15], which has lead as passive material, can reach a slightly better angular resolution than the CALICE calorimeter for the same reason; for electrons above 40 GeV an angular resolution of 7 mrad can be achieved while the CALICE prototype has a angular resolution of about 20 mrad.

Chapter 3

The Higgs self-coupling at the ILC

The Standard Model (SM) is the theory that best describes the experimental results of recent decades in particle physics. Combining the electroweak theory proposed by Glashow, Salam and Weinberg [16] and Quantum Chromodynamics (QCD) [17], the SM provides the most accurate description of the interaction of elementary particles we currently have. In this chapter the Higgs sector of the SM will be described focusing on the reasons to introduce this particle and its properties. Special attention will be given to the Higgs self-coupling which is the topic of the study of Chapter 5.

In the second part of the chapter the detector used in the simulation is described. Since the detector design is still to be optimised, the main focus of the description will be on the requirements for a detector at ILC .

A review of previous analyses performed on the Higgs self-coupling using fast simulation is presented in the last section of the chapter.

3.1 Standard Model Higgs

A complete description of the Standard Model can be found in many textbooks (e.g. [18, 19, 20]), while the latest review [21] was used as a reference in writing this section.

3.1.1 The Standard Model without the Higgs

The Standard Model theory, before introducing the Higgs boson, has two kinds of fields: matter fields and gauge fields. The former are the three generations of left-handed and right-handed quarks and leptons, which are spin-$\frac{1}{2}$ fermions. The left-handed fermions form weak isodoublets while the right-handed ones are weak isosinglets.

$$
\begin{aligned}
L_1 &= \begin{pmatrix} \nu_e \\ e^- \end{pmatrix}_L, \quad e_{R_1} = e_R^-, \quad Q_1 = \begin{pmatrix} u \\ d \end{pmatrix}_L, \quad u_{R_1} = u_R^-, \quad d_{R_1} = d_R^- \\
L_2 &= \begin{pmatrix} \nu_\mu \\ \mu^- \end{pmatrix}_L, \quad \mu_{R_2} = \mu_R^-, \quad Q_2 = \begin{pmatrix} c \\ s \end{pmatrix}_L, \quad u_{R_2} = c_R^-, \quad d_{R_2} = s_R^- \\
L_3 &= \begin{pmatrix} \nu_\tau \\ \tau^- \end{pmatrix}_L, \quad \tau_{R_3} = \tau_R^-, \quad Q_3 = \begin{pmatrix} t \\ b \end{pmatrix}_L, \quad u_{R_3} = t_R^-, \quad d_{R_3} = b_R^-
\end{aligned}
$$

The gauge fields correspond to the spin-one bosons that mediate the interactions. There are four gauge bosons in the electroweak sector, B_μ and $W_\mu^{1,2,3}$, while the strong sector has an octet of fields, $G_\mu^{1,\ldots,8}$. The fields strengths are given by

$$
\begin{aligned}
G^a_{\mu\nu} &= \partial_\mu G^a_\nu - \partial_v G^a_\mu + g_s f^{abc} G^b_\mu G^c_\nu \\
W^a_{\mu\nu} &= \partial_\mu W^a_\nu - \partial_v W^a_\mu + g_2 \varepsilon^{abc} W^b_\mu W^c_\nu \\
B_{\mu\nu} &= \partial_\mu B_\nu - \partial_v G_\mu
\end{aligned}
$$

where g_s, g_2 and g_1 are the coupling constants while f^{abc} and ε^{abc} are, respectively, the tensors of the structure constants of SU(3) and the antisymmetric tensor. The fermions are coupled to the gauge fields through the covariant derivative D_μ.

The SM Lagrangian is given by:

$$
\begin{aligned}
L_{SM} &= -\tfrac{1}{4} G^a_{\mu\nu} G^{\mu\nu}_a - \tfrac{1}{4} W^a_{\mu\nu} W^{\mu\nu}_a - \tfrac{1}{4} B_{\mu\nu} B^{\mu\nu} + \bar{L}_i i D_\mu \gamma^\mu L_i \\
&+ \bar{e}_i i D_\mu \gamma^\mu e_i + \bar{Q}_i i D_\mu \gamma^\mu Q_i + \bar{u}_{Ri} i D_\mu \gamma^\mu u_{Ri} + \bar{d}_{Ri} i D_\mu \gamma^\mu d_{Ri}.
\end{aligned}
$$

The Lagrangian is invariant under local $\mathrm{SU(3)_C} \times \mathrm{SU(2)_L} \times \mathrm{SU(1)_Y}$ gauge trans-

formations. It is impossible to add a mass term in the electroweak sector without breaking the symmetry. A mass term for the gauge boson, $\frac{1}{2}M_V^2 W_\mu W^\mu$, violates local $\mathrm{SU(2)_L} \times \mathrm{SU(1)_Y}$ gauge invariance while a mass term for the fermions mixes the left and right components of the fermion fields; this is not allowed since the term would not be invariant under isospin transformations.

Since the masses of the fermions and the weak bosons have been measured, the theory described so far requires an extension that can generate the masses of these particles while preserving the gauge symmetry. The spontaneous symmetry breaking mechanism proposed by Higgs et al. [22] provides such an extension to complete the SM.

3.1.2 The Higgs mechanism

To induce spontaneous symmetry breaking, a new scalar field must be added to the SM Lagrangian. The interaction of this field with the boson fields must produce three massive bosons. In order to have three bosons, the simplest choice is a complex SU(2) doublet of scalar fields

$$\Phi = \begin{pmatrix} \phi^+ \\ \phi^0 \end{pmatrix}.$$

This introduces a new term in to the SM Lagrangian discussed in the previous section given by

$$L_H = \left(D^\mu \Phi\right)^\dagger \left(D_\mu \Phi\right) - \mu^2 \Phi^\dagger \Phi - \lambda \left(\Phi^\dagger \Phi\right)^2.$$

For $\mu^2 < 0$ the neutral component of the doublet Φ develops a vacuum expectation value

$$\langle \Phi \rangle \equiv \langle 0|\Phi|0\rangle = \begin{pmatrix} 0 \\ \frac{v}{\sqrt{2}} \end{pmatrix} \text{ with } v = \left(-\frac{\mu^2}{\lambda}\right)^{1/2}.$$

Writing the field in terms of four fields $\theta_{1,2,3}(x)$ and $H(x)$, to first order,

$$\Phi(x) = \begin{pmatrix} \theta_2 + i\theta_1 \\ \frac{1}{2}(v+H) - i\theta_3 \end{pmatrix} = e^{i\theta_a(x)\tau^a(x)/v} \begin{pmatrix} 0 \\ \frac{1}{\sqrt{2}}(v+H) \end{pmatrix},$$

making a gauge transformation on this field to move to the unitary gauge

$$\Phi(x) \to e^{i\theta_a(x)\tau^a(x)}\Phi(x) = \frac{1}{\sqrt{2}} \begin{pmatrix} 0 \\ v+H \end{pmatrix},$$

fully expanding the term $|D_\mu|^2$ of the Lagrangian L_{SM}

$$\begin{aligned} |D_\mu|^2 &= \left|\left(\partial_\mu - ig_2\tfrac{\tau_a}{2}W_\mu^a - ig_1\tfrac{1}{2}B_\mu\right)\Phi\right|^2 \\ &= \frac{1}{2}\left| \begin{pmatrix} \partial_\mu - \frac{i}{2}\left(g_2W_\mu^3 + g_1B_\mu\right) & -\frac{ig_2}{2}\left(W_\mu^1 - iW_\mu^2\right) \\ -\frac{ig_2}{2}\left(W_\mu^1 + iW_\mu^2\right) & \partial_\mu + \frac{i}{2}\left(g_2W_\mu^3 - g_1B_\mu\right) \end{pmatrix} \begin{pmatrix} 0 \\ v+H \end{pmatrix} \right|^2 \\ &= \frac{1}{2}(\partial_\mu H)^2 + \frac{1}{8}g_2^2(v+H)^2\left|W_\mu^1 + iW_\mu^2\right|^2 + \frac{1}{8}(v+H)^2\left|g_2W_\mu^3 - g_1B_\mu\right|^2, \end{aligned}$$

then defining the new fields $W_\mu^\pm$, Z_μ and A_μ as

$$W^\pm = \frac{1}{\sqrt{2}}\left(W_\mu^1 \mp iW_\mu^2\right), \quad Z_\mu = \frac{g_2W_\mu^3 - g_1B_\mu}{\sqrt{g_2^2+g_1^2}}, \quad A_\mu = \frac{g_2W_\mu^3 + g_1B_\mu}{\sqrt{g_2^2+g_1^2}},$$

and picking up the terms which are bilinear in the fields $W_\mu^\pm$, Z_μ and A_μ

$$M_W^2W_\mu^+W^{-\mu} + \frac{1}{2}M_Z^2Z_\mu Z^\mu + \frac{1}{2}M_A^2A_\mu A^\mu,$$

the W and Z bosons have acquired masses while the photon is massless

$$M_W = \frac{1}{2}vg_2,\ M_Z = \frac{1}{2}\sqrt{g_2^2+g_1^2},\ M_\gamma = 0.$$

In order to have a gauge invariant theory that describes the experimental observations, spontaneous symmetry breaking must provide a mechanism to generate the mass of the fermions. Using the same mechanism described for the boson, it is possible to generate a mass term for all generations of fermions using the Lagrangian

$$L_F = -\lambda_e \bar{L}\Phi e_R - \lambda_d \bar{Q}\Phi d_R - \lambda_u \bar{Q}\Phi u_R + h.c. \tag{3.1}$$

In the case of the electrons

$$\begin{aligned} L_F &= \tfrac{1}{\sqrt{2}}\lambda_e \left(\overline{\nu}_e, \overline{e}_L\right) \begin{pmatrix} 0 \\ v+H \end{pmatrix} e_R \\ &= \tfrac{1}{\sqrt{2}}\lambda_e \left(v+H\right) \overline{e}_L e_R. \end{aligned}$$

The constant term in front of the fermion terms $\overline{f}_L f_R$ represents the fermion mass, for example

$$m_e = \frac{\lambda_e v}{\sqrt{2}}.$$

The spontaneous symmetry breaking mechanism can induce the appearance of mass terms for both fermions and bosons in the SM Lagrangian while preserving $\mathrm{SU(3)_C} \times \mathrm{SU(2)_L} \times \mathrm{SU(1)_Y}$ invariance. The $\mathrm{U(1)_Q}$ and the $\mathrm{SU(3)_C}$ symmetries remain unbroken.

3.1.3 The Higgs boson

The scalar potential introduced to generate the masses of the SM particles is also responsible for the generation of a new particle, the Higgs boson. The scalar potential $V\left(\Phi\right) = \mu^2 \Phi^\dagger \Phi + \lambda \left(\Phi^\dagger \Phi\right)^2$ can be expanded as

$$V = \frac{\mu^2}{2}\left(0, v+H\right) \begin{pmatrix} 0 \\ v+H \end{pmatrix} + \frac{\lambda}{4} \left| \left(0, v+H\right) \begin{pmatrix} 0 \\ v+H \end{pmatrix} \right|^2,$$

and using $v^2 = -\mu^2/\lambda$

$$V = -\frac{1}{2}\lambda v^2 \left(v+H\right)^2 + \frac{1}{4}\lambda \left(v+H\right)^4.$$

The Lagrangian for the Higgs is given by

$$\begin{aligned} L_H &= \tfrac{1}{2}\left(\partial_\mu H\right)\left(\partial^\mu H\right) - V \\ &= \tfrac{1}{2}\left(\partial^\mu H\right)^2 - \lambda v^2 H^2 - \lambda v H^3 - \tfrac{\lambda}{4} H^4. \end{aligned} \tag{3.2}$$

The mass of the Higgs is therefore

$$M_H^2 = 2\lambda v^2 = -2\mu^2,$$

and the self-interacting vertexes are

$$g_{H^3} = (3!)\, i\lambda v = 3i\frac{M_H^2}{v}, \quad g_{H^4} = (4!)\, i\frac{\lambda}{4} = 3i\frac{M_H^2}{v^2}.$$

From the Lagrangian of Equation (3.1) it is possible to obtain the coupling of the Higgs to the bosons and fermions

$$g_{Hff} = i\frac{m_f}{v}, \quad g_{HVV} = -2i\frac{M_V^2}{v}, \quad g_{HHVV} = -2i\frac{M_V^2}{v^2}.$$

These couplings determine the decay modes of the Higgs. Since the couplings are proportional to the mass of the coupled particles, the favoured decays are those in which the Higgs decays into the fermions with the highest mass or bosons with the lowest mass (due to the negative sign in the coupling). A complete description for each decay mode can be found in the second chapter of [21]. The branching ratios of the SM Higgs boson decay as a function of the Higgs mass are shown in Figure 3.1.

3.1.4 Experimental and theoretical limits on the Higgs mass

The hunt for the Higgs boson is still ongoing at the Tevatron and will probably be completed at LHC. While previous experiments have set a lower limit on the Higgs mass, the theory sets upper limits that will be reached at the LHC as briefly discussed in this section.

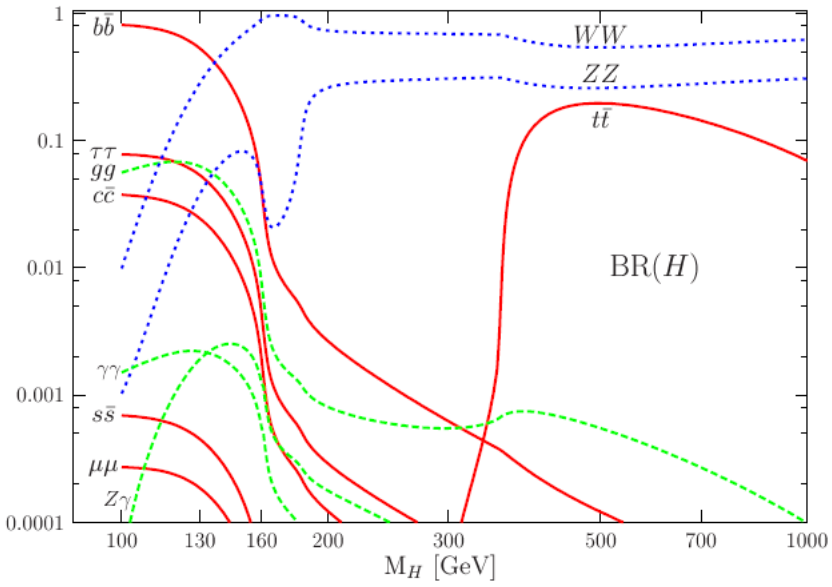

Figure 3.1: The SM Higgs decay branching ratios as a function of the Higgs mass (from [21]).

3.1.4.1 Experimental limits

The strongest experimental limit has been set by the LEP2 experiments using the process $e^+e^- \rightarrow Z^* \rightarrow ZH$. Combining the results from all experiments no excess was found above the expected SM background and the limit $M_H > 114.4\,\text{GeV}$ was determined at 95% confidence level (CL) [23].

The mass of the Higgs can also be constrained using high precision measurements of several SM observables such as the W mass, the top mass and the effective weak mixing angle. Using the latest values available [24], the mass of the Higgs boson is predicted to be $M_H = 87^{+36}_{-27}\,\text{GeV}$, leading to 95% CL upper limit of $M_H < 160\,\text{GeV}$.

The combination of direct searches and constraints from the SM fit is shown in Figure 3.2. The yellow region is excluded by the LEP searches while the blue band includes theory uncertainties.

3.1.4.2 Theoretical constraints

In addition to the limits on the Higgs mass derived from experimental results, it is possible to set some limits by requiring the SM to be a perturbative and unitary theory. For example, requiring WW scattering to be unitary [25], leads to the limit

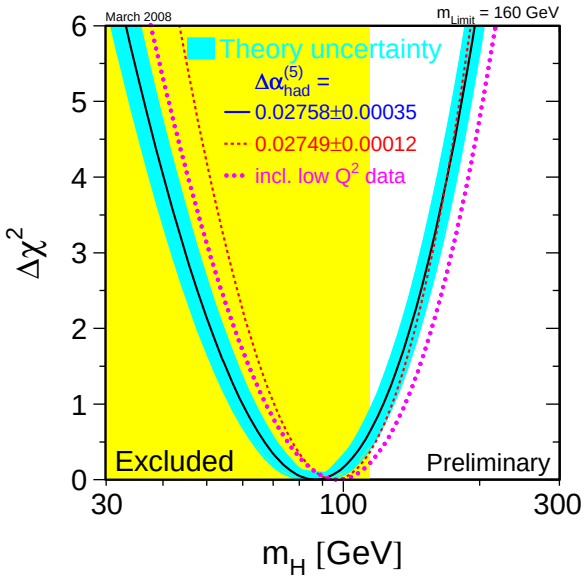

Figure 3.2: χ^2 of the SM parameters as a function of the Higgs mass (lines); the predicted mass is 87^{+36}_{-27} GeV. The yellow region is excluded by direct searches at LEP; the Higgs mass is therefore expected to be in the region $114\,\text{GeV} < M_H < 160\,\text{GeV}$ with 95% CL (from [24]).

$$M_H \lesssim 710\,\text{GeV}.$$

A similar constraint can be set by requiring processes involving the Higgs to be perturbative: for a Higgs mass above 1 TeV the theory is not perturbative because the loop terms with the Higgs self-coupling are as large as the leading order term. Moreover, a Higgs above 1 TeV has a total width comparable with the mass and the Higgs cannot be considered a resonance anymore.

Two more constraints can be set which depend on the energy at which the theory is no longer perturbative and hence new physics should appear. The first limit, an upper bound on the mass, can be set by requiring the theory to be non trivial (e.g. the coupling is different from zero). The second limit arises from requiring the vacuum to be stable; in this case a lower limit can be set on the Higgs mass. Figure 3.3 shows the two bounds as a function of the cut-off energy where the new physics should appear.

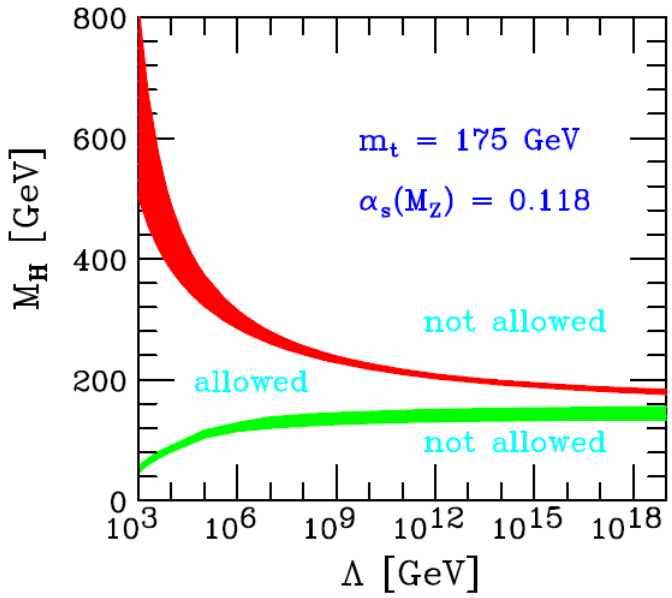

Figure 3.3: Triviality (upper) and vacuum stability (lower) bounds as a function of the new physics or cut-off energy (from [21]).

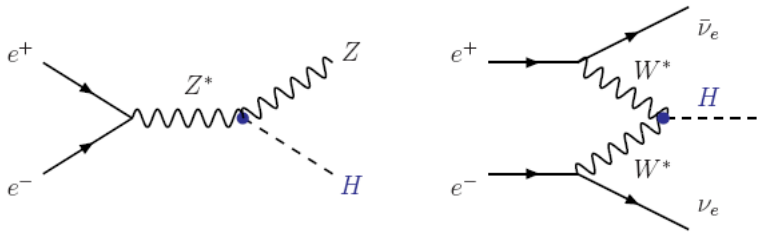

Figure 3.4: Feynman diagrams for Higgs production at LC. On the left the Higgsstrahlung process, on the right the WW fusion process.

3.1.5 Higgs production at the LC

Having described the role of the Higgs in the SM, the theoretical and experimental limits on its mass and the different decay channels depending on the mass, there is only one step left: how to produce the Higgs boson at a Linear Collider.

In e^+e^- collisions at a centre of mass energy above that of LEP2, there are two main production channels: Higgsstrahlung and WW fusion (Figure 3.4). There are other mechanisms that can lead to the production of the Higgs boson but these have a smaller cross section and are not relevant for the current discussion.

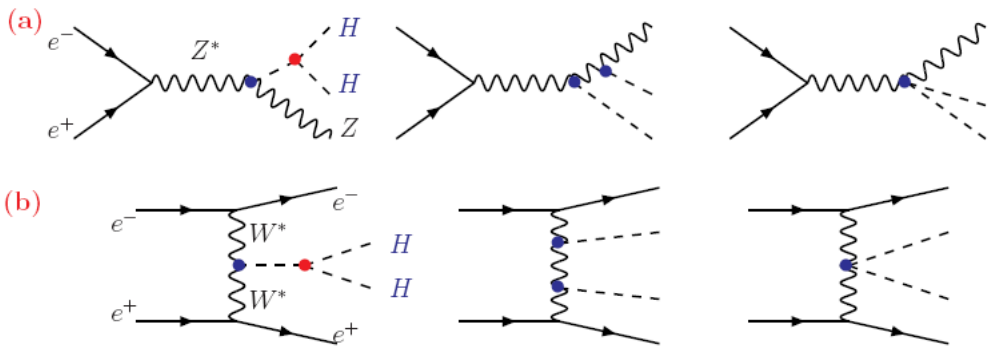

Figure 3.5: Diagrams for double Higgs production: row (a) double Higgsstrahlung, row (b) the vector boson fusion. Only first diagram in each row includes the Higgs trilinear coupling (red dot).

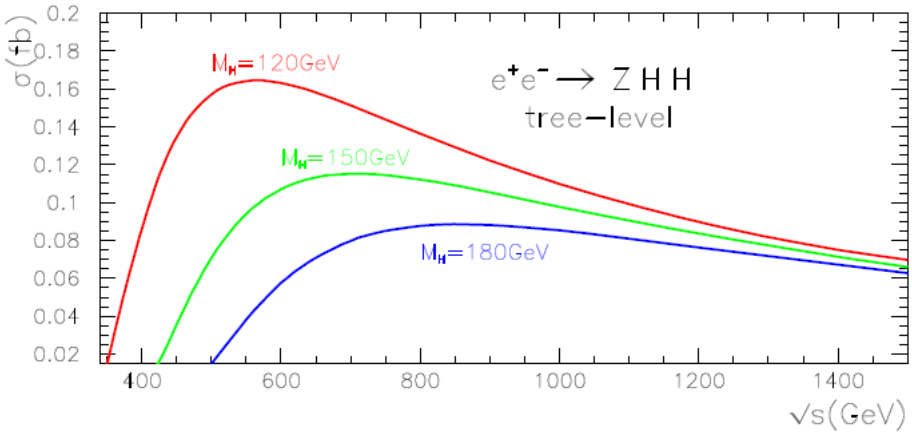

Figure 3.6: ZHH cross section as a function of the centre of mass energy for three Higgs masses (from [26]).

3.1.6 Determining the Higgs self-coupling

Observing two (or more) Higgs bosons in an event is the only way of measuring the self-coupling of the Higgs.

Higgs pairs can be produced through double Higgsstrahlung $e^+e^- \rightarrow Z^* \rightarrow ZHH$ or vector boson fusion $e^+e^- \rightarrow \nu\nu\,(V^*V^*) \rightarrow \nu\nu HH$. The Feynman diagrams for these two processes are shown in Figure 3.5. The first diagram in each row is the only one which involves the triple Higgs interaction, the other diagrams are generated by other SM process and are irreducible backgrounds for the self-coupling measurement. The cross section of the ZHH channel has been calculated for different Higgs masses by two groups [26, 27] with similar results as summarised in Figure 3.6.

In order to complete the SM Higgs potential defined by equation 3.2, it is required to measure the quadrilinear coupling λ_{HHHH} which would require the production of three Higgs bosons. However the cross section for this process is so small (less than 1 ab) that none of LHC, its upgrade the SLHC or the LC can measure this coupling.

3.1.6.1 Parameters in the analysis

In the analysis presented in Chapter 5 the Higgs mass was set to 120 GeV and the centre of mass energy was 500 GeV. The low mass was chosen because the fit to the SM parameters prefers a low mass Higgs. The centre of mass energy was the present preferred design energy for the ILC and conveniently is close to the maximum of the cross section (Figure 3.6). The events were simulated using one of the possible beam polarisations for the first phase of ILC, -80% for electrons and 0% for positrons, as described in [1].

With this polarisation, the total cross section for the process is 0.18 fb, however there are many different final states and this complicates the analysis. Since the Z decays mainly into quarks (70%) and a 120 GeV Higgs decays into $b\bar{b}$ 71% of the time, the main channel is the six-quark final state qqbbbb with a branching ratio (BR) of 34%. Other important decay channels are Z decays into neutrinos (20%) leading to the final state $\nu\nu$qqqq and the decay of one of the Higgs into WW (13%) leading to the final state qqbbWW. Both channels have a BR of about 10%. Unfortunately, the clean leptonic channels have a very small cross section due to the small BR for Z to charged leptons (3% each); the final states llbbbb are about 5% in total. Table 3.1 summarises the main decay channels of the ZHH with relative cross sections and expected number of events for an integrated luminosity of $500\,\text{fb}^{-1}$.

3.1.6.2 From cross section to self-coupling

The analysis presented in Chapter 5 allows the measurement of the ZHH cross section. In order to evaluate the Higgs self-coupling, the effect of the irreducible backgrounds (due to the diagrams without the red vertex in Figure 3.5) must be taken in account.

ZHH→	σ(fb)	Events for 500 fb^{-1}
total	0.183	91.5
qqbbbb	0.064	31.9
qqbbWW	0.024	12.1
$\nu\nu$bbbb	0.018	9.2
qqbb$\tau\tau$	0.014	6.8
llbbbb (each)	0.003	1.5

Table 3.1: Cross section for different decay modes of ZHH and expected number of events for an integrated luminosity of 500 fb^{-1}.

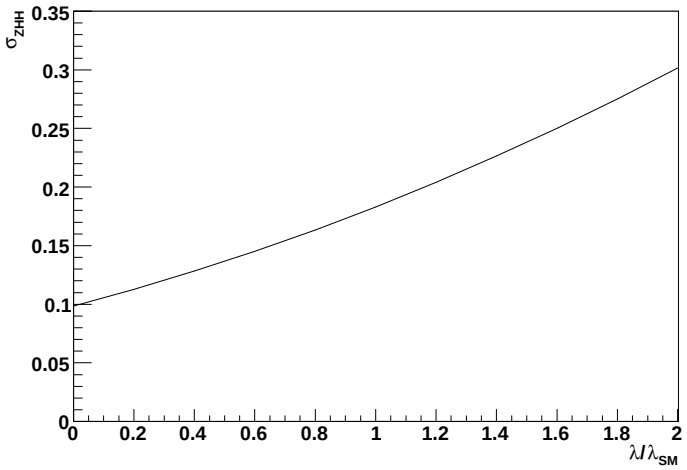

Figure 3.7: Correlation between the ZHH cross section and the Higgs self-coupling. The latter is expressed in units of the SM self-coupling.

The correlation between the cross section and the Higgs self-coupling is shown in Figure 3.7. The plot was obtained with the WHIZARD [28, 29, 30] event generator for the specific beam parameters of this analysis; the generator can reproduce the results presented in [31]. Given the non-linear dependence of the cross section on the self-coupling, in this thesis the focus will be on the cross section when comparing results with the literature.

Measuring a value of the Higgs self-coupling different from zero is the main goal of an analysis on the ZHH channel. Such a result would prove the existence of the HHH vertex which has not been discovered yet. This channel is also sensitive to beyond Standard Model effects but this study is beyond the scope of this thesis which focuses on the discovery of this process.

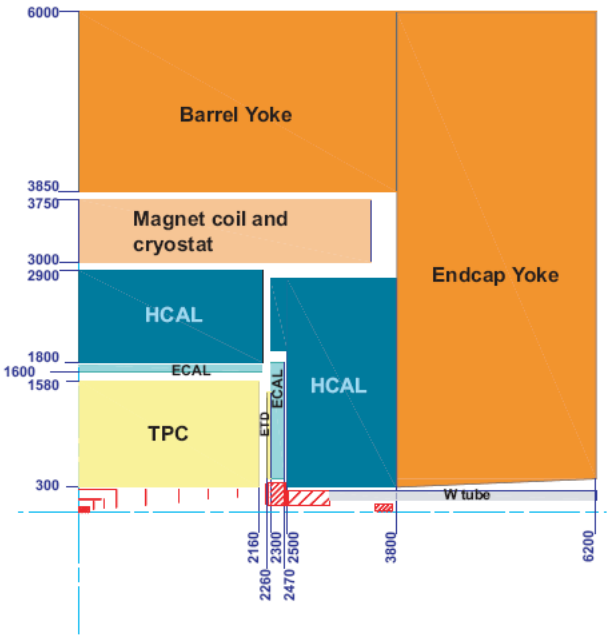

Figure 3.8: Quarter view of the LDC detector concept (from [2]).

3.2 Detector description and requirements

In this section the European detector concept known as the Large Detector Concept (LDC) is presented. The design of this and other LC detectors is far from final, therefore each sub-detector is discussed below focusing more on the physics requirement than the actual design or technology used. Most of the material used in this section is taken from the Reference Design Report for the International Linear Collider [2, 32].

3.2.1 Detector overview

The LDC detector is designed around the particle flow concept and has the typical structure of a general purpose particle physics detector as presented in Figure 3.8 and 3.9. The vertex detector is the closest element to the interaction point and provides high resolution track reconstruction which allows excellent b and c tagging. The central volume of the detector is occupied by the Time Projection Chamber (TPC), which provides up to 200 precise measurements along the x-y plane with each point reconstructed in 3D space. The tracking system is supported by other elements to increase the tracking performance at very small angles. The calorimetry is composed

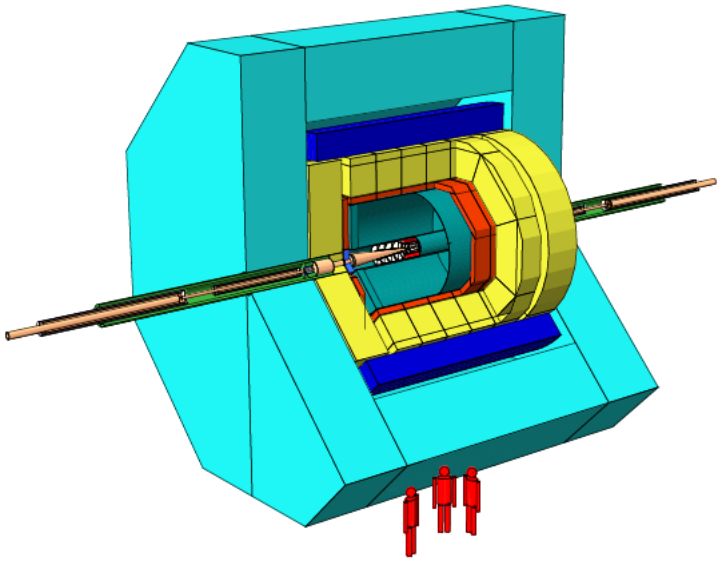

Figure 3.9: View of the LDC detector concept, as simulated with the MOKKA simulation package (from [2]).

of highly segmented electromagnetic and hadronic calorimeters. The magnetic field of the LDC detector is 4 T, generated by a coil placed outside the calorimeters. This solution was chosen in order to reduce the amount of passive material in front of the calorimeters thus improving the jet energy resolution. The return path of the magnetic flux is instrumented with muon chambers which can also measure the hadronic shower tail to further improve the jet energy resolution.

3.2.2 Calorimetry

Excellent jet energy resolution is probably the most important requirement for a LC detector, being linked with the measurement of W, Z and Higgs bosons and the top quark. The most important detector involved in the jet energy measurement is the calorimeter system described in detail in Chapter 4. Several studies have addressed the importance of this measurement in different analyses and are described in [2].

The Higgs mass can be measured with high precision in $e^+e^- \rightarrow ZH$ events using the recoil mass in the leptonic decay of the Z (Section 3.2.3); also the four-jet channel ($Z \rightarrow q\bar{q}$ and $H \rightarrow b\bar{b}$) can be used to reach a similar precision in M_H because of the higher statistics due to the larger branching ratio of the Z decay to quarks. All

the top channels require a high performance in the jet energy measurement, since at least two jets are produced in each event (the BR($t \rightarrow bW$) is 99.9%). The same argument concerning statistics made for the ZH channel is valid for the top because of the high BR of the W to quarks. Another interesting channel strongly affected by the jet energy measurement is WW scattering. The importance of this channel is linked with the perturbativity of the SM; in fact the cross section for this process diverges at 1 TeV if the Higgs does not exist. In any case this is an important test of the SM and one of the key measurements at the LC. A good jet energy resolution allows a better separation of the WW pair from the ZZ background as shown in Figure 4.1. Finally, the calorimetry is a key component in the ZHH analysis and a description of previous analyses on this channel is given in Section 3.3.

The LDC detector proposes the use of two sampling calorimeters with high granularity. The electromagnetic calorimeter is essentially the same detector tested by the CALICE collaboration and described in Section 2.2 with a small difference in the longitudinal segmentation. Tungsten is used as the passive material while silicon wafers are used for the sensitive material. Since this sub-detector is the most expensive part of the whole detector, several models with a reduced number of silicon layers have been proposed. For the LDC00Sc detector model used in this thesis the number of layers is set to 40. These layers are divided into two sections, 30 thin layers followed by 10 thicker layers at the back of the calorimeter. For the hadronic calorimeter two options have been considered: scintillator tiles with analogue readout or Resistive Plate Chambers (RPC) with digital readout. Both options use iron as passive material. LDC00Sc is the model with the scintillator tiles as active component, this choice being made mainly because the scintillator technology is the more mature. The CALICE hadron prototype tested at CERN is equipped with scintillator tiles while a digital prototype is currently being built.

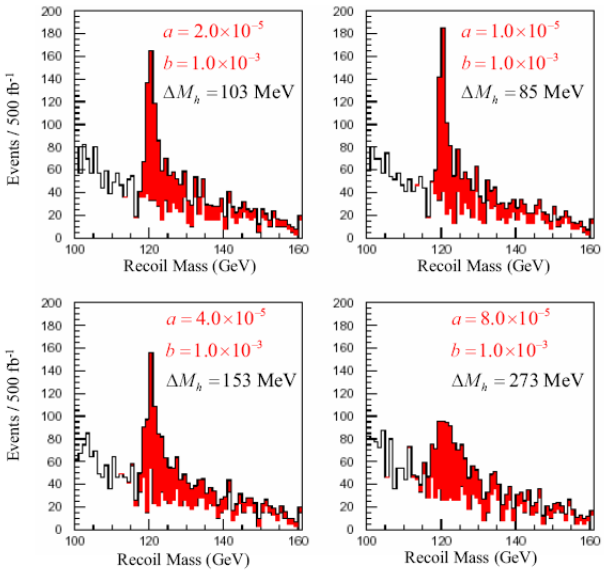

Figure 3.10: Effect of tracking performance on the Higgs mass in the ZH $\rightarrow \mu\mu$H channel. The parameter a and b are defined in the text. (From [2]).

3.2.3 Tracking

The tracking system of a Linear Collider detector must provide high performance, with high efficiency and low fake rate over the whole solid angle. This is a challenging requirement because in complex events such as $t\bar{t}$, more than fifty tracks can be produced with some events having up to one hundred tracks. The particle flow concept ideally requires that all tracks are reconstructed and no fake tracks are produced.

In addition to the particle flow requirements, the tracking system must satisfy requirements coming from physics analysis. In fact the best measurement of the mass and width of the Higgs boson will be obtained from the measurement of the recoil mass in ZH events when the Z decays into electrons and muons. Figure 3.10 shows the physics performance for different tracking performances; the resolution is defined as $\delta p_t/p_t^2 = a \oplus b/(p_t \sin\theta)$. The goal set in the RDR [2] is to build a tracking system with a resolution of $\delta p_t/p_t^2 = 5.0 \times 10^{-5}\text{GeV}^{-1}$.

The main volume of the tracking system for the LDC detector will be occupied by a Time Projection Chamber (TPC) supported by several disks and layers instrumented with silicon detectors to cover the forward region.

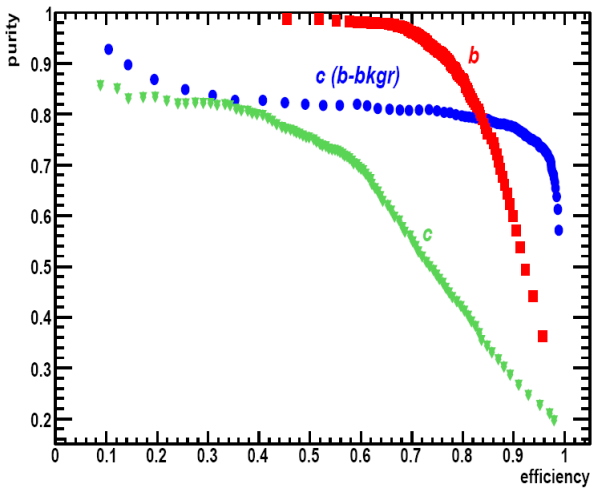

Figure 3.11: Vertexing performances for b tagging (red), c tagging (green) and c tagging in presence of b jets (blue) (from [2]).

3.2.4 Vertexing

The vertex detector has to provide both b and c tagging. The first of these is crucial since many relevant physics channels have b quarks in the final state: a low mass Higgs decays 70% of the time into $b\bar{b}$, top decays into a b and a W and about 12% of the time a Z decays into $b\bar{b}$. By requiring events to have a minimum number of b jets, it is possible to reduce many backgrounds; having an excellent b tagging improves all these analyses.

The possibility of performing c tagging further enhances the background reduction. In fact c quarks are the main cause of contamination for b tagging. Having this further level of tagging it should be possible to reduce the contamination and overall improve any physics analysis. Tagging c jets will also provide the possibility to measure the $H \rightarrow c\bar{c}$ decay from which it is possible to evaluate the coupling of the Higgs to the c quark.

The performance for the standard LDC vertex detector using the Linear Collider Flavour Identification (LCFI, [33]) reconstruction software is presented in Figure 3.11 for $Z \rightarrow q\bar{q}$. The purity is plotted as a function of efficiency for the b tagging (red), c tagging (green) and c tagging with only b background (blue). The performance of this detector is linked with the distance of the first detector layer from the beam. A

detector technology proposed for this detector is that of pixel sensors with a special support to minimise the amount of material between the layers in the vertex detector in order to keep the multiple scattering to a minimum.

3.2.5 Hermiticity

One of the most important features for the detector is the hermiticity. Covering the full solid angle from the interaction point allows the missing energy in each event to be determined. This is a key requirement for all SUSY analyses that need to measure the missing energy to estimate the masses of super-symmetric particles. Perfect hermiticity is a premium also for multi-jet final states. Reducing dead areas and extending the tracking and the calorimetry to very small angles with respect to the beam line are the detector challenges linked with the hermiticity. LDC has extended the tracking to small angles using silicon disks in the very forward region. The option of adding a silicon layer after the TPC disk is currently been considered to improve the forward tracking. The forward calorimeter is a crucial element in the detector since it is responsible for the measurement of the luminosity. All the elements in the very forward region are currently under development and have not been used in the detector model used in this analysis.

3.3 Studies performed on fast simulation

The analyses performed until now on the ZHH channel to evaluate the sensitivity to the Higgs self-coupling have used fast Monte Carlo simulations ([31, 34]). Both analyses stress the importance of achieving good jet energy resolution in order to separate the small signal from the backgrounds. Using a neural network analysis the analysis described in [31] achieved the better result, obtaining a sensitivity on the ZHH cross section of 10% and on the Higgs self-coupling of 18% for an integrated luminosity of $2000\,\mathrm{fb}^{-1}$. The result obtained in [34] is summarised in Figure 3.12.

3.3.1 Limitation of fast simulation

In the ZHH analyses with fast Monte Carlo simulation, the visible particles were assumed to be perfectly reconstructed and were used to form six jets. These jets were then smeared to simulate a given jet energy resolution. This approach suffers several limitations: all confusion due to clusters overlapping is neglected and, more importantly, particles with high penetration in the HCAL (leakage effect) are reconstructed perfectly while they will have a bad resolution due to the limited numbers of hits in the calorimeter. Another effect is caused by the assumption of perfect track reconstruction since, in a multi-jet environment, the probability of producing a fake track are low but not negligible. These fake tracks are a severe problem since energy is "created" that will affect the whole reconstruction.

In addition to these problems, both analyses lacked a fundamental component for a high multiplicity jet environment: gluon emission. Each quark has about 10% probability of emitting a gluon that leads to an extra jet of particles. Having removed the possibility of producing such extra jets, the events are simpler and a significant reduction in the confusion and the combinatorial problem is obtained. A study on the effect of gluon emission was presented for the first time at LCWS07 [34]; the result is summarised in Figure 3.12. There is a significant difference between the curves with and without gluon emission; for a jet energy resolution of $30\%/\sqrt{E}$ the sensitivity of the coupling measurement worsens from 32% to 54%. This is clearly an important effect that cannot be neglected in a realistic simulation.

The amount of data simulated in the fast Monte Carlo analysis is higher than the expected integrated luminosity for the first phase of the LC. For the current machine parameters the expected integrated luminosity is $500\,\mathrm{fb}^{-1}$. Reducing the total integrated luminosity from $2000\,\mathrm{fb}^{-1}$ to $500\,\mathrm{fb}^{-1}$ reduces the expected sensitivity by a factor two.

The two analyses had also some differences: while the analysis in [34] used only the six-jet final state, the one in [31] used the full BR of the Z. Moreover the two analyses performed a different vertex reconstruction; a realistic one in [34] and a

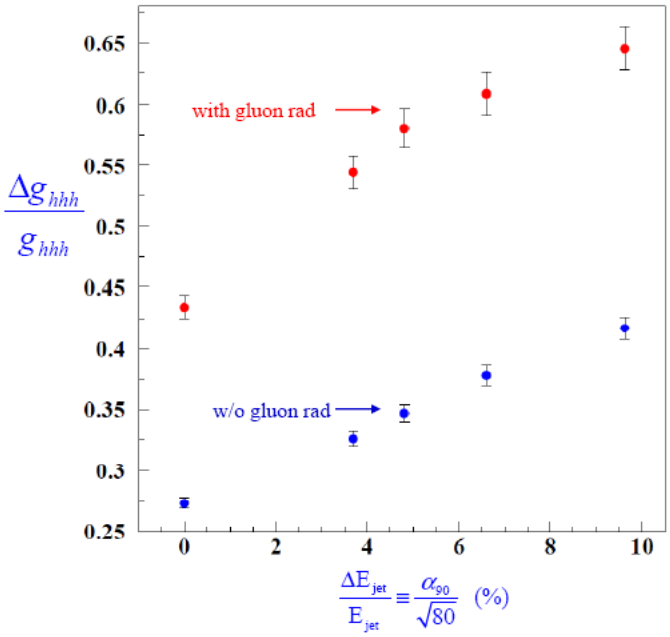

Figure 3.12: Resolution on Higgs self-coupling as function of the jet energy resolution without gluon emission (blue) and with gluon emission (red) (from [2]).

parametrisation in [31]. These two effects explain the difference in the results between the two analyses; assuming a jet energy resolution of $30\%/\sqrt{E}$, the resolution on the Higgs self-coupling obtained in [34] was 35%, about twice the 18% resolution obtained in [31]. A contribution to this difference due to the selection cannot be excluded.

3.3.2 LHC potential

In this start year of the Large Hadron Collider (LHC), it is important to understand the different capabilities of LHC and LC for the measurement of the Higgs self-coupling. The interplay between the two machines has been studied by the Durham LHC/ILC study group and is presented in [35]. At LHC, the main mechanism to produce a Higgs is gluon-gluon fusion. The Higgs self-coupling can be estimated from events in which the Higgs decays into two Higgs bosons as shown in Figure 3.13.

For a low mass Higgs (less than 140 GeV) the LHC detectors should not be able to detect any signal. In fact for these masses the Higgs decays mainly to $b\bar{b}$ for a final state with four b jets and this is overwhelmed by the jet background typical of hadronic machines. The best strategy is to look for the $bb\gamma\gamma$ final state and in this

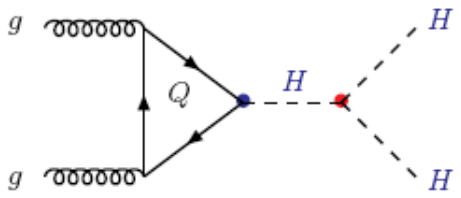

Figure 3.13: Main production mechanism including Higgs self-coupling at the LHC.

case the upgrade of LHC, the SLHC, with an integrated luminosity of 6 ab^{-1}, should be able to determine a self-coupling different from zero at 95% confidence level (CL). If the results of the fast simulation are confirmed, the Linear Collider will have a much better resolution on the Higgs self-coupling, of the order of 50% or even better if more decay modes can be exploited or more data collected.

The situation is reversed if the Higgs has a mass larger than 140 GeV. In this case the Higgs decays mainly to WW pairs that are easier to isolate in a hadronic environment. The loss in cross section due to the higher Higgs mass is more than compensated by the use of this channel with a possible resolution at SLHC of 30% on the self-coupling. For the LC the cross section of the ZHH decreases rapidly with the Higgs mass hence reducing the reachable resolution; it is likely to be impossible to estimate the self-coupling with a realistic amount of data (1 ab^{-1}). However increasing the centre of mass energy together with using polarised beams will allow the use of Higgs production through WW fusion. There are no detailed studies for this case at the ILC.

Chapter 4

Particle flow algorithms

The particle flow concept is one of the ideas driving the design of the detector for a high energy linear collider. In this chapter the motivations for such concept are presented. The available particle flow algorithms (PFAs) are described in the second section and a comparison between them is presented in the last section. The work presented in this chapter has been published as an LC note [37].

4.1 Jet energy requirement

A large part of ILC physics involves particles decaying into quarks that, after hadronisation, become jets. One goal of the ILC detector is to reach a mass resolution better than the natural width of the W and Z bosons (about 2 GeV). Achieving this resolution allows good separation of different channels, therefore reducing the statistics needed for a discovery or enhancing an exclusion limit. In order to reconstruct the bosons mass with high precision, the energy and the momentum resolution of the jets must be very good. An example of the improvement that a good energy resolution allows, is the WW and ZZ mass separation presented in Figure 4.1 [38]. The plot on the left has $60\%/\sqrt{E}$ energy resolution while that on the right has $30\%/\sqrt{E}$. The former is the performance of a LEP-like detector while $30\%/\sqrt{E}$ is related to the natural width of the W and Z boson as explained below.

The mass of a boson decaying into two jets is given by

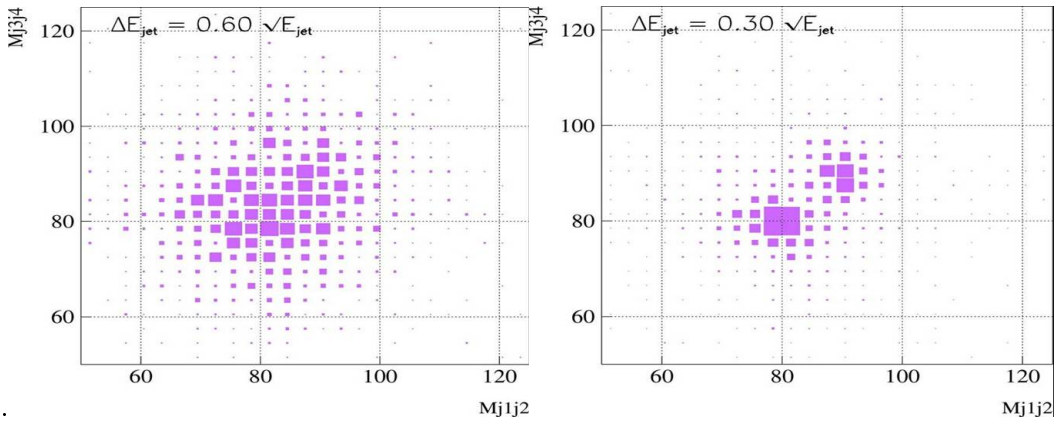

Figure 4.1: WW/ZZ invariant mass separation plot with jet energy resolution of $60\%/\sqrt{E}$ (left) or $30\%/\sqrt{E}$ (right) (from [38]).

$$m^2 = m_{j1}^2 + m_{j2}^2 + 2E_{j1}E_{j2}(1 - \cos\theta_{12}). \tag{4.1}$$

Assuming perfect reconstruction of the jets' direction and neglecting the invariant mass of the jets, the boson mass depends only on the jet energies. The first assumption was proved by a dedicated study [56]. The invariant mass of a jet can be approximated to zero because it is at most 5 GeV for b jets, much smaller in general than the jet energy.

Considering the simple case of a Z boson decaying at rest, $cos\theta_{12} = -1$ and $E_{j1} = E_{j2}$. Therefore

$$m_Z^2 = 4E_j^2 \tag{4.2}$$

so that

$$\frac{\sigma_m}{m} = 2\frac{\sigma_{E_j}}{E_j}. \tag{4.3}$$

Requiring that the mass resolution is comparable with the natural width,

$$\frac{\sigma_m}{m} \approx \frac{\Gamma_m}{m}, \tag{4.4}$$

then

Jet energy (GeV)	Jet energy resolution
45	$< 26\%$
100	$< 38\%$
180	$< 51\%$
250	$< 60\%$

Table 4.1: Jet energy resolution requirement for an ILC detector.

$$\begin{array}{l} \frac{\Gamma_W}{m_W} = \frac{2.124}{80.425} = 0.026 \\ \frac{\Gamma_Z}{m_Z} = \frac{2.495}{91.188} = 0.027. \end{array} \quad (4.5)$$

The experimental jet energy resolution is proportional to $1/\sqrt{E}$, hence it is convenient to use the same dependence:

$$\frac{\sigma_{E_j}}{E} = \frac{\alpha(E_j)}{\sqrt{E_j}}. \quad (4.6)$$

Then the following relation must be fulfilled:

$$\frac{\alpha(E_j)}{\sqrt{E_j}} < 2 \times 0.027 \Rightarrow \alpha(E_j) < 0.054\sqrt{E_j}. \quad (4.7)$$

Since the jet energy resolution depends on the jet energy, slightly worse resolution for high energy jets is acceptable as shown in Table 4.1.

The jet energy resolution can be approximately separated in three components corresponding to charged particles, photons and neutral hadrons in the jet. The contribution to the total energy resolution from these is about 65%, 25% and 10% respectively. These values arise from the average composition of a jet, which is made of about 75% of pions, one third of which are neutral and decay to photons, 15% of other charged particles and 10% of neutral hadrons, mainly K_L. Each component contributes to the jet energy resolution with a different weight that depends on the resolution of the detector that measures it. In summary:

$$\sigma_{Jet} = \sigma_{Tracking} \oplus \sigma_{ECal} \oplus \sigma_{HCal} \quad (4.8)$$

Charged particles are reconstructed by the tracking system with a momentum resolution of $\delta p_t/p_t^2 = 5.0 \times 10^{-5}\text{GeV}^{-1}$ (see Section 3.2.3). The energy of neutral particles is measured by the calorimeters. A typical value for the resolution for photons measured by the electromagnetic calorimeter is $\sim 15\%/\sqrt{E}$ while neutral hadrons are typically reconstructed with a resolution of $\sim 60\%/\sqrt{E}$. Since the tracking system resolution is much better than the typical calorimeter resolution, in order to achieve the required precision, the main focus in the design of any LC detector is to improve the calorimetric performance.

4.2 Particle flow concept

Two different concepts have been proposed to achieve the required jet energy resolution: the particle flow concept [39] and the dual read out concept [40, 41, 42]. The former is the evolution of the energy flow concept used at LEP [43] and proposes to use sampling calorimeters. The latter concept proposes to measure all the components of a hadronic shower using scintillator and Ĉerenkov light in a crystal calorimeter. It is not discussed further here; more information can be found in the literature.

The goal of the particle flow concept is to reconstruct all particles in an event. In order to take into account errors in the reconstruction of the particles in a jet, a fourth contribution to the jet energy resolution, in addition to the three described in the previous section, has to be considered. This is called the "confusion term" and arises from mis-reconstruction of tracks, mis-association of calorimeter hits to clusters or mis-association of clusters to tracks. These errors in the reconstruction can be caused by physical factors, i.e. the cell size of the calorimeter, or by a limit in the reconstruction algorithms. For this reason, more than one PFA must be used in order to separate the two contributions and be able to determine the best detector parameters.

4.3 Description of available algorithms

The algorithms currently available are “Wolf” [44], ”Pandora PFA” [45] and “Track based PFA” [46].

The main function of a PFA is to reconstruct the clusters in the calorimeters and, using the information from all sub-detectors, perform the particle identification. Wolf, the simplest of the three, has a basic particle ID and can distinguish only four types of particles: electrons, photons, charged hadrons and neutral hadrons. Pandora PFA uses a more sophisticated algorithm. It tries several combinations of clustering to improve the matching between the cluster energy and the track momentum. It also looks for “kinks” in the tracks to reconstruct decayed particles. A unique feature of Pandora PFA is the possibility of performing a “cheated” cluster reconstruction. In this case all hits are associated to the correct particle using Monte Carlo information, so that the confusion term is zero. This type of reconstruction is called “Perfect PFA”. It must be noticed that this perfect reconstruction is limited to the single particles and not to the jets that are created at a later stage and might introduce a different confusion contribution. So far Pandora PFA is the only algorithm that has reached the goals for a LC detector resolution described in Section 4.1.

Track based PFA is a new algorithm and is still in an early development phase, nevertheless it can already achieve good performances as shown later. This algorithm uses charged tracks as seeds to reconstruct the clusters.

4.4 Comparison of PFAs using ZHH→llbbbb

The physics related to the ZHH channel has been presented in detail in Chapter 3. For the purpose of the study described in this section, ZHH→llbbbb is a channel with a complex final state that can test the PFA performance. ZHH→llbbbb is the abbreviation for Z→ll and both H→bb; this convention is used in all the thesis.

4.4.1 Event generation and detector reconstruction

The events were generated using version 3.3 of Pandora Pythia [47], including effects of initial and final state radiation, and bremsstrahlung. The mass of the Higgs was set to 120 GeV and its decay was forced to $b\bar{b}$. The energy of each beam was 250 GeV for a total CM energy of 500 GeV. The electron and positron beams had 80% and 0% polarisation respectively. For the detector simulation Mokka v06-00 was used [11].

The event reconstruction was performed using Marlin 09-07, an analysis tool for event reconstruction at ILC [48]. The event reconstruction started with the tracking reconstruction performed with the LEPTrack package [49]. Then the clustering and the particle flow were performed. For comparison, the three PFAs were applied on each event. The versions of the PFA software used were v1.6 for Wolf, v1.1 for Pandora PFA and v1.0 for Track Based PFA.

The detector model used in the study was LDC00Sc [50] which is described in Section 3.2.

4.4.2 Analysis of ZHH events

For this analysis a sample of ZHH events in which the Z decays into electrons or muons was used.

After the particle flow algorithm reconstructs all particles, the invariant mass of all possible pairs of electrons or muons was calculated. The pair with the invariant mass closest to the Z mass was selected. All the others particles were used to form the jets. Since at the time this analysis was performed no muon identification was available, muons were identified as pions. For this reason the muon channel had a higher combinatorial background, hence a higher possibility to select a pion instead of a muon. A wrong selection affected the jet reconstruction and therefore the reconstructed Higgs mass. A cut on the Z mass between 80 and 100 GeV was applied. The muon and electron channels were analysed separately.

The particles remaining in the event after the Z selection were forced to form four jets using the well known Durham algorithm [51]. This algorithm associates the

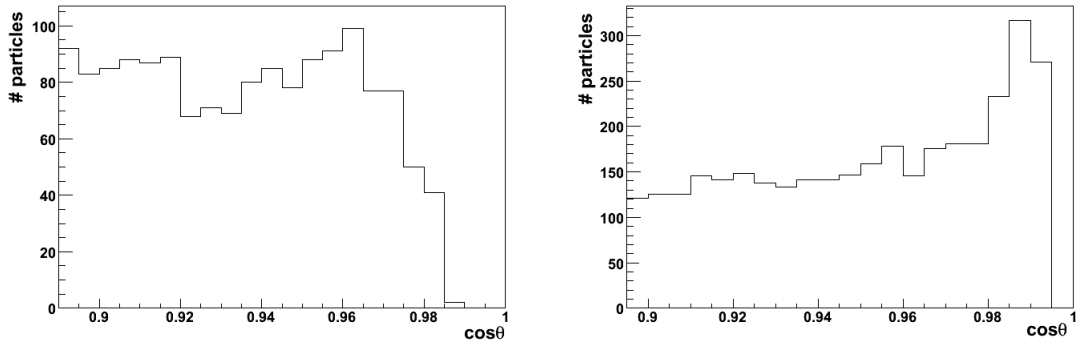

Figure 4.2: Angular distribution of charged (left) and neutral (right) particles in the beam pipe region of LDC00Sc detector using Pandora PFA.

two particles with the smallest angular distance until only the required number of jets is left. The four jets were paired in the three possible combinations and the one minimising the quantity

$$D^2 = (M_{ij} - M_H)^2 + (M_{kl} - M_H)^2 \tag{4.9}$$

was selected. In Equation (4.9), M_H is the generated mass of the Higgs while i, j, k and l are jet indices.

4.4.3 Effect of invisible particles on the Higgs mass peak

The effect of neutrinos and unseen particles (e.g. those lost in the beam pipe) had to be taken in to consideration. In the following, both categories of particles are referred to as "invisible particles". Using the Monte Carlo it was possible to recover the contribution from these particles to the Higgs mass.

The longitudinal angle θ is defined as the angle between the particle and the beam line. In order to estimate the detector acceptance, the distribution of cosθ of all charged and neutral particles was studied. In the forward region of the detector, where the efficiency was low, the particles were added to the event using the MC information. In Figure 4.2 the distributions of particles as a function of cosθ for all charged and neutral particles reconstructed by Pandora PFA in the LDC00Sc detector model are presented. Charged particles with $|\cos\theta| > 0.98$ and neutral particles with

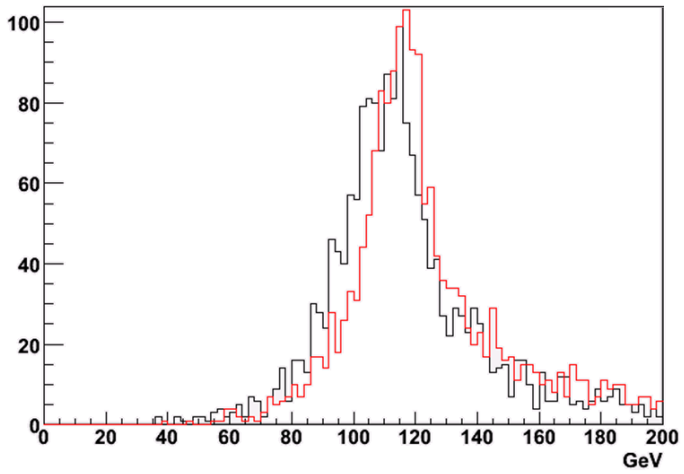

Figure 4.3: Mass distribution of the two Higgs for the electron channel using Pandora PFA. In black the distribution using only reconstructed particles, in red adding the invisible particles.

	Without invisible particles (GeV)	With invisible particles (GeV)
Mean	116.3	122.8
Sigma	25.2	25.2

Table 4.2: Mean and standard deviation of the reconstructed Higgs mass distribution with and without invisible particles.

$|\cos\theta| > 0.997$ were added to the reconstruction.

In Figure 4.3 the Higgs masses are plotted for Pandora PFA, with and without the contribution of invisible particles, for the electron channel. The mean and sigma of the distributions are summarised in Table 4.2. The distribution for the case when invisible particles have been included has a better peak at 120 GeV. The high value of the mean is due to the right tail in the mass distribution; this is due to bremsstrahlung photons not associated to the electrons from the Z. The contribution of invisible particles to the mass distribution is approximately 6 GeV, with the neutrinos alone contributing 3 GeV [52].

This result shows that the reconstructed Higgs mass in Equation 4.9 should be reduced from 120 GeV to 114 GeV. In fact the detector is sensitive only to visible particles which account for only 114 of the 120 GeV with which the Higgs had been generated. A wrong Higgs mass would lead to a wrong selection with the distribution of D^2 affected as well.

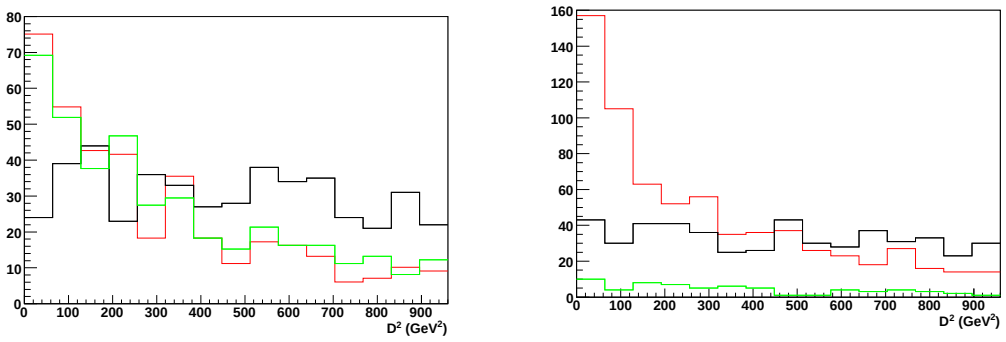

Figure 4.4: Distribution of the D^2 discriminator for the electron (left) and muon (right) channel; red is Pandora PFA, black is Wolf and green is Track based PFA reconstruction. The muon reconstruction problem with Track based PFA causes a very low performance for this PFA.

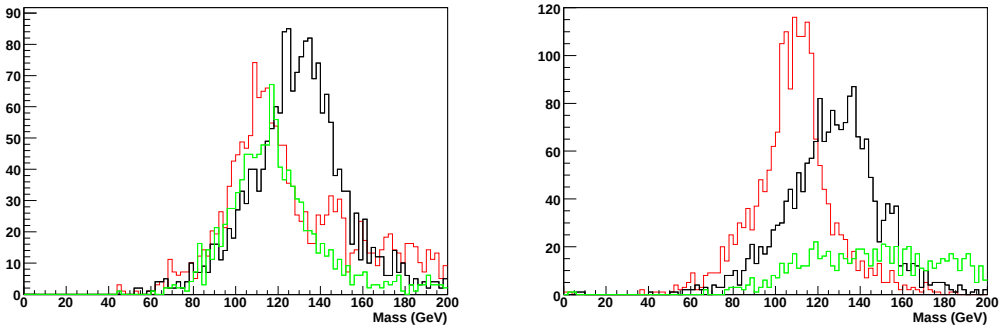

Figure 4.5: Distribution of the reconstructed Higgs bosons for the electron (left) and muon (right) channel; red is Pandora PFA, black is Wolf and green is Track based PFA reconstruction. The muon reconstruction problem with Track based PFA causes the wrong reconstruction of the Higgs mass.

4.4.4 Comparison between different PFAs

After the analysis described in Section 4.4.2, it was possible to compare the three PFAs using several variables. These are: the masses of the reconstructed Z and Higgs boson and the D^2 discriminator used in the selection. The distributions of these variables are shown in Figures 4.4, 4.5 and 4.6.

From these it was possible to see that Pandora PFA seemed to be the best particle flow available. The mass distributions were well centred on the expected values. The Wolf algorithm clearly performed less well; the reconstructed Higgs mass was too high for both the electron and the muon channels. Because of some features in the muon reconstruction, Track based PFA had a poor result in the muon channel; however in

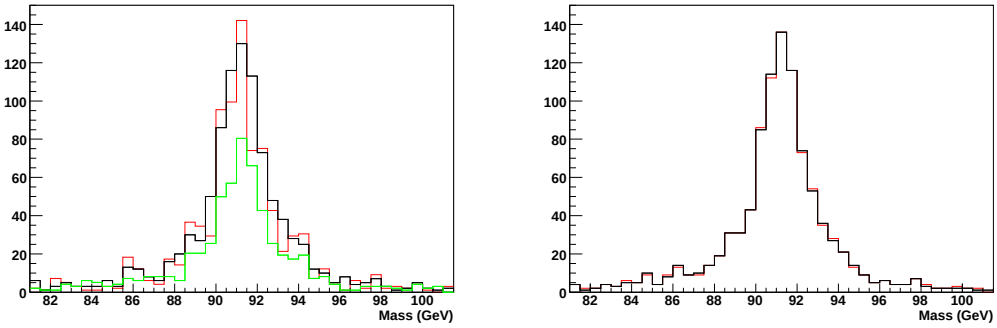

Figure 4.6: Distribution of the reconstructed Z boson for the electron (left) and muon (right) channel. Red is Pandora PFA, black is Wolf and green is Track based PFA reconstruction. The Z$\rightarrow \mu\mu$ reconstruction with Track based PFA is not shown in this Figure due to a known bug in the muon reconstruction.

the electron channel it reached almost the same resolution of Pandora PFA.

4.5 Conclusion

The analysis performed on the three available particle flow algorithms using the ZHH→llbbbb channel showed that the Pandora PFA algorithm had a better performance among the three algorithms available at present. The effect of invisible particles, such as neutrinos and particles escaping in the beam pipe, was considered. These particles accounted for about 6 GeV; for this reason, the Higgs mass used in the selection was 114 GeV instead of 120 GeV. The Wolf algorithm had the worst performance. In the electron channel the performance of Track based PFA was almost as good as Pandora PFA. Considering the events with $D^2 < 200$ Pandora PFA selected $\sim$ 15% more events than the Track based PFA. Pandora PFA had different performance in the muon and the electron channels; this was likely due to lack of muon identification and bremsstrahlung recovery. Pandora PFA is the best algorithm because it is more complex and is therefore better able to correctly reconstruct a larger variety of cases than Wolf or Track based PFA. Among the features that allow high performances is a complex refragmentation algorithm driven by the track momentum, a high performance photon finder and a sophisticated particle identification procedure.

As a result of this study, Pandora PFA was used for the six-jet analysis presented in Chapter 5.

Chapter 5

Analysis of the ZHH six-jet final state

At the energy of the Linear Collider, the ZHH is the only channel that can be used to investigate the self-coupling of the Higgs boson, with the six-jet final state as the main decay channel of this process. In addition to the physics motivations, this channel has also been suggested as one of benchmark channels for the optimisation of the detector [3]. The fast simulation studies, introduced in Section 3.3, indicate that it should be possible to measure the Higgs self-coupling with good precision; however this has never been proved with full Monte Carlo studies. In this chapter the first attempt to perform this analysis using full simulation and realistic reconstruction is described.

In the first section of this chapter the software used in the analysis and the chain from generation to reconstruction of all events are presented. Several studies on the six-jet final state are presented in Section 5.2. In Section 5.3 the list of variables used to select signal events is described and their cuts optimised. In Section 5.4, the bosons are reconstructed using several jet pairing algorithms for both realistic and perfect PFA. A further analysis using neural networks was developed and it is shown in Section 5.5. The performance of the b tagging reconstruction in the six-jet environment is presented in Section 5.6. In Section 5.7 all the results are summarised and compared to the results from the fast simulation studies.

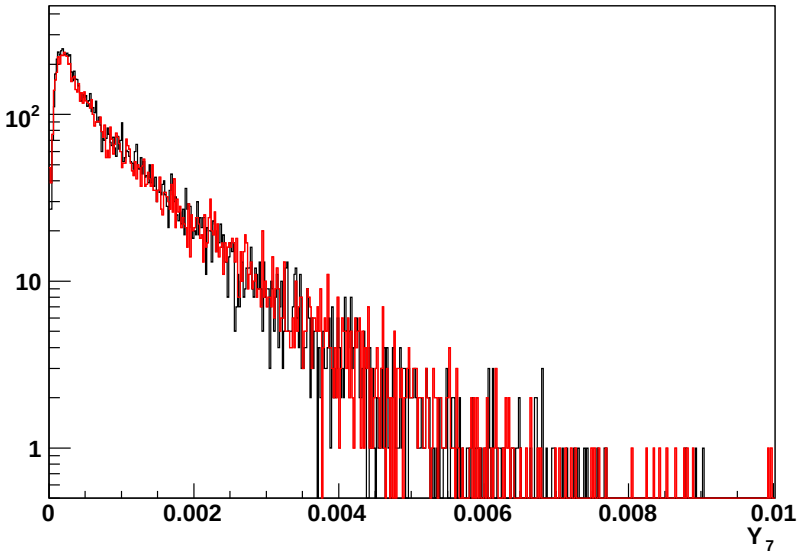

Figure 5.1: Y_7 distribution for samples generated with Pandora Pythia (black) and WHIZARD (red).

5.1 Event generation, simulation and reconstruction

5.1.1 Event generation

The events used in the ZHH analysis were generated using Pandora Pythia [47] and WHIZARD [28, 29, 30]. They use different approaches in producing an event. WHIZARD takes as input the required initial and final states (i.e $e^+e^- \rightarrow$ ZHH) and then sums all possible Feynman diagrams that contributes to that process taking into account possible interference terms. Pandora Pythia, on the other hand, generates events according to specific decay channels (i.e $e^+e^- \rightarrow$ ZHH $\rightarrow$qqbbbb). The two generators were compared looking at output of the Durham algorithm (Y_7, defined in Section 5.3.1) which is shown in Figure 5.1. This variable evaluates the fragmentation models used by the generators; from the distribution in the figure they were considered compatible.

It is computationally impossible to produce the simulation for the whole 500 fb^{-1} of data, which is the expected integrated luminosity during the first phase of the ILC. Since this analysis requires six jets, only events with six quarks in the final state and a selection of four-jet final states are considered. Table 5.1 summarises the number

Channel	σ(fb)	Evt. for 500 fb^{-1}	Evt. simulated	Generator
ZHH	0.147	73.5	10000	Pandora
ZHH	0.183	91.5	10000	Whizard
$t\bar{t}$ (total)	711	354000	375000	Pandora
$t\bar{t}$ →bbcqcq	81.94	40970	45000	Pandora
$t\bar{t}$ →bbcquq	163.38	81690	85000	Pandora
$t\bar{t}$ →bbuquq	81.94	40970	45000	Pandora
$t\bar{t}$ →Semileptonic	311.2	155600	160000	Pandora
$t\bar{t}$ →Leptonic	73.0	36500	40000	Pandora
WWZ	212.9	106450	120000	Whizard
ZZH→qqqqbb	0.502	251	1000	Pandora
ZZZ	1.486	743	5000	Whizard
ZZ→qqQQ	90.5	45250	50000	Pandora
ZH→qqbb	13.66	6830	20000	Pandora
tbtb	0.434	217	5000	Whizard
Wtb	44.34	22170	25000	Whizard
ttH	0.237	118.5	5000	Whizard
ttZ	1.016	508	5000	Whizard

Table 5.1: List of events generated for each channel.

of generated events and the generator used for all channels used in this analysis. The $t\bar{t}$ channel is the main background because of its cross section; for this reason the generation of $t\bar{t}$ events was performed according to the different W decay modes. The symbol Q in Table 5.1 indicates heavy flavour quarks (c and b); the high cross section ZZ channel was generated requiring at least one Z to decay to one of the two heavy quarks. Since the analysis requires four b jets to be identified, at least two b jets were requested. C-jets were included since they are the most likely jets to be mis-tagged as b jets.

5.1.2 Detector simulation

The detector simulation was performed using MOKKA v00-06-04p02 [11]. The detector model used was LDC00Sc that is described in Section 3.2. A more detailed description of the detector can be found in [50].

5.1.3 Event reconstruction

The simulated events were reconstructed using Marlin v00-09-10 [48]. The hits in the tracking and calorimetry systems are digitised and then used as input for the tracking and particle flow reconstruction. An extensive overview of the reconstruction is presented in Appendix A.

All reconstructed particles with an energy above 20 MeV were forced to six jets using the Durham algorithm [51]. The next step was the vertex reconstruction which was performed by the LCFI vertex reconstruction software described in [33]. This software is based on the ZVTOP algorithm [53] developed for the SLD experiment, which guarantees a high reliability, and uses neural networks to identify the vertex flavour. The software can identify b and c vertices and evaluate their charge. Different networks have been trained by the authors using $Z \rightarrow qq$ events; for b tagging, one for c tagging and one for c tagging assuming only b jets background. The networks trained with two-jet events work also in the six-jet environment although the performance is affected by the different environment as described in Section 5.6. The output of each network is a number between 0 and 1 where 1 indicates high probability and 0 low probability to be a b or c jet. Expected performance in a two-jet environment is shown in Figure 3.11.

In this analysis the particle flow algorithm Pandora PFA was used since this was shown to be the best available in the study described in Chapter 4. In order to determine the contribution of the PFA to the final measurement, Perfect Pandora PFA (see Section 4.3 for the definition) was used on the same events. Six different jets were obtained from the Perfect PFA list of particles and for each of them the vertex was reconstructed.

The reconstructed particles and the jets, for both the realistic and perfect PFA chain of reconstruction, were then used to calculate several shape variables which are used in this analysis.

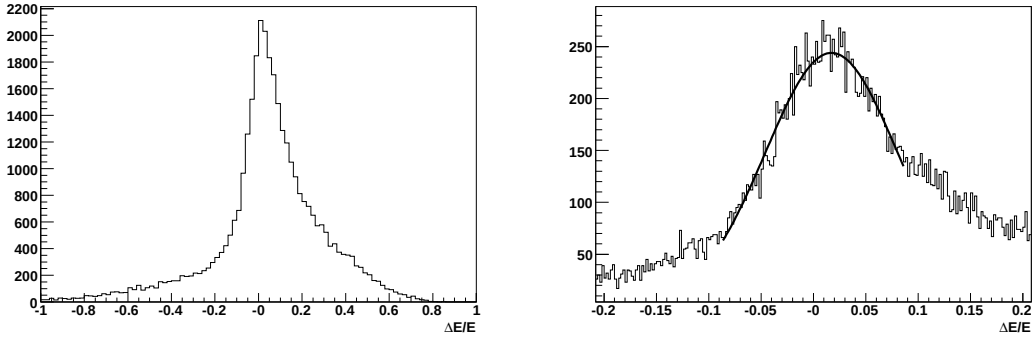

Figure 5.2: Distribution of the jet energy resolution for jets between 40 and 60 GeV. On the right, the core of the distribution is fitted with a Gaussian function.

5.2 Preliminary studies on the six-jet final state

In this section some properties of jets in the six-jet environment are studied using the ZHH sample. Each reconstructed jet had to be associated to one of the Monte Carlo quarks from the boson decays. In order to do that, the sum of the six scalar products between the momentum vectors of the reconstructed jets and the Monte Carlo quarks was evaluated for all possible 720 combinations. The combination that maximised the sum was chosen.

5.2.1 Jet energy resolution

The jet energy resolution was evaluated by dividing the jets in energy bins of 20 GeV. For each bin the distribution of the resolution, defined as

$$\sigma = \frac{E_{jet} - E_{quark}}{E_{quark}},$$

was plotted. The energy of the quark was considered to be the true energy of the jet. Figure 5.2 shows such a distribution for jets with an energy between 40 and 60 GeV. This distribution and those obtained for the other energy bins are asymmetric due to several effects such as calorimeter non-linearity, particles mis-associated to the jet and, at higher energies, leakage effects. For each distribution the core of the peak was fitted with a Gaussian function as shown in the same Figure. The standard deviation

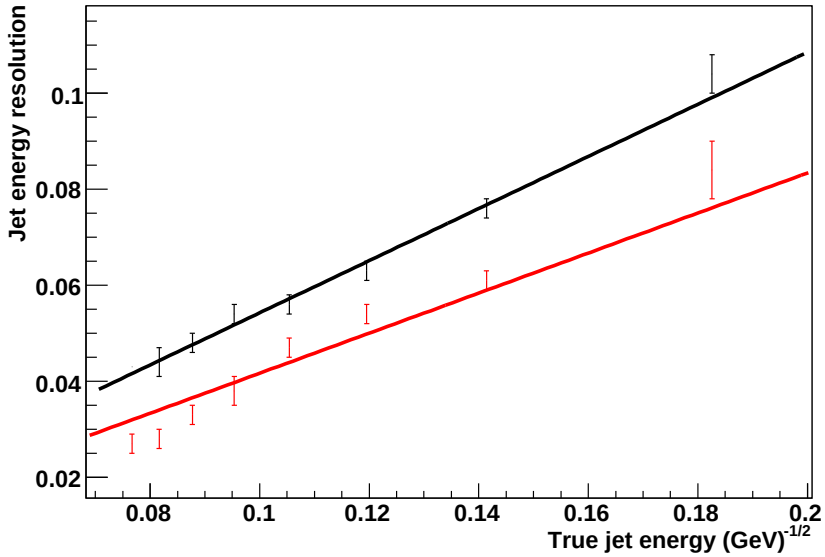

Figure 5.3: Jet energy resolution as a function of $1/\sqrt{E_{true}}$. Reconstructed jet in black, jet reconstructed using perfect PFA in red.

Realistic PFA	Generator Mass (GeV)	Mass (GeV)	Width (GeV)
Higgs	120	116.6 ± 0.3	7.2 ± 0.4
Top	174.2	172.8 ± 0.4	20 ± 2
Z	91.187	90.3 ± 0.1	6.0 ± 0.1
W	80.425	79.9 ± 0.1	4.8 ± 0.1

Table 5.2: Bosons mass and width for realistic PFA.

evaluated in each fit was plotted as function of $1/\sqrt{E_{true}}$ and it is shown in Figure 5.3. The reconstructed jets using realistic PFA are in black while the jets obtained with perfect PFA are in red. The lines are the linear fit with zero constant term to the points and they give the resolution as function of $1/\sqrt{E}$. For realistic PFA the jet energy resolution was $(54 \pm 1)\%/\sqrt{E}$ while for perfect PFA the jet energy resolution was $(42 \pm 1)\%/\sqrt{E}$.

5.2.2 Mass resolution

Using the association between jets and quarks described before, it was possible to reconstruct the particles using the correct jets. Tables 5.2 and 5.3 summarise the masses and the widths obtained for all bosons and the top quark for the realistic and perfect PFA respectively. Comparing the two tables, it is possible to see that

Realistic PFA	Generator Mass (GeV)	Mass (GeV)	Width (GeV)
Higgs	120	115.6 ± 0.2	5.8 ± 0.4
Top	174.2	169.1 ± 0.3	15 ± 2
Z	91.187	88.7 ± 0.1	5.1 ± 0.2
W	80.425	78.6 ± 0.1	3.8 ± 0.1

Table 5.3: Bosons mass and width for perfect PFA.

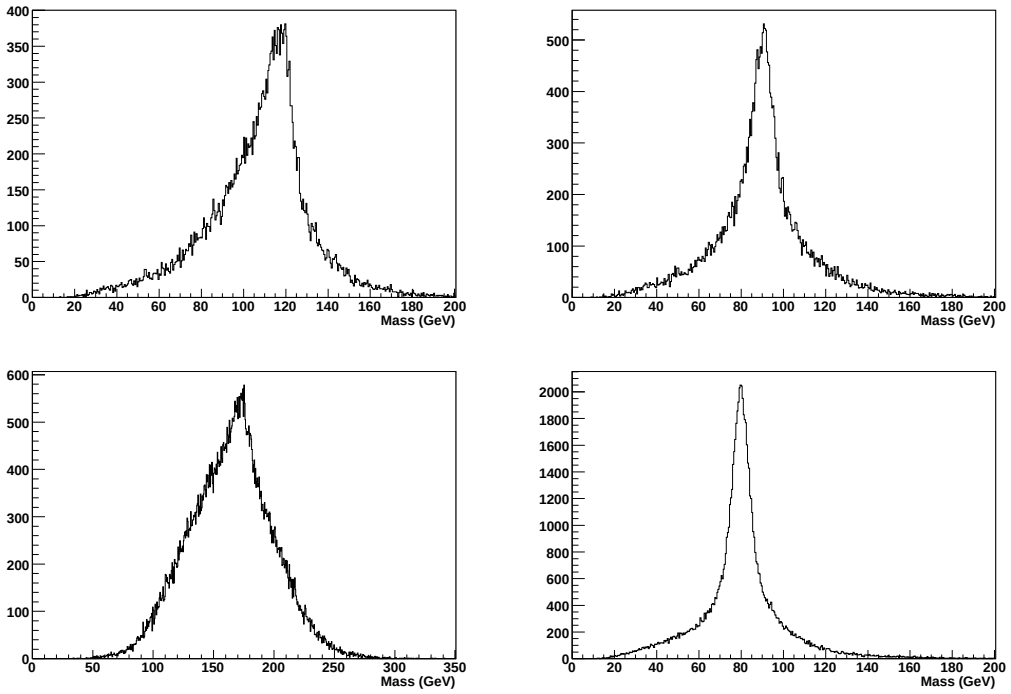

Figure 5.4: Mass distribution for the Higgs (top left), Z (top right), top (bottom left) and W (bottom right) assuming perfect pairing of the jets.

the perfect PFA reconstructs slightly smaller masses. This effect is due to the MIP to energy calibration in the particle flow. In fact, in the case where a cluster from a charged hadron is split in more clusters and only one is associated with the track, additional energy is created in the detector in the form of neutral hadrons. The energy calibration of all clusters has been performed so that the total amount of reconstructed energy is correct. Since perfect PFA does not have such additional clusters (i.e. all hits are associated with the correct cluster using the Monte Carlo information), the total visible energy is smaller than the realistic reconstruction. This relatively small effect was corrected by using the masses of Tables 5.2 and 5.3 in the realistic and perfect reconstruction instead of the generator masses.

The mass distributions of the Z, W, Higgs and top quark are shown in Figure 5.4.

From these distribution it is possible to see the effect of b jets to the mass of a particle. The neutrinos in the b jets are the cause of the asymmetry in the Higgs and the top quark mass distribution. The Z and W masses distributions presented in the same Figure are much more symmetric since they have smaller b jets content. Particles decaying in to b jets had also a smaller mass than the one used in the generator for the same reason.

5.3 Cut based analysis

In this section a cut based analysis to select ZHH events is described.

5.3.1 Event selection

The preliminary event selection was based on the analysis described in [34]. The variables used in the analysis are listed below with some examples of distributions of signal and significant backgrounds.

- **Thrust**. The thrust is defined as:

$$Thrust = max \frac{\sum_i |\mathbf{n} \cdot \mathbf{p}_i|}{\sum_i \mathbf{p}_i},$$

  where $\mathbf{n}$ is the direction of the thrust while $\mathbf{p}_i$ is the momentum of the i-th track. An event with high thrust develops along an axis (back-to-back event) while a multi-jet spherical event is characterised by a low thrust since there is no preferred direction in the event. This variable is useful to reduce two- and four-fermion final state events. Figure 5.5 shows the normalised distributions of the thrust for the signal and the ZH background.

- **cos(θ_{thrust})**. This variable can separate events produced in the central region of the detector from those produced in the endcaps. Signal and backgrounds have different distributions of cos(θ_{thrust}); the normalised distributions for WWZ, $t\bar{t}$ and signal are presented in Figure 5.6.

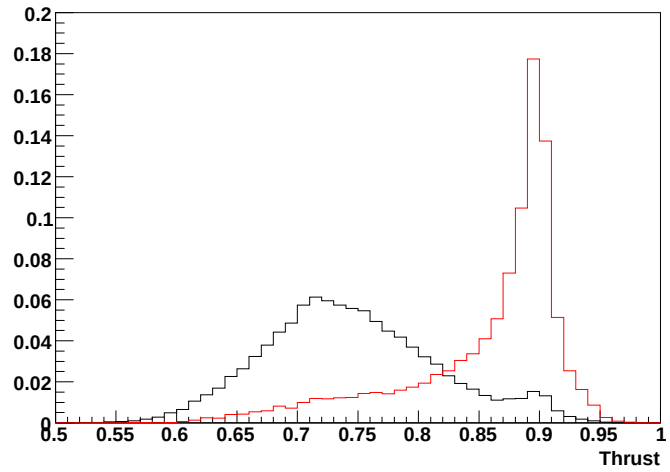

Figure 5.5: Distribution of the thrust for signal (black) and ZH background (red). The distributions are normalised to have the same area.

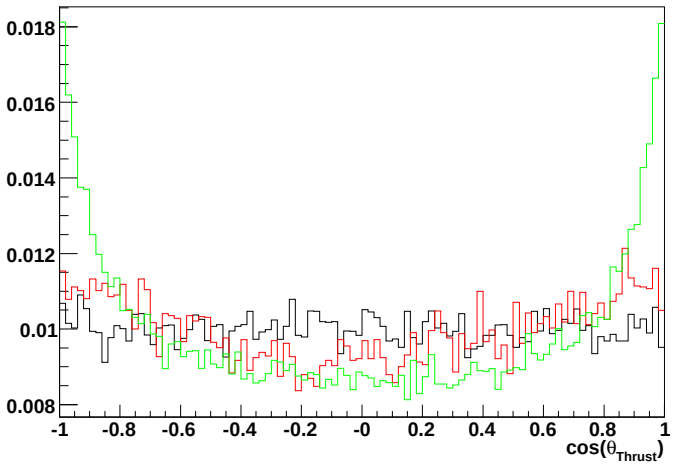

Figure 5.6: Distribution of $\cos(\theta_{thrust})$ for signal (black), $t\bar{t}$ (red) and WWZ (green). The distributions are normalised to have the same area.

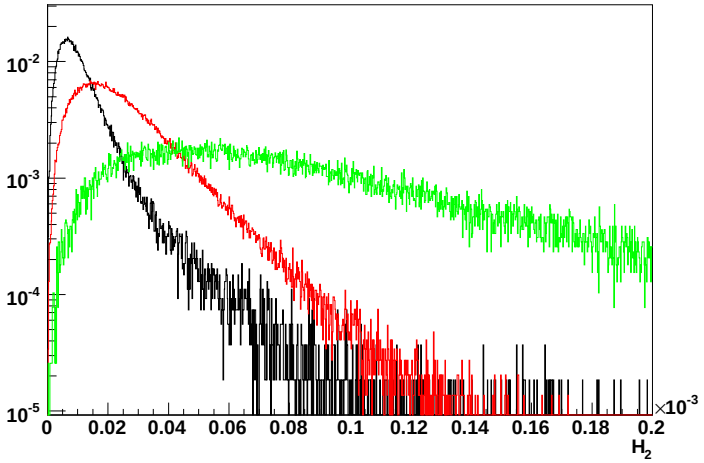

Figure 5.7: Distribution of second Fox-Wolfram moment for signal (black), leptonic (green) and semileptonic (red) decay of $t\bar{t}$. The distributions are normalised to have the same area.

- **Fox-Wolfram moments**. These global variables summarise how an event develops looking at the angles between all particles. The generic l-th moment is defined as:

$$H_l = \sum_{i,j} \frac{\mathbf{p}_i \cdot \mathbf{p}_j}{E_{vis}^2} P_l(\cos\theta_{ij}).$$

  where P_l are the Legendre polynomials. The sum is performed on all pairs of particles. All moments are then normalised to H_0. For this analysis the second Fox-Wolfram moment is used. This variable can separate the signal from non-six-jet backgrounds. Figure 5.7 shows the distributions of this variable for the signal and the leptonic and semileptonic $t\bar{t}$.

- **Total energy**. This is the total visible energy in the event and is a useful discriminator for events with missing energy such as all Z and W decays containing neutrinos. Figure 5.8 shows the total energy distributions for the signal and the $t\bar{t}$ leptonic channel.

- **Number of particles in jet**. This variable is used to eliminate events with isolated particles (in general leptons) which are reconstructed as a jet. A typical case of a single particle forming a jet is given by the semileptonic channel of the $t\bar{t}$; since the lepton is isolated from the other particles, the jet finder creates a

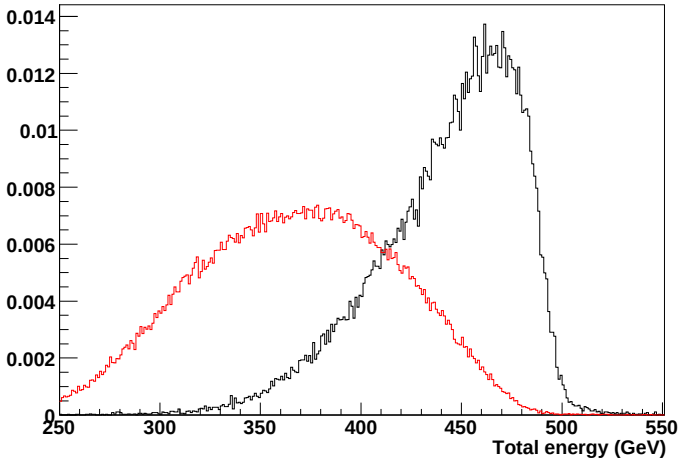

Figure 5.8: Distribution of the total energy for signal (black) and semileptonic $t\bar{t}$ channel (red). The distributions are normalised to have the same area.

jet with a single particle. More often some low momentum particles are added to this isolated particle. The distributions of the number of particles in a jet for the signal and the semileptonic $t\bar{t}$ are shown in Figure 5.9.

- **Jet EM energy ratio**. The ratio of electromagnetic energy over the total energy of the jet is used to reject events in which single electrons or photons have been selected as jets in a similar way as described above. The signal and the semileptonic $t\bar{t}$ channels distributions for this variable are shown in Figure 5.10.

- **Angular distance between jets (Y_6)**. The Y_i are defined as:

$$Y_i = 2min\left\{E_i^2, E_{i-1}^2\right\}(1 - \cos\theta_{i,i-1}),$$

where E_i and E_{i-1} are the energy and $\theta_{i,i-1}$ is the angle between the two particles. The Durham algorithm used by the jet finder merges the two having the smallest Y value in a jet until the number of jet matches the required number. This variable should discriminate between six-fermion final states and final states with a lower number of fermions. The Y_6 distributions for the signal and the ZZ background are shown in Figure 5.11.

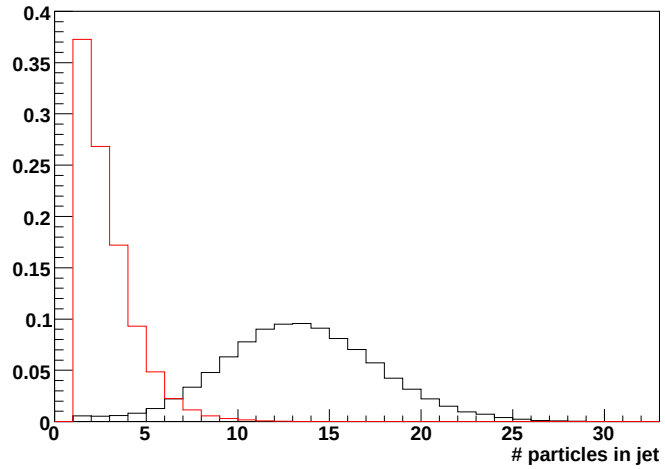

Figure 5.9: Distribution of the number of particles in a jet for signal (black) and semileptonic $t\bar{t}$ channel (red). The distributions are normalised to have the same area.

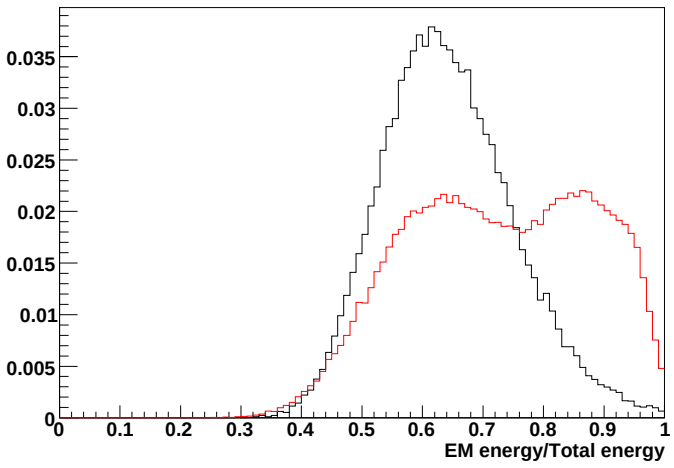

Figure 5.10: Distribution of the ratio of electromagnetic and total energy for signal (black) and semileptonic $t\bar{t}$ (red). The distributions are normalised to have the same area.

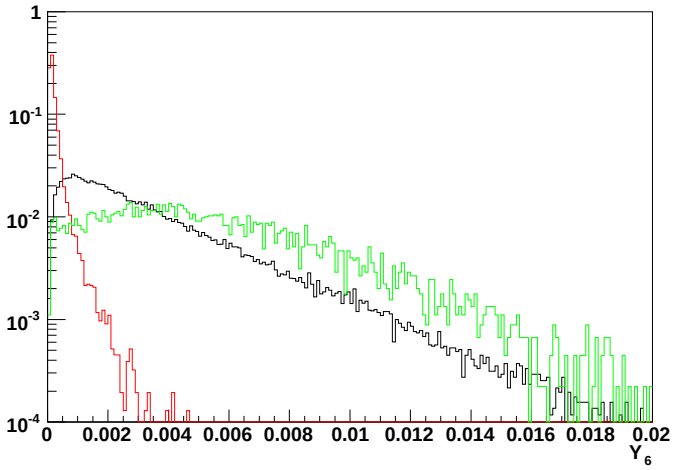

Figure 5.11: Distribution of Y_6 for signal (black), ZZ (red) and tbtb (green) events. The distributions are normalised to have the same area.

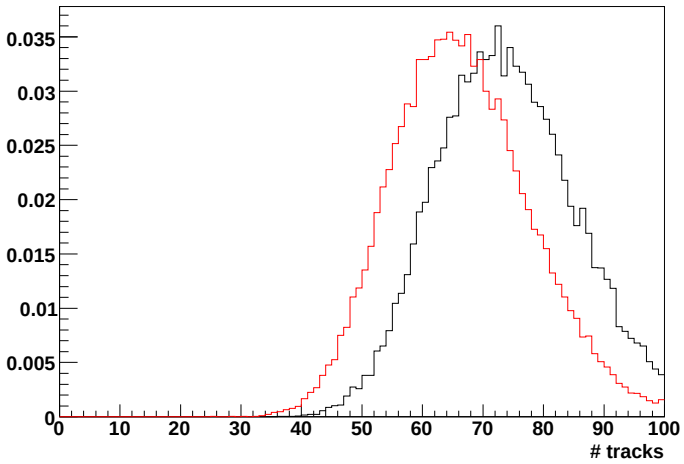

Figure 5.12: Distribution of the total number of tracks for signal (black) and hadronic $t\bar{t}$ (red). The distributions are normalised to have the same area.

- **Number of tracks**. This variable is very useful since in general b jets have more tracks than light jets. Since the signal has four b jets, a higher number of tracks is expected for the ZHH than for other six-jet events. This variable is not correlated with the b tagging because the information used is different, therefore it can help in discriminating real multi-b events from events with mis-tagged jets. Figure 5.12 shows the distributions of the total number of tracks for the signal and the hadronic $t\bar{t}$ channel.

- **Total NN b tag**. This variable is the sum of the outputs of the b tagging

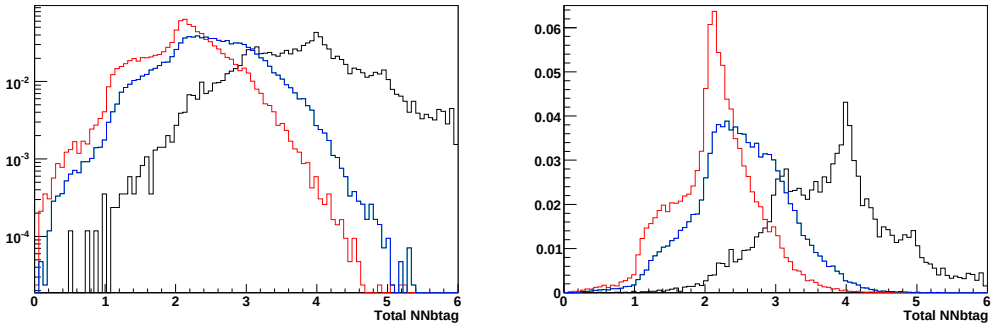

Figure 5.13: Distribution of the total output of the b tagging neural network for signal (black) and two hadronic $t\bar{t}$ samples: in blue is shown $t\bar{t} \to$ bbcscs while in red $t\bar{t} \to$ bbcsud . The distributions are normalised to have the same area and are presented in logarithmic (left) and linear (right) scale.

neural network for each jet. It plays a key role in reducing the background since the signal has four b jets while $t\bar{t}$ should have only two b jets. However the inefficiency in reconstructing all the b jets in the signal and the contamination from mis-tagged c jets in the $t\bar{t}$ sample cannot guarantee a perfect separation. The distributions for the signal and the $t\bar{t} \to$ bbcscs sample are shown in Figure 5.13.

5.3.2 Cut optimisation

The usual figure of merit $S/\sqrt{S+B}$, where S indicates the number of signal events and B the number of background events, was used to optimise all cuts in this analysis. It is commonly required to achieve a value of $S/\sqrt{S+B} = 3$ for evidence and $S/\sqrt{S+B} = 5$ for discovery. The most important variable of those listed above is the b tag variable. Starting from a value of 3.5, taken from the fast simulation studies [34], several values of the cut were tried in steps of 0.1. A cut at 3.9 was chosen giving a $S/\sqrt{S+B} = 0.237 \pm 0.002$; the error is statistical. This value is small and indicates that the signal cannot be separated from the background; for this reason other variables were studied to increase the $S/\sqrt{S+B}$.

The optimisation was performed scanning simultaneously all variables along a wide range of values. However the high number of variables made it difficult to test many values because of the processing time and the memory requirement. A satisfactory

	Cut Value	Cut Value for Perfect PFA
Thrust	0.84	0.85
$\cos(\theta_{thrust})$	1	1
$Y_6(*)$	0.00021	0.00021
Jet EM energy ratio	0.925	0.925
# of particles in jet	6	6
Total energy (GeV)	373	355
$H_2 \times 10^{-3}$	0.0175	0.02
# of track	44	44
Total NN b tag	3.9	3.9

Table 5.4: Final value of the cuts used in the analysis.

Channel	Efficiency	Efficiency Perfect PFA
ZHH	0.423	0.405
$t\bar{t}$ →bbcqcq	0.0167	0.0163
$t\bar{t}$ →bbcquq	0.0070	0.0069
$t\bar{t}$ →bbuquq	0.0025	0.0027
$t\bar{t}$ →semileptonic	0.0003	0.0003
$t\bar{t}$ →leptonic	0	0
ZH	0.0004	0.0007
ZZ	0.00002	0
WWZ	0.0003	0.0004
Wtb	0.0003	0.0005
ttH	0.118	0.116
ttZ	0.028	0.028
tbtb	0.130	0.129
ZZH	0.132	0.128
ZZZ	0.008	0.009

Table 5.5: Efficiency of the selection for each channel.

compromise was found using five cut values for each variable; for example, for the total energy (Figure 5.8) the five starting values were 350, 375, 400, 425 and 450 GeV. Among all possible combination of cuts (there are 5^8), the one that maximises the $S/\sqrt{S+B}$ was chosen. The procedure was iterated several times with increasingly smaller segmentation around the chosen values until no significant improvement is achieved changing the cuts. Continuing with the total energy example, having found 375 as the best cut in the first iteration, the values chosen for the second iteration were 355, 365, 375, 385 and 395 GeV and in the last iteration the values 371, 372, 373, 374 and 375 GeV were used.

Table 5.4 summarises the selected cut value for each variable. Table 5.5 shows the

efficiency of the selection for the signal and the backgrounds; the efficiency is defined as the number of events passing the cuts over the total number of events. One of the results of the optimisation is that the $\cos(\theta_{thrust})$ is not useful in order to discriminate the backgrounds indicating that other variables are more efficient in rejecting those channels, like WWZ and tbtb, that the $\cos(\theta_{thrust})$ was supposed to reject.

The $S/\sqrt{S+B}$ at this stage of the analysis was 0.364 ± 0.011. The number of signal was 13.5 while the background events passing the cuts were 1364.5. The same procedure was performed on the perfect PFA reconstruction obtaining very similar cut values and a $S/\sqrt{S+B}$ of 0.361 ± 0.010; the two numbers were compatible within the statistical error.

5.4 Boson mass reconstruction

5.4.1 Simple jet pairing

In order to reconstruct the three boson masses, a χ^2 was built to force a reconstruction to ZHH:

$$\chi^2 = \frac{(M_{ij} - M_Z)^2}{\sigma_Z^2} + \frac{(M_{kl} - M_H)^2}{\sigma_H^2} + \frac{(M_{mn} - M_H)^2}{\sigma_H^2}. \tag{5.1}$$

The masses and the σ of the Higgs and the Z bosons used in the χ^2 are those obtained in Section 5.2.1. All forty five combinations of the six jets were tried. The combination that produced the smallest χ^2 defined the χ^2_{min} for that event. χ^2_{min} was then used to discriminate signal from backgrounds.

Figure 5.14 shows the distribution of χ^2_{min} (called simply $\chi^2$from now on) for signal (black) and backgrounds (colours); each channel is weighted by its cross section. In order to optimise the cut on χ^2, the figure of merit $S/\sqrt{S+B}$ was plotted as function of the χ^2; the cut should be placed at the maximum of this distribution. Figure 5.15 shows that a cut on the χ^2 would not improve the result, since the highest separation is achieved for high values of χ^2. In this case all events, signal and background alike,

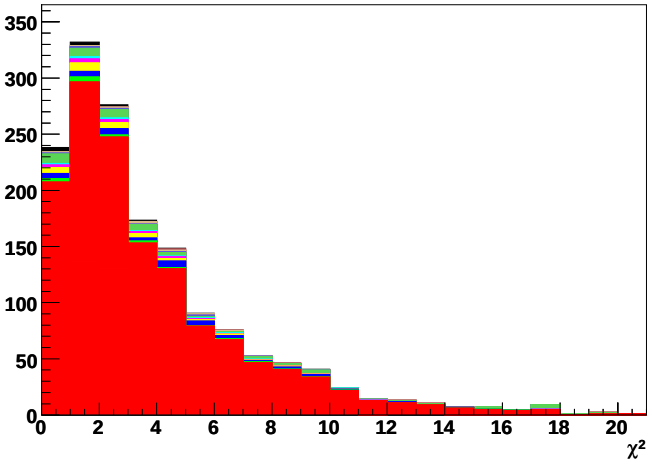

Figure 5.14: Distribution of χ^2 for signal (black) and backgrounds; red is hadronic tt, the other colours represent the different backgrounds.

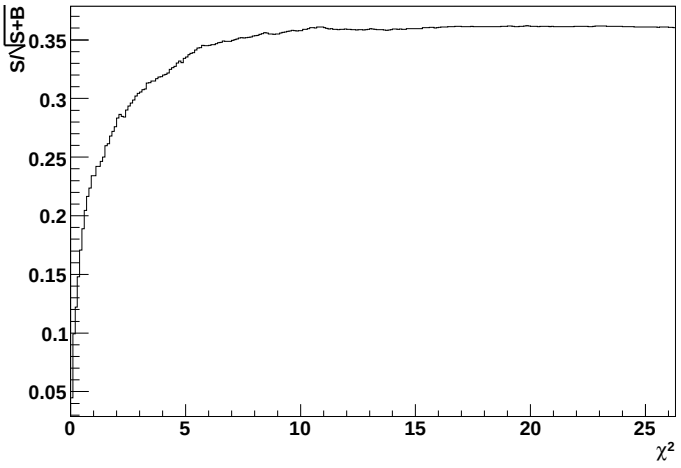

Figure 5.15: $S/\sqrt{S+B}$ as a function of χ^2 using the χ^2 definition of equation 5.1.

are used. The reason for poor separation is the large number of hadronic $t\bar{t}$ events that pass the selection and, due to the high combinatorial for jet pairing, are reconstructed to look similar to ZHH events.

5.4.2 Jet pairing with b tag information

In order to reduce the combinatorial background and further use the b tagging information a second χ^2 was defined as

$$\chi^2 = \frac{(M_{ij} - M_Z)^2}{\sigma_Z^2} + \frac{(M_{kl} - M_H)^2}{\sigma_H^2} + \frac{(M_{mn} - M_H)^2}{\sigma_H^2} + \sum_{J_H=1}^{4} A(Btag(J_H) - 1)^2. \quad (5.2)$$

The first three terms of this χ^2 are identical to those defined for Equation (5.1). The new term uses the b tag information with the value of A usually very large as described later. Since the four jets from the two Higgs bosons should be b jets, the output of the b tagging neural network should peak at 1 hence the sum of the four terms should peak at zero for well reconstructed and well associated jets in signal events. Since b-like jets are more likely to form one of the Higgs boson instead of the Z, the new term effectively reduces the number of possible combinations.

However this term had to be optimised with respect to the other terms. The A constant is a parameter that represents the relative weight of the mass terms and the b tag term. The optimisation of this parameter was performed varying the value from 0 to 10^5. For each value of A the same procedure described before was performed; the minimised χ^2 was plotted for signal and background and from this distribution the $S/\sqrt{S+B}$ was maximised. Figure 5.16 shows the distribution of $S/\sqrt{S+B}$ as a function of the χ^2 for A=1000.

Figure 5.17 shows the maximum of $S/\sqrt{S+B}$ as a function of A. The error is the statistical error mainly due to the limited amount of simulated $t\bar{t}$. For values above 100 the separation is constant at a value of 0.55 ± 0.06. This is a significant improvement with respect to the previous result of $S/\sqrt{S+B} = 0.364 \pm 0.011$, which

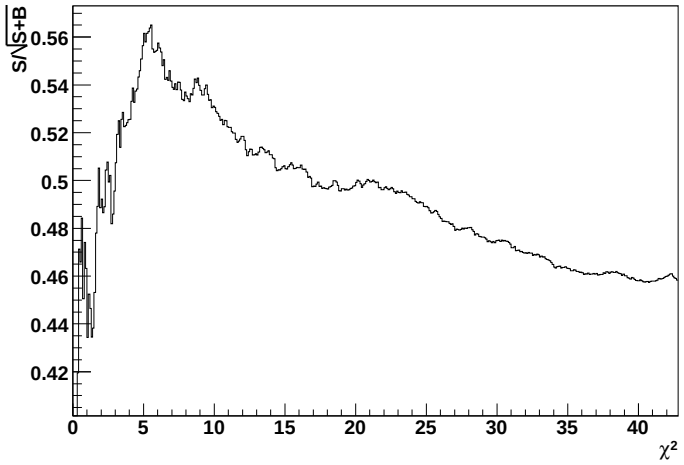

Figure 5.16: $S/\sqrt{S+B}$ as a function of χ^2 using the χ^2 definition of equation 5.2.

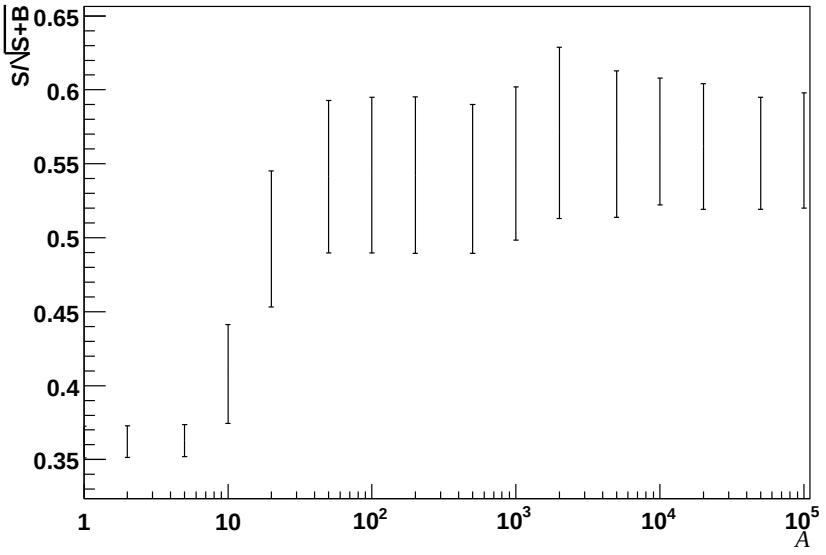

Figure 5.17: $S/\sqrt{S+B}$ as a function of A.

is possible thanks to the b tagging information.

5.4.3 Kinematic fitting in jet pairing

A technique that can improve the result of the previous analysis is the kinematic fit. This is a standard technique that has been widely used in multi-jet environments at LEP and the Tevatron (see [54, 55] for examples). The idea is to make use of known information, such as the mass and the width of a particle, and force the reconstructed particles to have the same values. Several constraints can be applied to an event: on the total energy, on total momentum and on the mass and width of the reconstructed particles. Depending on the type of particles to be reconstructed, different constraints can be used: for example in the W mass kinematic fit at LEP, the requirement was to have two particles with the same mass while it is possible to force a Higgs to its theoretical mass or use the experimental resolution typical of the analysis. The constraints are enforced by smearing the jet four-vectors and the quality of the fit is usually controlled by including a term that measures the difference between the original and final values of the four-vectors taking into account the errors on the measurements.

In this analysis the kinematic fit was implemented extending the χ^2 definition of Section 5.4.2. Since the direction of the jets is reconstructed with much higher precision than the jet energy (see [56]), only the jet energy was smeared. A constraint on the total energy was found to be ineffective for this selection and was dropped. MINUIT was used to minimise the new χ^2 defined as:

$$\begin{aligned}\chi^2 &= \frac{(M_{ij}^{fit}-M_Z)^2}{\sigma_Z^2} + \frac{(M_{kl}^{fit}-M_H)^2}{\sigma_H^2} + \frac{(M_{mn}^{fit}-M_H)^2}{\sigma_H^2} + \\ &+ \sum_{J_H=1}^{4} A(Btag(J_H)-1)^2 + \sum_{i=1}^{6} \frac{(E_i^{fit}-E_i)^2}{\sigma_i}.\end{aligned} \tag{5.3}$$

The first three terms are identical to those of equation 5.2 except that the masses were reconstructed using the energy obtained from the minimisation. Moreover two different values of σ_H were used to constrain the Higgs boson; the "soft constraint" used the value $\sigma_H = 7.2\,\text{GeV}$, the experimental resolution estimated in Section 5.4,

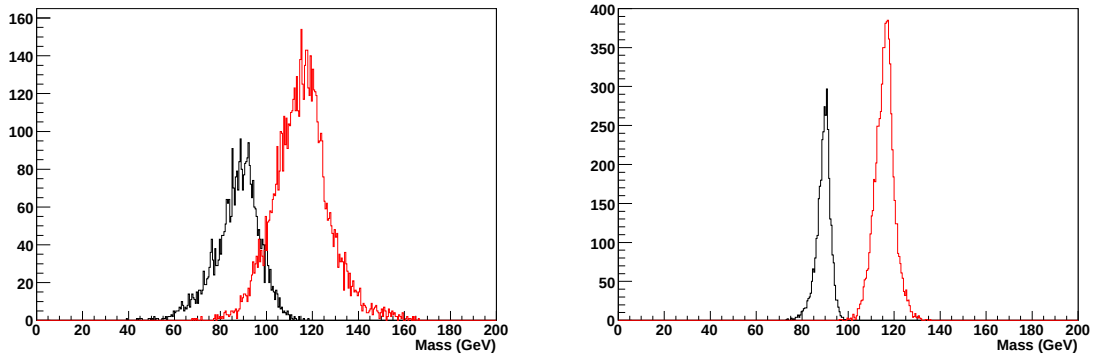

Figure 5.18: Mass distribution for the selected Z (black) and Higgs (red) for the non-kinematic selection (left) and the selection using the soft constraint for the kinematic fitting (right).

while the "hard constraint" used $\sigma_H = 0.03\,\text{GeV}$, the theoretical width of a 120 GeV Higgs boson, forcing the jets to form a boson with the input Higgs mass. Results with both constraints are presented below.

The new term is the jet energy term, where E_i^{fit} is the fitted energy and E_i is the reconstructed energy. σ_i determines how much the jets can be smeared; the values used for σ_i were those evaluated in Section 5.2.1. Figure 5.18 shows the improvement in the reconstructed Z and Higgs masses with respect to the previous selection using the soft constraint.

The same analysis to optimise A in the b tagging term described in Section 5.4.2 was performed. Figure 5.19 and 5.20 show the best $\text{S}/\sqrt{\text{S}+\text{B}}$ as a function of A for the soft and hard constraints respectively; in both cases the best separation achieved was $\text{S}/\sqrt{\text{S}+\text{B}} = 0.56 \pm 0.06$. Within the statistical error there was no improvement in the signal/background separation using the kinematic fitting.

5.4.4 Results for perfect PFA

The methods to pair the jets to form the bosons presented in the previous sections for realistic PFA were applied to the perfect PFA reconstruction. Figure 5.21 shows the result for the optimisation of the parameter A in the case without the kinematic fit and for both options in the kinematic fit. The different performance in PFA lead to a different value in the optimisation of this parameter with respect to the realistic PFA

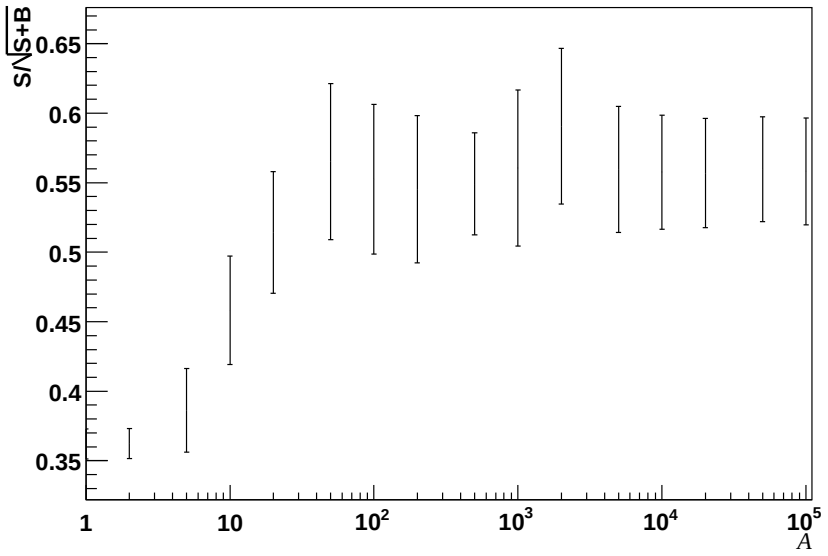

Figure 5.19: $S/\sqrt{S+B}$ as a function of A for the kinematic fit analysis using the "soft constraint".

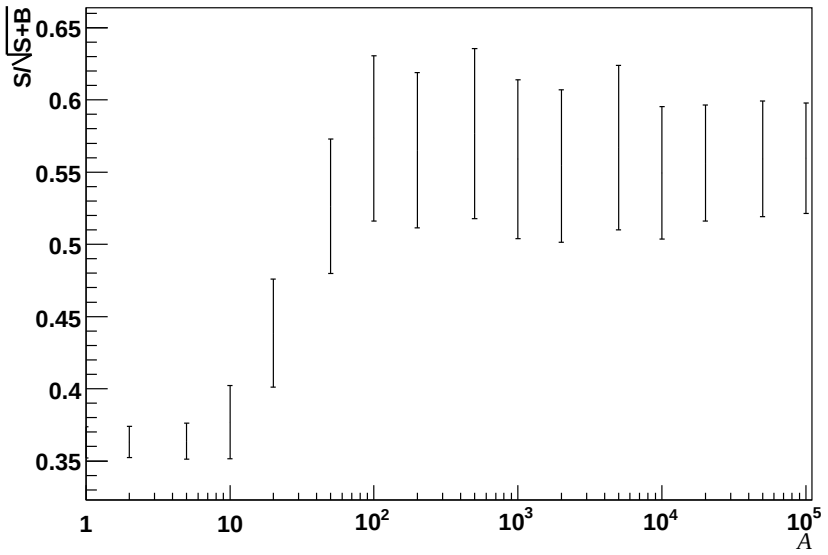

Figure 5.20: $S/\sqrt{S+B}$ as a function of A for the kinematic fit analysis using the "hard constraint".

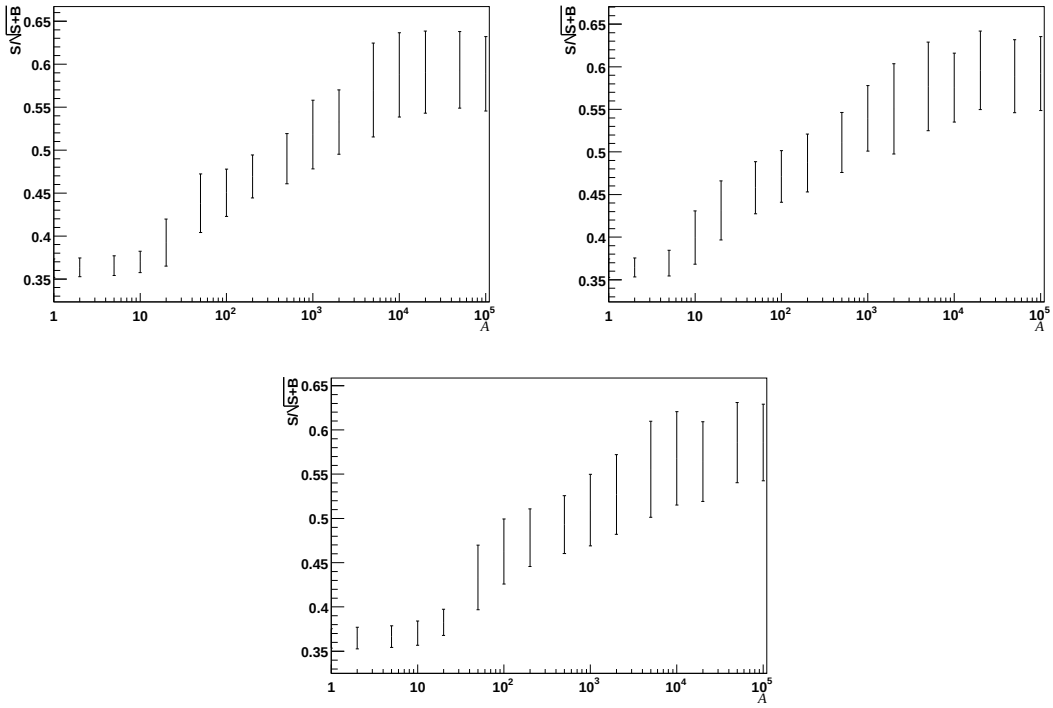

Figure 5.21: $S/\sqrt{S+B}$ as a function of A for the non-kinematic case, the soft constraint and the hard constraint cases.

reconstruction. As in the previous case, there was no difference using the kinematic fit. For perfect PFA reconstruction, $S/\sqrt{S+B} = 0.59 \pm 0.06$ which, within the statistical error, was compatible with the case of realistic PFA. This means that any improvement in the PFA will not reflect in a better separation in this analysis. In order to have a better separation the other main element of the selection, the vertex reconstruction for the b tagging, has to be improved.

5.5 Neural network analysis

A final analysis was performed using a neural network, which in principle should give a better separation between the signal and the backgrounds then the cut based one. Two studies were carried out, the first using the variables described in Section 5.3.2 to check the result obtained while the second used the b tagging and the masses information to evaluate the sensitivity to the ZHH cross section. The result of the latter analysis can also be better compared with the two results from the fast Monte

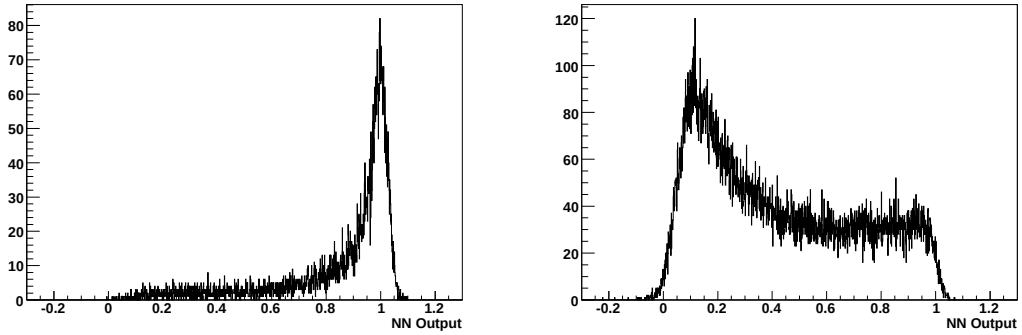

Figure 5.22: Distribution of the neural network output for signal (left) and hadronic $t\bar{t}$ (right).

Carlo studies presented in Section 3.3 since both those analyses used neural networks. The artificial neural network (ANN) package within TMVA, a tool for multi-variable analysis compatible with ROOT, was used in this analysis. The detailed description of ANN and the full documentation of TMVA can be found in [57].

5.5.1 Network training

In order to train the neural network a separate set of samples from those described in Section 5.1.1 was needed, each of them with an adequate number of events. Only the most relevant channels for the analysis, namely $t\bar{t}$, WWZ, ZZ, ZH and Wtb, were generated for an integrated luminosity of $125\,\mathrm{fb}^{-1}$ (1/4 of the amount produced in 5.1.1). These events were simulated and reconstructed in the same way as the other samples. For the signal 30000 events were simulated and reconstructed in order to have good statistics.

5.5.2 Variable optimisation

A first network was trained to test the variable optimisation described in Section 5.3.2. The nine variables described in Section 5.3.1 were used as inputs of a neural network. The output of the neural network for the signal and the hadronic $t\bar{t}$ background are shown in Figure 5.22; the signal peaks at 1 while the background close to 0, as expected.

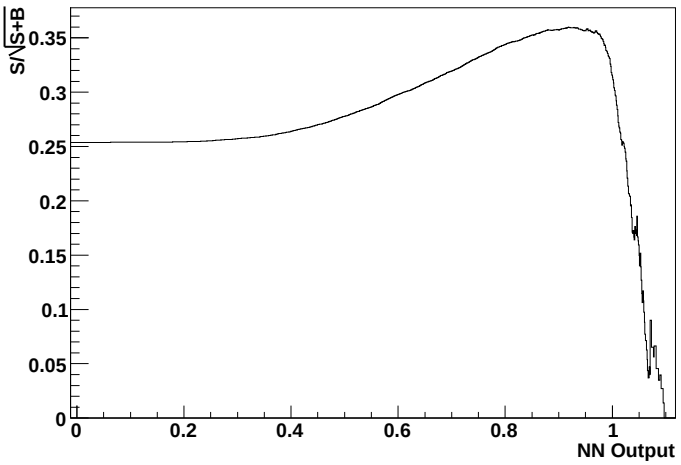

Figure 5.23: $S/\sqrt{S+B}$ as a function of the neural network output.

These plots were analysed in a similar way to the χ^2 variables of the previous section; the $S/\sqrt{S+B}$ is evaluated as a function of the neural network output as shown in Figure 5.23. At the maximum, $S/\sqrt{S+B} = 0.359 \pm 0.012$; this value is compatible with the the result of Section 5.3.2 which was 0.364 ± 0.011.

5.5.3 ZHH cross section sensitivity

Two neural networks were used to evaluate the sensitivity to the ZHH cross section. In order to have a valid training sample, the same cuts used for the event selection should be applied to the samples generated for the training. However these cuts reduced the training sample to 300 events for the backgrounds, not enough for training a neural network. Therefore the cut on the b tagging neural network output was released from 3.9 to 3.7.

The variables used in this analysis were:

- The sum of the b tagging neural network of the four jets with the highest b tag.
- $\chi^2_{ZHH} = \frac{(M_{ij}^{fit}-M_Z)^2}{\sigma_Z^2} + \frac{(M_{kl}^{fit}-M_H)^2}{\sigma_H^2} + \frac{(M_{mn}^{fit}-M_H)^2}{\sigma_H^2}$. For this selection, the two Higgs were reconstructed using the four most b-like jets; in order to further reduce the combinatorial the vertex charge information was used to pair jets with opposite charge. The combination that minimised the χ^2 was used.

Analysis	$S/\sqrt{S+B}$	S	B
Simple χ^2	0.36 ± 0.01	13.5	1364.5
χ^2 with b tag term	0.55 ± 0.06	4.0	47.0
χ^2 with b tag term and kin. fit.	0.56 ± 0.06	6.4	124.4
NN two variables	0.57 ± 0.06	5.8	99.2
NN three variables	0.54 ± 0.06	7.5	186.0

Table 5.6: Best $S/\sqrt{S+B}$ for different NN and cut based analyses.

Variable	Importance
NN b tag	75.14
χ^2_{ZHH}	6.172×10^{-06}
χ^2_{tt}	2.525×10^{-09}

Table 5.7: Importance of b tagging and χ^2 variables.

- $\chi^2_{tt} = \frac{(M_{ij}-M_W)^2}{\sigma_W^2} + \frac{(M_{kl}-M_W)^2}{\sigma_W^2} + \frac{(M_{mij}-M_{top})^2}{\sigma_t^2} + \frac{(M_{nkl}-M_{top})^2}{\sigma_t^2}$. The reconstruction of the two top quarks was performed in the following way: first the two most b-like jets were considered to be the product of the top decay and the other four jets were combined to form the W bosons. Then the W bosons were combined with the b jets to form the top. Among all possible combination the one that minimised the χ^2 was selected.

Two different networks were trained; one used the three variables while the other used the first two variables. The networks were applied only to those events that passed the nominal cuts. The $S/\sqrt{S+B}$ were obtained as before, looking for the maximum as a function of the neural network output; the results are summarised in Table 5.6. Within the statistical error, neither of the two networks improved the separation between signal and background.

This result can be better understood looking at the importance of the variables in the neural network shown in Table 5.7 . The importance I of the input variable i is give by $I_i = \bar{x_i}^2 \sum_j (w_{ij})^2$ where $\bar{x_i}$ is the mean of the variable in the training sample and w_{ij} are the weight linked with variable i. The b tagging information is by far more important than the χ^2 terms.

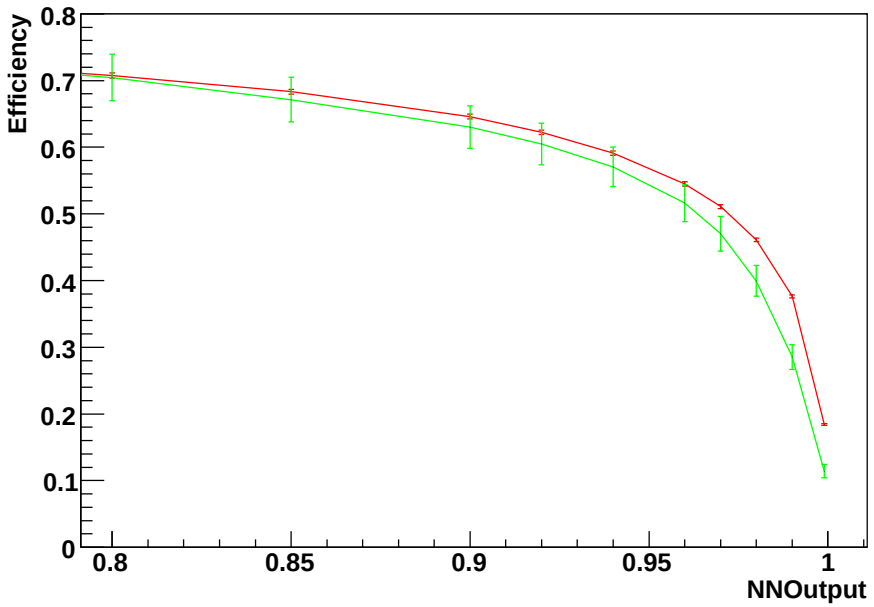

Figure 5.24: B tagging efficiency as a function of the NN b tag output for b jets ($t\bar{t}$ in red, Z in green).

5.6 b tagging performance

Having shown several times the importance of b tagging in this analysis, a study of the b tagging performance was carried out in order to understand how the vertex reconstruction was affected by the six-jet environment. In particular, a high rate of light and c-jets reconstructed as b jets would deeply affect this analysis.

In this study hadronic $t\bar{t}$ and $Z \rightarrow qq$ events were compared. In order to select b, c and light jets in $t\bar{t}$ events, the association between Monte Carlo quarks and jets described in Section 5.2 was used. The $t\bar{t}$ events were generated using Pandora Pythia at a centre of mass energy of 500 GeV. Three different samples were used for the Z, forcing the decay into b, c or light jets. These events were generated with Pandora Pythia at a centre of mass energy of 90 GeV.

For each type of jets, the b tagging efficiency was evaluated as a function of the b tagging neural network output. Results are shown in Figures 5.24, 5.25 and 5.26. All jets in the six-jet environment had a higher probability to be tagged as b jets; while this is good for real b jets, it is a problem for non-b jets. The c jets fake rate was increased by about 25% while for light jets the probability to be mis-tagged as b jets

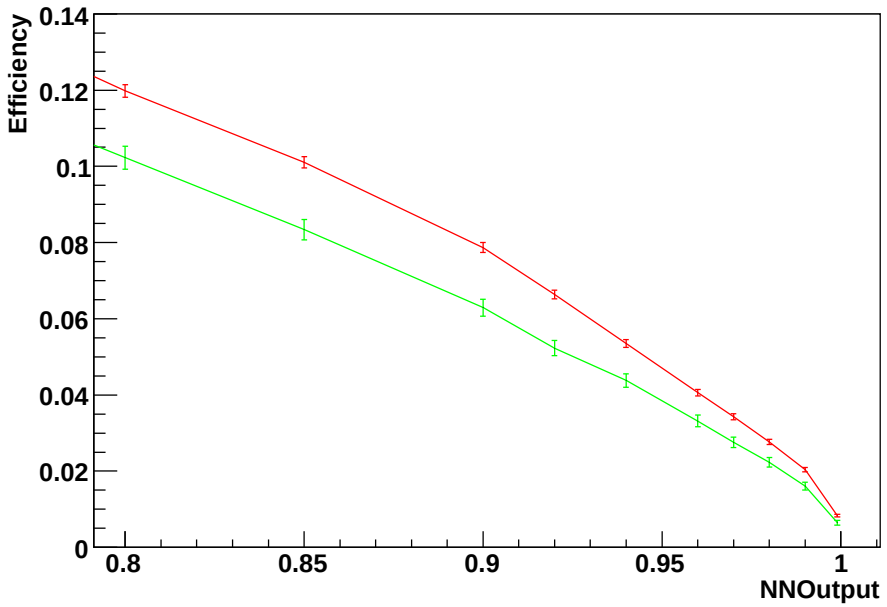

Figure 5.25: B tagging efficiency as a function of the NN b tag output for c jets ($t\bar{t}$ in red, Z in green).

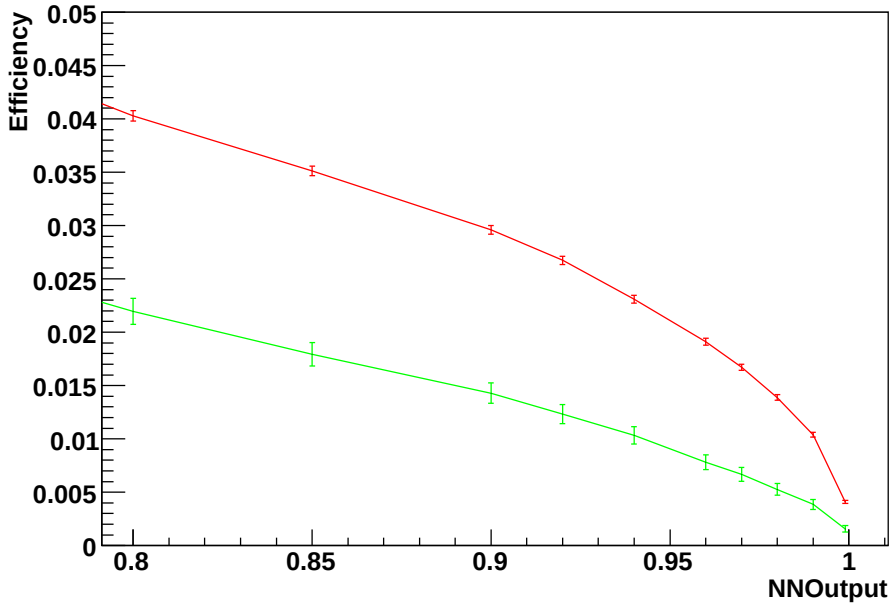

Figure 5.26: B tagging efficiency as a function of the NN b tag output for light jets ($t\bar{t}$ in red, Z in green).

was almost double for $t\bar{t}$ with respect to Z events.

If the same performance for the Z events could be achieved for the six-jet events, the hadronic $t\bar{t}$ background in the ZHH→qqbbbb analysis would be strongly suppressed: $t\bar{t} \rightarrow$ bbcscs would be reduced almost 6 times, $t\bar{t} \rightarrow$ bbcsud would be reduced about 9 times while $t\bar{t} \rightarrow$ bbudud would be reduced about 16 times where the difference in reduction is due to the difference in c-jet content between the channels. Since hadronic $t\bar{t}$ is the main background for the ZHH channel, it is clear that an improvement in b tagging performance would lead to a significantly better resolution of the Higgs self-coupling.

5.7 Conclusion

Different analyses using full event reconstruction have been performed to determine the resolution on the ZHH → qqbbbb cross section for a Linear Collider detector using $500\,\mathrm{fb}^{-1}$ of data. A sensitivity $S/\sqrt{S+B} = 0.56 \pm 0.06$ has been found using a cut based analysis and the result confirmed by a neural network analysis. The resolution on the ZHH cross section, defined as $\frac{\sqrt{S+B}}{S}$, was about 180%. All analyses show that b tagging plays a key role in this measurement. For example, if a similar performance could be achieved in the six-jet environment as in two-jet events, the resolution would improve by a factor two. Then, without performing any further optimisation, the resolution on the ZHH cross section would be about 95%.

The resolution on the ZHH cross section achieved in fast Monte Carlo simulations, described in Section 3.3, is about 20% [34] and 10% [31]. However several effects must be taken into account in order to compare this result with the one obtained in this thesis.

- The total integrated luminosity: the reduction of integrated luminosity from 2000 fb^{-1}, used in the fast simulation, to 500 fb^{-1}, used in this analysis, causes a factor two reduction in the resolution.

- Gluon emission: gluon emission was not included in the events generated for

the fast simulation analysis. From the studies in [34], it is possible to estimate that events with gluon emission, such as those used in this work, would have about a factor two worse resolution with respect to the events without.

- The decay modes of the Z considered in the analysis; $Z \rightarrow q\bar{q}$ has a BR of about 70% and that the neutrino and leptonic decay channels have a better background separation than the hadronic channel, so that about twice as many events could be used if these channels were included. This leads to a reduction in the resolution of about a factor 1.5 but applies only to the result in [31].

Considering these three effects, comparable resolutions on the ZHH cross section are about 80% for [34] and 60% for [31]. These values are not very distant from the resolution of 95% obtained in this analysis assuming a better vertex reconstruction. The remaining difference is likely to be due to detector effects, such as confusion in particle reconstruction. It is important to stress the fact that this is an indirect comparison; in order to have an accurate estimate of the differences between fast and full simulation, the same events should be compared using the same analysis.

Given the level of accuracy that is required in the coming LOI for a detector concept, the fast Monte Carlo studies should be treated with caution since the results cannot be replicated using full simulation. Moreover they do not include critical effects such as gluon emission and use an optimistic integrated luminosity. This work provides a better estimate for the detector performance, having included gluon emission, using a more realistic amount of data and performing a full simulation of the detector.

The sensitivity to the $ZHH \rightarrow qqbbbb$ cross section estimated in this thesis indicates that this process cannot be observed during the first phase of the Linear Collider which should achieve an integrated luminosity of $500\,\mathrm{fb}^{-1}$. Considering that the Higgs self-coupling is even more difficult to measure due to the ZHH irreducible background (those events produced without having a three-Higgs vertex), with this integrated luminosity the measurement of the Higgs self-coupling cannot be performed. In order to be sensitive to this parameter, an improvement of at least a factor three (for evidence) or five (for discovery) must be achieved in $S/\sqrt{S+B}$, assuming a better

vertex reconstruction than the one used in this analysis.

Increasing the integrated luminosity is the simplest way to improve the sensitivity. A further improvement could arise from better reconstruction, and in particular better jet reconstruction, which could lead to better vertex reconstruction (already assumed for the projected 95% resolution from this analysis). It is important to stress that in the simulation performed in this thesis, the luminosity calorimeters and the muon chambers were not used. Including them could improve the detector performance; the former may recover some of the energy lost in the beam pipe while the latter may identify muons in a jet, with this information then used to tag the jet as a b jets.

This analysis has highlighted the importance of b tagging performance and the needed for more studies of the vertex reconstruction in the multi-jet environment. Two of the key detector parameters for b tagging are the distance of the innermost layers of the vertex detector from the interaction point and the amount of material in the beam pipe and support structure, which causes multiple Coulomb scattering, limiting the vertex reconstruction. However these parameters also depend other phenomena; for example the position of the vertex layers is constrained by pair production in beam-beam interactions and by the magnetic field that reduces the looping of these pairs. The software reconstruction needs to be optimised for the six-jet environment, including training the neural network reconstruction with a six-jet sample instead of a two-jet sample. Studying and optimising all these parameters and algorithms will be the work of the LC community in the coming years; if we are successful, the Higgs self-coupling could be evaluated during the first phase of the Linear Collider, but this analysis shows that it will be a difficult task.

Appendix A

Event reconstruction

In this appendix the detailed description of the event reconstruction is described. The names used to identify the processors and the collections are, in general, the standard names defined by the authors of the packages.

Figure A.1 shows the flow diagram of the reconstruction from the hits in the tracking and calorimeter systems to the reconstruction of the particles. MyTPCDigiProcessor, MyVTXDigiProcessor and MyFTDDigiProcessor were the digitisation processors for the TPC, vertex and forwards tracker disks creating the collection of hits AllTPCTrackeHits, SITTrackerHits, VXTTrackerHits and FTDTrackerHits. The MyCurlKillerProcessor removes the hits in the AllTPCTrackeHits collection from the low momentum tracks that spiral in the TPC and may cause the TPC reconstruction to fail. The hits after this selection (TPCTrackeHits) were used by the MyTPCTrackingProcessor, together with the hits from the silicon tracker (SITTrackerHits) to form the TPCTracks. The silicon tracker hits, the forward disk hits and the vertex tracker hits were used by the MySiliconTracking processor to reconstruct the vertex tracks (SiTracks). The FullLDCTracking processor merged the TPC tracks and the vertex track in the final tracks in the LDCTracks collection. The collections denoted with the MCP suffix were the relation collections that linked the reconstructed tracks to the Monte Carlo tracks. MyMokkaCaloDigi processor performed the digitisation of the electromagnetic and hadronic calorimeters producing the ECAL and HCAL

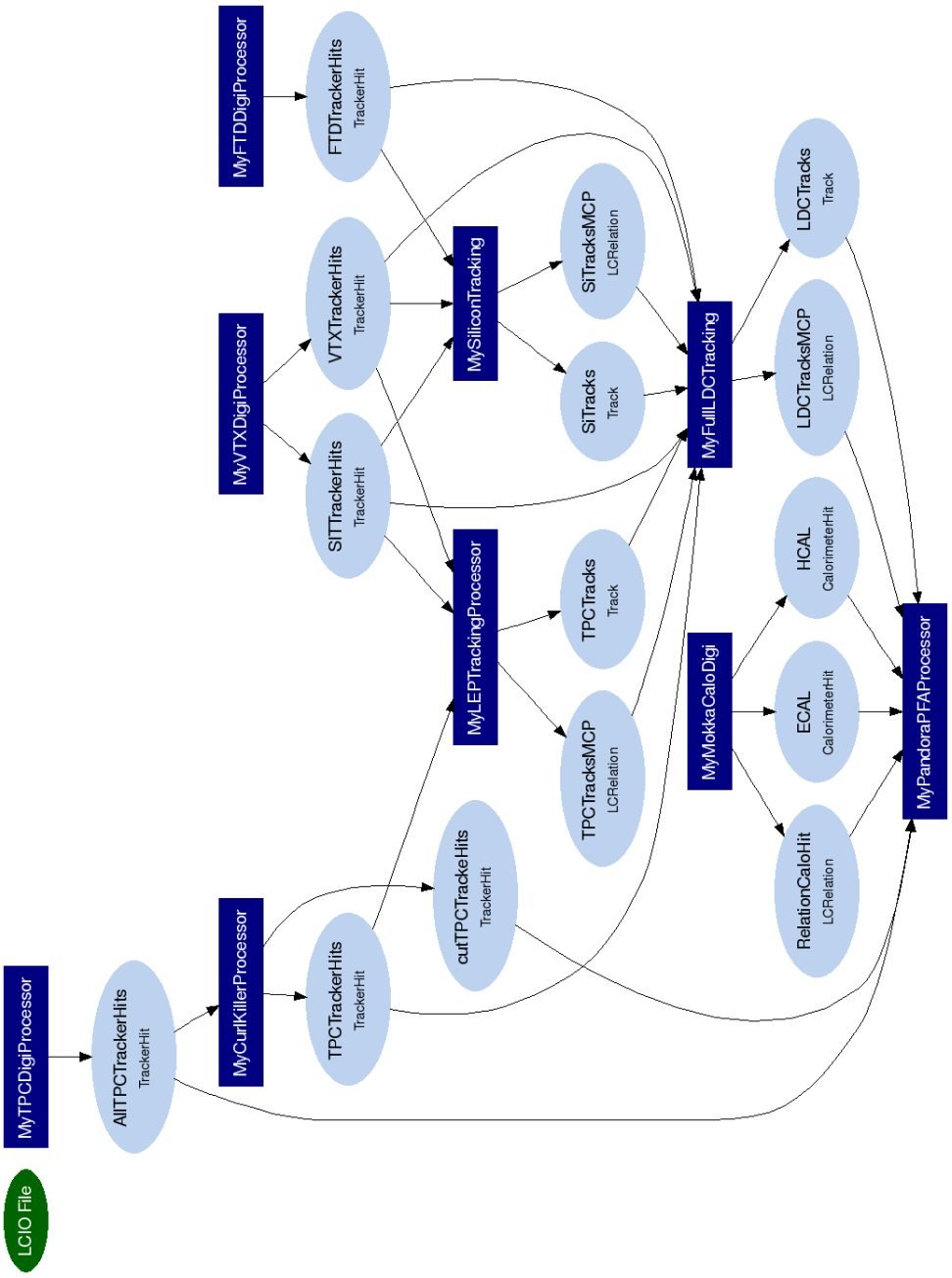

Figure A.1: Flow diagram of the event reconstruction from the hits to the reconstruction of particles by the PFA.

collections. All the available information was then given as input to the particle flow algorithm, in this case the MyPandoraPFAProcessor. The same information was also sent to another processor which performed the perfect PFA reconstruction as described in Section 4.3.

The diagram flow of the second part of the reconstruction, from the particle flow to the b tagging for a single PFA is shown in Figure A.2. The particle flow algorithm produced the collection of reconstructed particles (RecoParticles) which was then filtered by the MySelectReconstructedParticles to apply the 30 MeV filter discussed in Section 5.1.3. The resulting collection (SelectedRecoParticles) was given in input to the jet finding processor (MySatoru) which produced the Jet collection. The remaining processors are the default processors used in the vertex reconstruction which ends with the MyFlavourTag processor. The product of this processor is a collection (not shown in the figure) with the three tag information (b, c, and c with b background) for all the jets in the event.

A second identical and independent chain of processors was used to reconstruct the particles, the jets and the vertexes for the perfect PFA reconstruction, results of which are presented in Section 5.4.4.

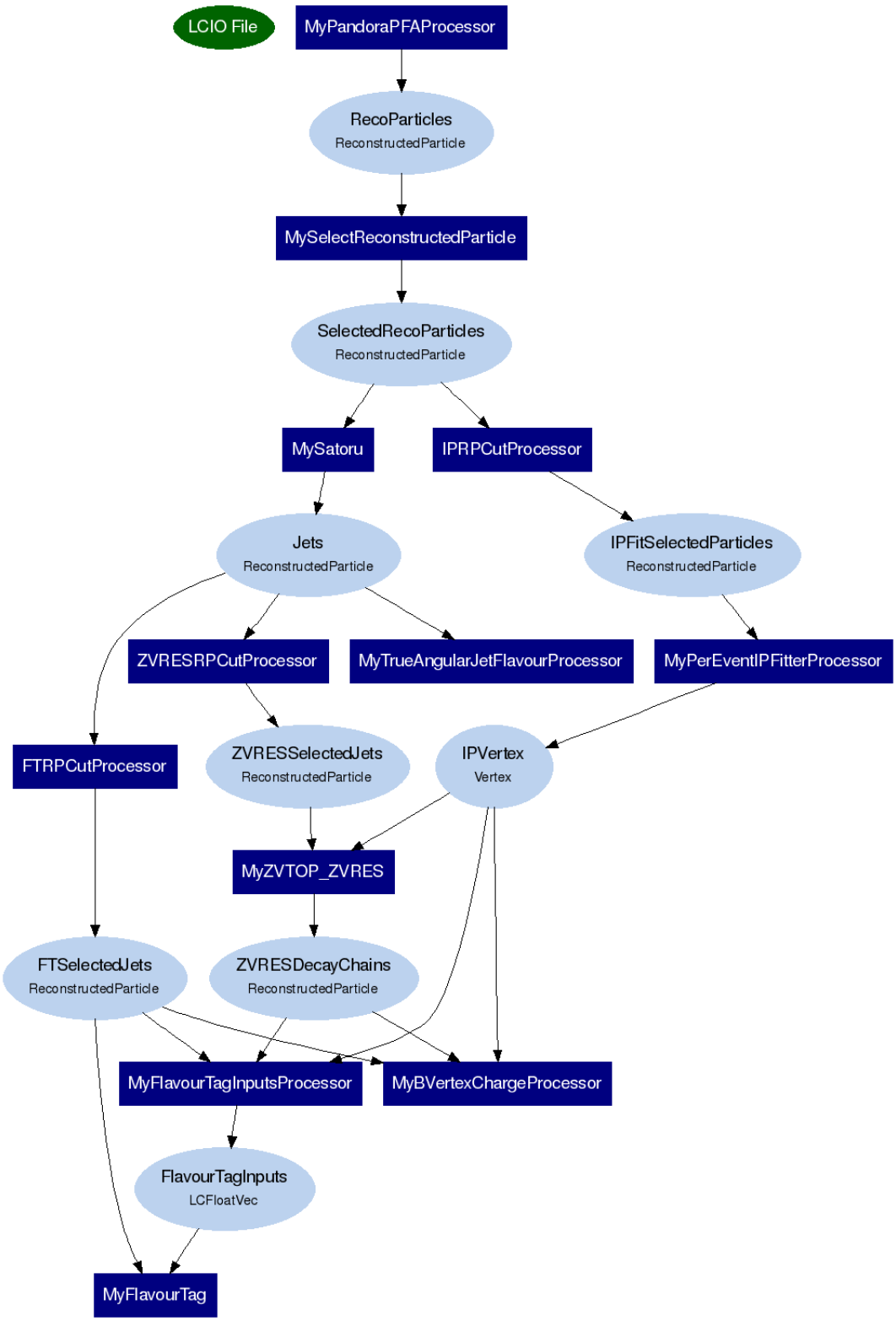

Figure A.2: Flow diagram of the event reconstruction from the reconstruction of particles from the PFA to the b tagging.

Bibliography

[1] G. Aarons et al. “International Linear Collider, Reference Design Report, Accelerator”, ILC-REPORT-2007-001 (2007).

[2] G. Aarons et al. “International Linear Collider, Reference Design Report, Detectors”, ILC-REPORT-2007-001 (2007).

[3] M. Battaglia et al., “Physics Benchmarks for the ILC Detectors”, arXiv:hep-ex/0603010v1.

[4] Calice Collaboration, https://twiki.cern.ch/twiki/bin/view/CALICE/WebHome.

[5] CALICE Collaboration, “Design and Electronics Commissioning of the Physics Prototype of a Si-W Electromagnetic Calorimeter for the International Linear Collider”, arXiv:0805.4833v1.

[6] Particle Data Group, chap 27, page 16.

[7] CALICE Collaboration,“Study of the response of the CALICE silicon-tungsten electromagnetic calorimeter prototype to electrons”, Calice Internal Noter, CAN-001.

[8] CALICE Collaboration, ”CALICE Report to the Calorimeter R&D Review Panel” ILC-DET-2007-024, Jul 2007, e-Print: arXiv:0707.1245.

[9] D. Chakraborty, "The Tail-Catcher/Muon Tracker for the CALICE Test Beam", in the Proceedings of 2005 International Linear Collider Workshop (LCWS 2005), Stanford, California, March 2005, http://www.slac.stanford.edu/econf/C050318/papers/0919.PDF.

[10] "Short indroduction to the use of the H6 area", http://ab-div-atb-ea.web.cern.ch/ab-div-atb-ea/BeamsAndAreas/h6/H6manual.pdf.

[11] http://polywww.in2p3.fr:8081/MOKKA.

[12] J. Spanggaard, "Delay wire chambers, a user guide", SL-Note-98-023 (BI).

[13] R. Wigmans, "Calorimetry", Clarendon Press, Oxford, 2000.

[14] ALEPH coll., " Performance of the ALEPH detector at LEP", NIM A360, p. 481-506.

[15] B. Aubert et al., NIM A330, 405 (1993).

[16] S. Glashow, Nucl. Phys. 22 (1961) 579; S. Weinberg, Phys. Rev. Lett. 19 (1967) 1264; A. Salam, in ?Elementary Particle Theory?, ed. N. Svartholm, Almqvist and Wiksells, Stockholm (1969) p. 367.

[17] M. Gell-Mann, Phys. Lett. 8 (1964) 214; G. Zweig, CERN-Report 8182/TH401 (1964); H. Fritzsch, M. Gell-Mann and H. Leutwyler, Phys. Lett. B47 (1973) 365; D. Gross and F. Wilczek, Phys. Rev. Lett. 30 (1973) 1343; H.D. Politzer, Phys. Rev. Lett. 30 (1973) 1346; G. ?t Hooft, Marseille Conference on Yang?Mills fields (1972).

[18] I. Aitchison and A. Hey, "Gauge Theories in Particle Physics", Adam Hilger, Bristol (UK), 1982.

[19] F. Halzen and A.D. Martin, "Quarks and Leptons: an introductory course in modern Particle Physics", Wiley, New York (USA), 1984.

[20] M.E. Peskin and D.V. Schroeder, "An introduction to Quantum Field Theory", Addison-Wesley, Reading (USA) 1995.

[21] A. Djouadi, "The Anatomy of Electro-Weak Symmetry Breaking", arXiv:hep-ph/0503172 v2 3 May 2005.

[22] P.W. Higgs, Phys. Rev. Lett. 13 (1964) 508; ibid. Phys. Rev. 145 (1966) 1156; F. Englert and R. Brout, Phys. Rev. Lett. 13 (1964) 321; G.S. Guralnik, C.R. Hagen and T. Kibble, Phys. Rev. Lett. 13 (1965) 585; T. Kibble, Phys. Rev. 155 (1967) 1554.

[23] The LEP Collaboration (ALEPH, DELPHI, L3 and OPAL), Phys. Lett. B565 (2003) 61.

[24] http://lepewwg.web.cern.ch/LEPEWWG/, winter 2008 update.

[25] W. Marciano and S. Willenbrock, Phys. Rev. D37 (1988) 2509; S. Dawson and S. Willenbrock, Phys. Rev. Lett. 62 (1989) 1232.

[26] G. Belanger et al., "Full order alpha electroweak corrections to double Higgs-strahlung at the linear collider", Phys. Lett. B576 (2003) 152-164.

[27] Zhang Ren-You, Ma Wen-Gan, Chen Hui, Sun Yan-Bin, Hou Hong-Sheng, "Full order alpha electroweak corrections to $e^+e^- \to ZHH$", hep-ph/0308203.

[28] W. Kilian, T. Ohl, J. Reuter, WHIZARD: Simulating Multi-Particle Processes at LHC and ILC , arXiv: 0708.4233 [hep-ph].

[29] M. Moretti, T. Ohl, J. Reuter, O'Mega: An Optimizing matrix element generator , LC-TOOL-2001-040-rev, arXiv: hep-ph/0102195-rev.

[30] W. Kilian, WHIZARD Manual 1.0, LC-TOOL-2001-039, http://www-flc.desy.de/lcnotes/.

[31] C. Castanier, P. Gay, P. Lutz, J. Orloff, "Higgs self-coupling measurement in e+ e- collisions at centre of mass energy of 500 GeV", hep-ex/0101028, 2001.

[32] G. Aarons et al. "International Linear Collider, Reference Design Report, Physics", ILC-REPORT-2007-001 (2007).

[33] http://hepwww.rl.ac.uk/LCFI/.

[34] T. Barklow, "Higgs self-coupling measurement", LCWS 2007, presentation.

[35] G. Weiglein et all., "Physics Interplay of the LHC and the ILC The LHC", arXiv:hep-ph/0410364v1.

[36] LCFI Group, "Neural Net Package", http://www-pnp.physics.ox.ac.uk/~hillert/VP/LCFIVertex-v00-01/NeuralNet.html.

[37] M. Faucci Giannelli, M. Green, F. Salvatore, "Comparison of Particle Flow Algorithms using e+e- -> ZHH Events at 500 GeV Centre of Mass", LC-PHSM-2007-003.

[38] F. Sefkow, "Performance goals and design cosiderations for a linear collider calorimeter", LC-DET-2004-022.

[39] J. Brient, "Improving the Jet Reconstruction with the Particle Flow Method; an Introduction", arXiv:physics/0412149v1.

[40] N. Akchurina et al., "Dual-Readout Calorimetry with Lead Tungstate Crystals", arXiv:0707.4019v1 [physics.ins-det] 26 Jul 2007.

[41] N. Akchurina et al., "Measurement of the Contribution of Neutrons to Hadron Calorimeter Signals", arXiv:0707.4021v1 [physics.ins-det] 26 Jul 2007.

[42] N. Akchurina et al., "Contributions of Cherenkov Light to th Signals from Lead Tungstane Crystals", arXiv:0707.4013v1 [physics.ins-det] 26 Jul 2007.

[43] ALEPH Collaboration, Nucl. Instrum. Meth. A360, 481 (1995).

[44] A. Raspiareza, "Modular Implementation of Particle Flow Algorithm with Minimized Dependence on the Detector Geometry", arXiv.org:physics/0601069.

[45] M. Thomson, "Particle Flow Calorimetry at ILC", arXiv:physics/0607261.

[46] O. Wendt, "Track based particle flow", arXiv:0710.2467.

[47] http://www-sldnt.slac.stanford.edu/nld/new/Docs/Generators/PANDORA.htm

[48] http://ilcsoft.desy.de/marlin/.

[49] See the tracking section on
http://ilcsoft.desy.de/MarlinReco/v00-02/manual_html/manual.html.

[50] http://polywww.in2p3.fr:8081/MOKKA/detector-models/ldc/ldc-models.

[51] Stirling W. J. et al., 1991, J. Phys. G: Nucl. Part. Phys. 17 1567.

[52] M. Faucci Giannelli, "Comparison between PFlow algorithms using ZHH channel", CALICE-UK meeting, Manchester, 2007, http://www.hep.ph.ic.ac.uk/calice/generalMeetings/061103manchester/fauccigiannelli.pdf.

[53] D. Jackson, NIM A 388 (1997) 247.

[54] L3 Collaboration, Phys. Lett. B 413, 176 (1997); OPAL Collaboration, Eur. Phys. J. C 1, 395 (1998); ALEPH Collaboration, Phys. Lett. B 422, 384 (1998).

[55] A. Abulencia et al. "Precision Top-Quark Mass Measurement in the Lepton+Jets Topology in $p\bar{p}$ Collisions at $\sqrt{s}$ =1.96 TeV", PRL 96, 022004 (2006).

[56] Y. Wembiao, "ZH $\rightarrow q\bar{q}b\bar{b}$ study with neural network", ILD workshop, Cambridge, 2008,
http://www.hep.ph.ic.ac.uk/calice/others/080911cambridge/yan1.pdf.

[57] TMVA, http://tmva.sourceforge.net.